2018

NEW APPROACHES TO CYCLOPENTADIENYL-FUSED THIOPHENE COMPLEXES OF IRON and SYNTHESIS AND CHARACTERIZATION OF CARBONIC ANHYDRASE ACTIVE-SITE MIMICS FOR CO_2 HYDRATION

Deepshikha Gupta
University of Kentucky, dgu222@g.uky.edu
Author ORCID Identifier:
https://orcid.org/0000-0002-3748-3021
Digital Object Identifier: https://doi.org/10.13023/ETD.2018.044

STUDENT AGREEMENT:

I represent that my thesis or dissertation and abstract are my original work. Proper attribution has been given to all outside sources. I understand that I am solely responsible for obtaining any needed copyright permissions. I have obtained needed written permission statement(s) from the owner(s) of each third-party copyrighted matter to be included in my work, allowing electronic distribution (if such use is not permitted by the fair use doctrine) which will be submitted to UKnowledge as Additional File.

I hereby grant to The University of Kentucky and its agents the irrevocable, non-exclusive, and royalty-free license to archive and make accessible my work in whole or in part in all forms of media, now or hereafter known. I agree that the document mentioned above may be made available immediately for worldwide access unless an embargo applies.

I retain all other ownership rights to the copyright of my work. I also retain the right to use in future works (such as articles or books) all or part of my work. I understand that I am free to register the copyright to my work.

REVIEW, APPROVAL AND ACCEPTANCE

The document mentioned above has been reviewed and accepted by the student's advisor, on behalf of the advisory committee, and by the Director of Graduate Studies (DGS), on behalf of the program; we verify that this is the final, approved version of the student's thesis including all changes required by the advisory committee. The undersigned agree to abide by the statements above.

Deepshikha Gupta, Student

Dr. John P. Selegue, Major Professor

Dr. Mark A. Lovell, Director of Graduate Studies

NEW APPROACHES TO CYCLOPENTADIENYL-FUSED THIOPHENE COMPLEXES OF IRON

and

SYNTHESIS AND CHARACTERIZATION OF CARBONIC ANHYDRASE ACTIVE-SITE MIMICS FOR CO_2 HYDRATION

DISSERTATION

A dissertation submitted in partial fulfillment of the requirements for the degree of Doctor of Philosophy in the College of Arts and Sciences at the University of Kentucky

By
Deepshikha Gupta
Lexington, Kentucky

Director: Dr. John P. Selegue, Professor of Chemistry
Lexington, Kentucky
2017

ABSTRACT OF DISSERTATION

NEW APPROACHES TO CYCLOPENTADIENYL-FUSED THIOPHENE COMPLEXES OF IRON

and

SYNTHESIS AND CHARACTERIZATION OF CARBONIC ANHYDRASE ACTIVE-SITE MIMICS FOR CO_2 HYDRATION

Polyheterocycles such as polythiophene and its derivatives comprise an important class of conducting polymers used for electronic applications. They have been of great interest for use in electronic materials due to their increased environmental stability as well as novel electronic properties in their polymer states. We have been interested in exploring the electronic properties of organometallic analogues of the low-band-gap polymer poly(benzo[3,4-*c*]thiophene) (polyisothianaphthene) that incorporates η^5-cyclopenta[*c*]thienyl monomers such as ferroceno[*c*]thiophene. First chapter of this dissertation involved synthetic attempts to ferroceno[*c*]thiophene. Exploring a shorter synthetic route to starting material, 1,2-di(hydroxymethyl)ferrocene was the first task. This was followed by attempts to synthesize an important precursor, 1,3-dihydroferroceno[*c*]thiophene to our target molecule, ferroceno[*c*]thiophene. In order to achieve our target precursor molecule, 1,3-dihydroferroceno[*c*]thiophene, we reacted 1,2-di(hydroxymethyl)ferrocene with H_2S/H_2SO_4 and Na_2S/HBF_4 respectively. Reaction of 1,2-di(hydroxymethyl)ferrocene with either H_2S/H_2SO_4 or Na_2S/HBF_4 results in 2,16-dithia[3.3](1,2)ferrocenophane instead of monomeric 1,3-dihydroferroceno[*c*]thiophene. Dehydration of 1,2-di(hydroxymethyl)ferrocene with dilute H_2SO_4 resulted in 2,16-dioxa[3.3](1,2)ferrocenophane. Formation of the five-membered tetrahydrothiophene or tetrahydrofuran rings is probably disfavored compared to formation of the ten-membered ferrocenophane rings because of greater strain in the five-membered rings. Thus, in order to achieve our target molecule ferroceno[*c*]thiophene, we took an alternate route. We decided to pursue the route with 1,4-dihydro-2,3-ferrocenodithiin being the precursor to our final target molecule. This was successfully accomplished. 1,2-Di(hydroxymethyl)ferrocene reacts with thiourea in the presence of catalytic trifluoroacetic acid to give a water-soluble thiouronium salt, which reacts with aqueous

potassium hydroxide in air to give 1,4-dihydro-2,3-ferrocenodithiin, via oxidation of the intermediate 1,2 di(mercaptomethyl)ferrocene. 1,4-dihydro-2,3-ferrocenodithiin, an important precursor to our desired heterocyclic chemistry was synthesized.

The increased emission of CO_2, a greenhouse gas, to the atmosphere is a matter of serious worldwide concern. Every year a few gigatons of CO_2 are added to the atmosphere by various anthropogenic activities like burning of fuel for electricity, running industry and transportation. Thus, developing ways to reduce the emission of CO_2 to the atmosphere is of major importance. Although the amine-based absorption method is considered the most reliable, it is an expensive alternative. The catalyzed enhancement of CO_2 absorption is a critical component to reduce the capital cost of CO_2 capture. Specifically, an effective catalyst will increase the CO_2 hydration rate, thereby decreasing the size of the absorber tower needed. In biological systems, CO_2 hydration is catalyzed by the enzyme carbonic anhydrase, which contains Zn^{II} in its active site. Carbonic anhydrase typically is not stable enough to be used in an industrial process, therefore, there is a need to synthesize robust, inexpensive CO_2 hydration catalysts.

Majority work of this dissertation focuses on designing catalysts that show high CO_2 hydration rate similar to carbonic anhydrase while showing superiority towards temperature, pH and inhibitors. We focused our efforts on complexes of Zn, Cu and Co with ligands such as 1,4,7,10-tetraazacyclododecane (cyclen), 5,5,7,12,12,14-hexamethyl-1,4,8,11-tetraazacyclotetradecane (teta and tetb), tris(benzimidazolylmethyl)amine (BIMA) and anionic tris(pyrazolylborate)s that mimic the enzyme, carbonic anhydrase. Several of these complexes have been reported for their interesting CO_2 capture properties but they contain hazardous perchlorate ion. We desired to replace them with benign, non-coordinating counterions like PF_6^-, BF_4^-, Cl^-, CH_3COO^-, NO_3^-, $CF_3SO_3^-$, SiF_6^{2-} that avoid the potentially explosive perchlorate salts. In order to test the activity of synthesized catalysts under industrial capture conditions, we designed a quick experimental screening pH drop method. $[[Zn(cyclen)(H_2O)][SiF_6]\bullet 2H_2O$ as well as a number of other catalysts have been synthesized and tested for their post-combustion CO_2 capture enhancement capabilities in aqueous solvent mixtures under both pH-drop screening and stopped-flow conditions.

$[Zn(cyclen)(H_2O)][SiF_6]\bullet 2H_2O$, which has an unreactive counteranion, is found to catalyze CO_2 hydration in aqueous solvent mixtures under both pH-drop screening and stopped-flow conditions. However, under pH-drop which has conditions similar to industrial post combustion capture, activity of $Zn(cyclen)(H_2O)][SiF_6]\bullet 2H_2O$ drops as compared to observed in stopped-flow conditions probably because of bicarbonate

coordination to Zn active site in these systems. The Zn center is highly electron deficient and therefore easily coordinates anions, inhibiting the ability to reform hydroxyl species on the metal. Thus, we decided to test the catalysis of benchmark enzyme carbonic anhydrase under similar conditions to determine the threshold k_{obs} value. Carbonic anhydrases catalyze the hydration of carbon dioxide at ambient temperatures and physiological pH with the highest known rate constant = 10^6 M^{-1} s^{-1}, but in our system (CAER pH drop screening) k_{obs} came out to be 438797 M^{-1} s^{-1}. The lower catalytic rate constant for carbonic anhydrase in 0.1000 M K_2CO_3, similar to Zn-cyclen, strengthens the conjecture that at high bicarbonate concentrations, HCO_3^- binding to the Zn(II) active site slows catalysis by inhibiting bicarbonate displacement with water to regenerate the active species.

The complexes containing anionic ligands that donate electron density into the metal center may serve to remove anionic bicarbonates/carbamates from the secondary coordination sphere and away from the metal center, thereby facilitating bicarbonate/anion dissociation and increasing CO_2 hydration rates. We studied catalysis of trispyrazolylborate molecule in 30% MEA and found the molecule to be catalytically active. We also developed an NMR-based method to see if the coordination of solvents to CO_2 capture solvents can be studied.

KEYWORDS: polythiophene, ferrocene, ferroceno[*c*]thiophene, carbon dioxide capture, carbonic anhydrase, cyclen

Deepshikha Gupta

11/28/17
Date

NEW APPROACHES TO CYCLOPENTADIENYL-FUSED THIOPHENE COMPLEXES OF IRON

and

SYNTHESIS AND CHARACTERIZATION OF CARBONIC ANHYDRASE ACTIVE-SITE MIMICS FOR CO_2 HYDRATION

By

Deepshikha Gupta

Dr. John P. Selegue

Director of Dissertation

Dr. Mark A. Lovell

Director of Graduate Studies

11/28/17

Date

Dedicated To
(My Mentors, Family and Friends)

Acknowledgments

"Now, this is not the end; it is not even the beginning of the end. But, it is perhaps, the end of the beginning"- Winston Churchill

My graduate career has been a journey of lifetime. I am deeply grateful to all the people – my mentor, advisory committee members, lab-mates, departmental staff, family and friends, who have helped me to achieve my scientific aspirations.

First and foremost, I want to wholeheartedly thank my advisor, Professor John P. Selegue, for his constant guidance, motivation, constructive criticism, dedication and commitment to scientific research. I can't thank him enough for his tremendous efforts, time and limitless patience in helping grow me as a research professional in my Ph.D. pursuit. His continued support and patience lead to where I stand today.

My advisory committee members have been very kind and encouraging in directing me towards my goal. I take this opportunity to thank, Dr. Folami Ladipo, Dr. Edith Glazer and Dr. Zach Hilt for their support and encouragement over the years. I am also very thankful to Dr. Stephen Rankin and Dr. David Atwood for serving in my committee for my final defense and for their wonderful suggestions. Also, I am very appreciative of support provided by DGS- Dr. Mark Lovell.

I would like to express my gratitude to Dr. Kunlei Liu from CAER for wonderful collaboration on Carbon Capture project. My special thanks to Dr. Joe Remias and Dr. Cameron Lippert for their assistance in experimental studies throughout my research and Anitha Wishrojwar for laying the foundations of this project.

I also extend my heartfelt thanks to Dr. Sean Parkin for his support with X-ray crystallography, Mr. John Layton for NMR facility and Dr. Jack Goodman for mass spectra services. Their support throughout my research really made things easier.

I am also very grateful for the funding that supported my research including teaching assistantship provided by University of Kentucky, Department of Chemistry and Research assistantship provided by CAER.

My sincere acknowledgment goes to all my former and current Selegue group members- Uttam, Mahendra, Rituraj, Anitha, Bidhya, Surya, Eric, Ilya and CAER group members- Moushumi, Payal, Krishna, Reynolds, Saloni, Huang and Taylor for being wonderful colleagues and creating a very positive workplace. I also extend special thanks to my friends from the department- Aman, Subbu, Minakshi and Rahul for being there through thick and thin of my dissertation.

I am particularly grateful to my supervisors at Piramal Pharma Solutions, Dr. Adrian Raiche and Dr. Walter Wu for their encouraging support to finish my doctorate studies.

Last but never the least, my greatest thanks go to my family and friends for their unconditional love. For my parents, Anil and Manju, who are my biggest support system. For my biggest fans Shalini and Shashank, my siblings, for always believing in me and my dreams. For my understanding in-laws for being very supportive. For my friends for the hearty laughter and endless heart-to-heart conversations. For the love of my life Aman and the apple of my eye, Shanaya, my daughter- I am indebted to them for all the sacrifices they have made to help me accomplish my long-awaited goal. Without their patience, none of this would have been possible. Thank you.

Table of Contents

List of Tables

List of Figures

List of Schemes

List of Abbreviations

General	
Å	Ångstrom 10^{-10} m
[°]	degrees
η^5	pentahapto
n-BuLi	n-butyllithium, $CH_3(CH_2)_3Li$
tBu	t-butyl, C_4H_9
Cp	cyclopentadienyl
°C	degree Celsius
dcalc	calculated density Mg/m^3
dec	decomposed
Fe	Ferrocene
h	hours
kJ	kilojoules
Me	methyl, CH_3
mg	milligrams
min	minutes
mL	milliliters
µL	microliters
mmol	millimoles
mp	melting point
Ph	phenyl
Tol	Tolyl, C_7H_7
MS	Mass spectra
m/z	Mass to charge ratio
M^+	Molecular ion
R	R-factor (for X-ray crystallography)
XRD	X-Ray Diffraction
GOF	goodness of fit
s	seconds
t	time
T	temperature
THF	tetrahydrofuran, C_4H_8O
CCS	Carbon Capture and Storage
PCC	Post Combustion Capture
CA	Carbonic Anhydrase
MEA	Monoethanol amine
WWC	Wetted-wall column
MDEA	Methyl diethanol amine
CAER	Center for Applied Energy Research
Cyclen	1,4,7,10-Tetraazacyclododecane
Teta	5,7,7,12,14,14-Hexamethyl-1,4,8,11-tetraazacyclotetradecane

BIMA	Tris-(2-benzimidazolylmethyl)amine
$CDCl_3$	Chloroform-d_1
DMSO-d_6	Dimethyl sulfoxide-d_6
D_2O	Deuterated Water
$Zn(BF_4)_2 \cdot 6H_2O$	Zinc tetrafluoroborate hexahydrate
$Co(BF_4)_2 \cdot 6H_2O$	Cobalt tetrafluoroborate hexahydrate
$Cu(BF_4)_2 \cdot 6H_2O$	Copper tetrafluoroborate hexahydrate
$Cu(CH_3COO)_2.2H_2O$	Copper acetate dihydrate
$Zn(CH_3COO)_2.2H_2O$	Zinc acetate dihydrate
$Zn(NO_3)_2.2H_2O$	Zinc nitrate dihydrate
$Zn(CF_3SO_3)_2.2H_2O$	Zinc triflate dihydrate
For nuclear magnetic resonance (NMR) spectra	
ppm	parts per million
δ	chemical shift (in parts per million)
s	singlet
d	doublet
t	triplet
q	quartet
p	pentet
m	multiplet
dd	doublet of doublets
dt	doublet of triplets
td	triplet of doublets
Hz	hertz s^{-1}
J	coupling constant
For infrared (IR) spectra	
FT IR	Fourier transform infrared
ATR	Attenuated total reflectance
cm^{-1}	wavenumbers
s	strong
w	weak
Br	broad or broadened

Chapter 1 Synthesis and Characterization of Ferrocene-Fused Thiophene Complexes

1.1 Introduction

1.1.1 Polyheterocycles

Polyheterocycles comprise an important class of semiconductors used for organic electronic applications (rechargeable batteries, electrolytic capacitors, LEDs, etc.), in particular polythiophene and polypyrrole derivatives. In terms of band theory, for conduction to occur in materials, a high-energy promotion from the valence band to the conduction band must occur. As the band gap essentially dictates the electronic behavior of the polymer, band gap control is critical to synthesizing materials of desirable properties. Research has continued to push towards polymers that have a low or zero band gap (metallic in nature). Goal of chemists is to synthesize polymers having small band gap and thus high conductivities. Polymers of this type would not require doping because they would be intrinsically conducting. These polymers would show high conductivity because having small gap would result in room temperature thermal excitation, thus allowing the promotion of electrons from the valence to the conduction

band. However, the mobility of the charge carriers in organic systems is a primary limiting factor. To achieve high conductivities, a small band gap and high mobilities are necessary. Due to the wide band gaps of most organic materials, they are not intrinsic semiconductors; thus, doping is required to reduce the band gap in order to conduct. When the material is doped, there is an introduction of lower energy transitions caused by the presence of solitons. When electrons are removed from the valence band, there is a partial delocalization of the newly formed charge over several chain lengths with an accompanying deformation in the local structure. This deformation causes higher energy levels or bands located within the band gap. Doping can be done electrochemically or chemically.[1] Oxidative doping is typically achieved with iodine, producing a p-doped polymer with an I_3^- counter ion. Reductive doping can be achieved using sodium metal to produce an n-doped polymer with a Na^+ counter ion.[2]

Practical concerns have limited use of polyacetylene and other linear polymers in materials processing. While these polymers display favorable electronic properties, they are brittle, insoluble and show poor environmental stability. Therefore, much of the interest research has switched to polyheterocycles, mainly polythiophene and

polypyrrole. Polythiophene and its derivatives have also been of great interest for use in electronic materials due to their increased environmental stability as well as novel electronic properties. Their stability is due to the ability of the heteroatom to stabilize the positive charge in the p-doped state.[3] In both doped and undoped states, polythiophene and its derivatives are stable to both air and moisture. Wudl *et al.* made a remarkable discovery by synthesizing poly(benzo[3,4-*c*]thiophene) (polyisothianaphthene, PITN), a polyheterocycle incorporating a thiophene with a fused, six-membered aromatic ring. Oxidatively doped PITN is an optically transparent, electrochromic polymer that exhibits increased conductivity and stability. The reason behind this is stabilization by additional resonance forms, quinoidal forms.[1,4] The discovery of PITN has promoted the expansion of an entire class of small intrinsic band-gap polymers incorporating a fused ring and a wide variety of structural variations.[5,6]

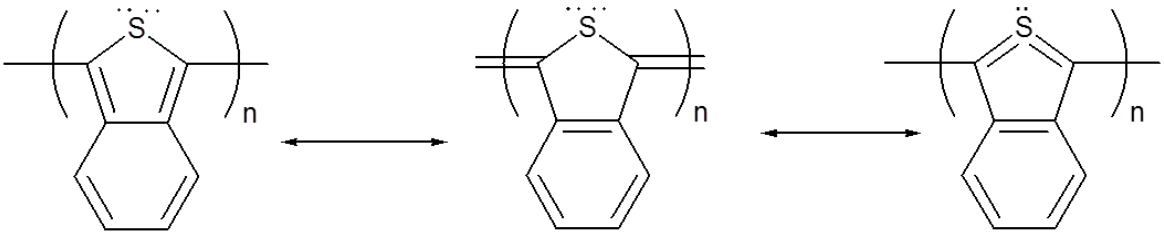

Figure 1.1 Polyisothianaphthene (PITN) resonance forms

Further progress in the area has been made, hoping that the use of fused rings would have the ability to tune the band gap of polyheterocycles, as well as providing the stability and processability required for electronic materials. However, there occurs an issue of insolubility of these polymers into common organic solvents. The insolubility of these polymers makes them difficult to purify and process. To increase solubility, thiophenes with solubilizing alkyl chains and other solubilizing functional groups can be introduced at the 3- and 4-positions of thiophene. Since 3-substituted thiophene is not a symmetrical molecule, coupling at the 2- and 5-positions leads to three possible regioisomeric linkages: head-to-head (HH), head-to-tail (HT), and tail-to-tail (TT). Regioregular functionalization also helps to create a highly ordered polymer by improving the solid-state order as a result of greater structural regularity.[6] A high degree of homogeneity or long-range order will lessen the effects of unfavorable steric interaction between R-substituents on adjacent heterocycles. Head-to-head ordering will cause planarity of the polymer to decrease, given in terms of the twist angle. This is significant because the electronic properties of conducting polymers are dependent upon efficient overlap of the π-orbital system of adjacent rings.

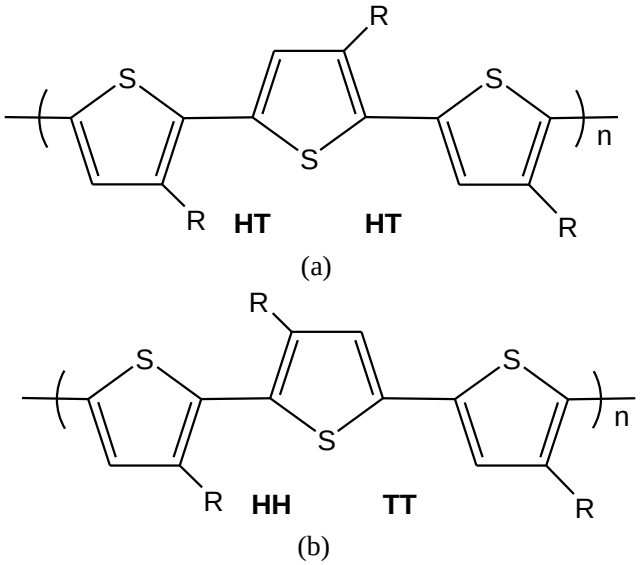

Figure 1.2 Ordering for 3-substituted polythiophene. (a) Polymer with regular head-to-tail linkages. b) Polymer with head-to-head and tail-to-tail linkages.

Thus, regioregular functionalization decreases the band gap of the polymer and enhances its conductivity as compared to regiorandom analogs. Poly(3-substituted thiophene)s are among the most studied polymeric materials for semiconductor applications. Recently, this made rr-P3HT, poly-3-hexylthiophene, one of the benchmark organic semiconductors, with charge-carrier mobility up to 0.1 cm^2/Vs. This benchmark polymer has several drawbacks, such as poor environmental stability.[7,8] High side-chain substitution frequency along the backbone lowers the interdigitation of the side-chain packing, thus lowering the three-dimensional order.

1.1.2 Metallocene-Fused Heterocycles

Incorporation of organometallic moieties into polymers has several advantages. These transition metal moieties could act as “switches”, enabling the polymer to be

reversibly doped and undoped by using the metal's electrochemistry.[9] It also allows for tuning the properties of the polymer by simply substituting different organic ligands on the metal center, thereby changing the electronic environment. These materials, which combine the electrical properties of the metals with the advantages of polymers such as lighter weight, greater workability, resistance to corrosion and chemical attack and lower cost, have become extremely attractive for many applications including light-emitting diodes (LEDs), chemical and biological sensors, microelectronic devices, and advanced textiles incorporating the advantages of strength, flexibility, and novel electronic properties.

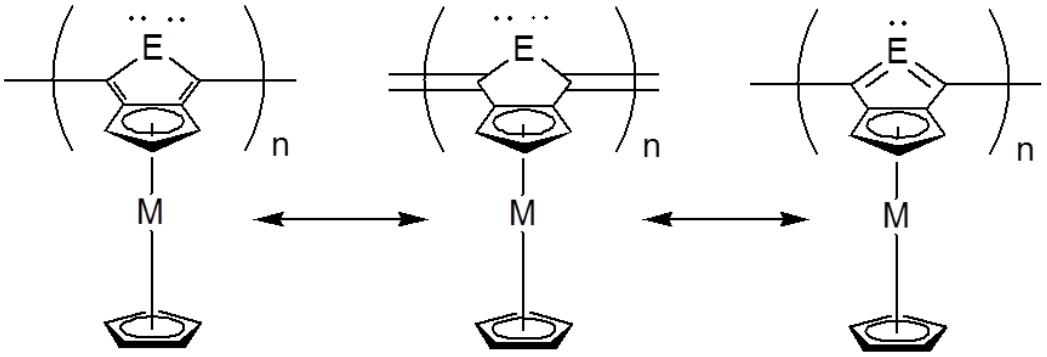

Figure 1.3. Resonance forms of the desired organometallic polymer system

Various transition metal polymer systems that incorporate the thiophene derivatives have already been explored. These systems can be classified based upon the

arrangement of the metal center relative to the polymer backbone. Type 1 organometallic polymers have the metal center situated on a tether or pendant attached to the polymer backbone. In this case, there is little electronic interaction between the metal center and the backbone and the polymer serves as a support with little effect on the properties of the metal. Type II metal-containing polymers have the metal and the polymer electronically coupled, thus leading to the ability of the metal to influence the properties of the polymer. The metal center itself is not incorporated into the polymer backbone. In contrast, Type III polymers have the metal situated within the backbone, leading to a strong interaction between metal and organic chain.[10]

1.1.3 Goal of this project

Intrigued by these properties, our group's long-term interest is in the electronic properties of organometallic analogues of the low-band-gap polymer PITN that incorporate cyclopenta[*c*]thienyl monomers or polycyclic aromatic hydrocarbons as ligands.[11] Organometallic groups provide the ability to tune the band gap, thus increasing the conductivities as well as providing the stability and processability required for the electronic materials.[9] Selegue and coworkers have been particularly interested in fused-ring thiophenes and pyrroles incorporating group 6–9 metals bound in a π fashion through the ring portion. While a variety of hapticities is possible through both the thiophene and ring portion, the Selegue group has focused primarily upon coordination

through a fused Cp ring. We are primarily interested in fused-ring thiophenes as synthetic models and precursors for potential Type II organometallic polymers incorporating a polyheterocyclic backbone. Selegue and Swarat prepared a chromium complex of benzo[3,4-*c*]thiophene, from the reaction of benzo[3,4-*c*]thiophene with photochemically generated [Cr(thf)$(CO)_5$] at room temperature.[12] It was the first transition metal complex of benzo[3,4-*c*]thiophene. X-ray diffraction showed that chromium is bound to the benzo ring rather than the thiophene ring. The stability of the complex was found to be better than that of a free non-classical thiophene. Wallace *et al.* prepared pyridazine complexes of ruthenium, by employing two different methodologies. The first method involves the reaction of [Ru{η^5-$C_5H_3(CO_2Ph)_2$}(Cp^*)] with hydrazine monohydrate; the second method involves the deprotonation of free cyclopenta[*d*]pyridazines[13] with thallium ethoxide followed by treatment with [Ru(μ_3-Cl)(Cp^*)]$_4$ to give pyridazine complexes.[14] Similarly, 1,4-difurylcyclopenta[*c*]pyridazyl complexes of manganese and rhenium have been studied.[15] Blankenbuehler, Snyder and Selegue reported on the formation of discrete manganese tricarbonyl complexes incorporating cyclopenta[*c*]thiophenes.[11] Tice expanded the work to prepare a number of cyclopenta[*c*]thienyl complexes of manganese including 4-chloro and 4-bromothiapentanyl complexes and succeeded in coupling the 4-bromo complex with phenylboronic acid under Suzuki conditions.[16] Current project at Selegue lab is aimed at developing monomers based on ferrocene-fused thiophene

systems. Efforts are underway to prepare Type II metallopolymers chemically and/or electrochemically. Appreciable progress has been made over the years for low-band gap materials with modest environmental stability compared to polyacetylene. However, an ideally stable, easily processable, zero-band gap conducting polymer is yet to be reported. In order to synthesize organometallic polyheterocycles and predict the properties and characteristics of the polymer, it is important to understand how the heterocycle bonds to the metal center. Herein, we report on the continued investigation to improve the understanding of the interaction of fused-ring thiophenes and their potential incorporation into conducting polymers.

1.2 Experimental

Reactions are carried out using standard Schlenk line techniques under nitrogen. Solvents were dried and distilled under nitrogen before use, including ethyl ether, benzene, tetrahydrofuran (THF), hexane and toluene over sodium benzophenone ketyl. Dichloromethane and acetonitrile were dried and distilled over calcium hydride. $CDCl_3$, C_6D_6, DMSO-d_6 and acetone-d_6 (Cambridge Isotopes), N,N,N',N-tetramethylmethylenediamine (Aldrich), *n*-butyllithium 2.5 M (Aldrich), active manganese dioxide (Acros), sodium hydroxide (Fisher), potassium hydroxide (EMD), were used without further purification. H_2S was obtained from the Matheson Co. Inc. 1,2-Di(hydroxymethyl)ferrocene was prepared by literature methods.[17,18,19] Organic phases

were dried using either anhydrous sodium sulfate or anhydrous magnesium sulfate purchased from Mallinckrodt. Flash chromatography was performed using 60-Å pore size, 230–400 mesh silica gel purchased from Sorbent Technologies. ^{1}H and ^{13}C NMR spectra were recorded on a Varian Gemini-400 spectrometer at ca. 22 °C unless mentioned otherwise and were referenced to residual solvent peaks. Infrared spectra were recorded on an ATI-Mattson Galaxy Series 5000 FTIR15 spectrometer. Mass spectra were acquired by the University of Kentucky Mass Spectrometry Facility. Electron ionization (EI) mass spectra were recorded at 70 eV on a Thermo Finnigan PolarisQ (quadrupole ion trap). Samples were introduced via a heatable direct insertion probe. Melting points were taken on Thomas Hoover capillary melting point apparatus and were uncorrected. X-ray diffraction data were collected at 90 K on either a Nonius KappaCCD diffractometer or a Bruker-Nonius X8 Proteum diffractometer. Crystal indexing and data processing were performed with either DENZO-SMN (KappaCCD)[20] or with Bruker APEX2 (X8 Proteum). The structures were solved and refined by using SHELXL-97.[21]

1.2.1 Synthesis

1.2.1.1 Preparation of 1,4-dihydro-2,3-ferrocenodithiin

To a 250-mL, three-necked flask containing refluxing dichloromethane (50 mL) and trifluoroacetic acid (5 drops) at reflux were added 1,2-di(hydroxymethyl)ferrocene (150.0 mg, 0.609 mmol) in freshly distilled dichloromethane (7.7 mL) from a dropping funnel

and thiourea (150.0 mg, 1.970 mmol) from a solid-addition sidearm, simultaneously over about 1 h with vigorous stirring. The reaction mixture was refluxed in a dinitrogen atmosphere for 18 hours. After cooling to room temperature, the reaction mixture was washed with 5% KOH solution. The organic layer was separated, washed several times with water, dried over anhydrous magnesium sulfate and evaporated under reduced pressure. The product was column chromatographed over silica gel with hexane-ether (3:1) to get the crude product. The compound was crystallized from ether/ hexane as bright yellow-orange crystals. Yield was around 20%. **^{1}H NMR, 400 MHz ($CDCl_3$)**: δ (ppm) 4.13 (d, 2H, ^{2}J = 2.4 Hz, C***H***CHC***H***), 4.122 (s, 5H, Cp), 3.989 (t, 1H, ^{3}J = 2.4 Hz, CHC***H***CH), 3.89(d, CH_2, Ha ^{2}J = 14.8 Hz), 3.59 (d, CH_2, H_b^{2}J = 15.2 Hz). **MS m/e:** 276, 212, 152, 121, 91, 77, 65, 56. **^{13}C NMR (50 MHz, $CDCl_3$, ppm):** δ (ppm) 32.587 (CH_2), 81.200 (*ipso* Cp), 70.527 (unsubstituted Cp), 67.422(C***H***CHC***H***), 64.037 (CHC***H***CH). IR (ATR, cm^{-1}) 3093, 2922, 1396, 1103, 903, 650; Mp. 98 ˚C. Complete characterization was done by X-ray crystallography.

1.2.1.2 Preparation of 2,16-dioxa[3.3](1,2)ferrocenophane

1.2.1.2.1 Method 1

To 1,2-di(hydroxymethyl)ferrocene (50.0 mg, 0.21 mmol) dissolved in freshly distilled ethyl ether was added 10 drops of 3:1 water: H_2SO_4. The reaction mixture became lighter in color and a precipitate appeared. The mixture was left stirring overnight and filtered.

The precipitate was washed with ether and vacuum dried. Yield was 70% **m.p.** 210 ºC (dec. without melting) **^{1}H NMR, 400 MHz ($CDCl_3$):** δ (ppm) 4.411 (d, 4H, ^{2}J = 2.8 Hz, C***H***CHC***H***), 3.978 (s, 10H, Cp), 4.293 (t, 2H, ^{2}J = 2.8 Hz, CHC***H***CH), 4.34 (d, CH_2, Ha ^{2}J = 13.2 Hz), 4.007 (d, CH_2, H_b^{2}J = 12.8 Hz). **MS, m/e:**456(M^+), 390, 362, 227, 200,186, 128, 91, 73, 56. **^{13}C{^{1}H} NMR (50 MHz, $CDCl_3$, ppm):** δ (ppm) 60.774 (CH_2), 82.930 (*ipso* Cp), 69.359 (unsubstituted Cp), 70.192 (C***H***CHC***H***), 69.954 (CHC***H***CH). Complete characterization was done by X-ray crystallography.

1.2.1.2.2 Method 2

Tosyl chloride (38.73 mg, 0.203 mmol) was added to 1,2-di(hydroxymethyl)ferrocene (50.0 mg, 0.20 mmol), in 15 mL of refluxing benzene. After two hours, the reaction mixture was cooled, the precipitate was collected, washed with ether and vacuum dried. Yield was 60%.

1.2.1.3 Preparation of 2,16-dithia[3.3](1,2)ferrocenophane

1.2.1.3.1 Method 1

Dilute H_2SO_4 (30 drops, 1:1) was added to 1,2-di(hydroxymethyl)ferrocene (100.0 mg, 0.406 mmol) in freshly distilled ethyl ether (60 mL). As H_2S from an H_2S cylinder was bubbled through the solution for 2 h, a precipitate appeared. The precipitate was filtered, washed with ether and vacuum dried. Yield was 80% **m.p.** 172 °C (dec. without melting). **^{1}H NMR, 400 MHz ($CDCl_3$):** δ (ppm) 4.391(d, 4H, ^{3}J = 2.4 Hz, C***H***CHC***H***), 3.950 (s,

10H, Cp), 4.155 (t, 2H, ^2J = 2.8 Hz, CHC***H***CH), 3.348(d, CH_2, $H_a$$^2J$ = 15.2 Hz), 3.09 (d, CH_2, $H_b$$^2J$ = 15.2 Hz).**MS, m/e:** 488(M^+), 308, 307, 306, 304, 244, 241, 212, 186, 121, 91, 65, 56. Complete characterization was done by X-ray crystallography.

1.2.1.3.2 Method 2

To 1,2-di(hydroxymethyl)ferrocene (100.0 mg, 0.406 mmol) dissolved in freshly distilled dichloromethane was added $Na_2S{\cdot}9H_2O$ (97.44 mg, 0.406 mmol). A few drops of HBF_4 (48% aqueous) were added with vigorous stirring. The reaction mixture was stirred for 30 minutes at room temperature and 30 mL of ether was added. The ethereal solution was washed twice with water and dried with magnesium sulfate. The compound was vacuum dried. Yield was 70%.

1.3 Results and Discussion

The organometallic chemistry of thiophene-based compounds has been extensively studied during the past few years. It is motivated by the search for metal-based catalysts to accomplish the hydrodesulfurization of fossil fuels. The hydrodesulfurization of fossil fuels is very important as a means for providing a cleaner form of energy. In fossil fuels, organic sulfur is present in the form of thiophenes, benzothiophenes, etc. As a result, the research is driven to investigate sulfur-bound chemistry of thiophene-metal complexes.[22] Thiophene can bind to a metal center in a

variety of ways. The lone pairs on sulfur can bond to the metal in a sigma fashion. HDS catalysts have been developed to remove the sulfur from these compounds. The mechanism of how these catalysts work is still unclear. Much work has been done to investigate S-bound thiophene-metal complexes because it was believed that thiophene compounds would adsorb onto the metal catalysts by means of a sulfur-metal bond. This would activate the sulfur-carbon bonds to aid in loss of the sulfur atom. In order to synthesize organometallic polyheterocycles and predict the properties and characteristics of the polymer, it is important to understand how the heterocycle bonds to the metal center.

1.3.1 Synthesis

1,2-Di(hydroxymethyl)ferrocene is a very important precursor for our desired heterocyclic chemistry. Synthesis of 1,2-di(hydroxymethyl)ferrocene was performed by the method of Marr and Rockett[17,18,19] (Scheme 1.1). It is a time-consuming method with an overall low yield due to lithiation step.

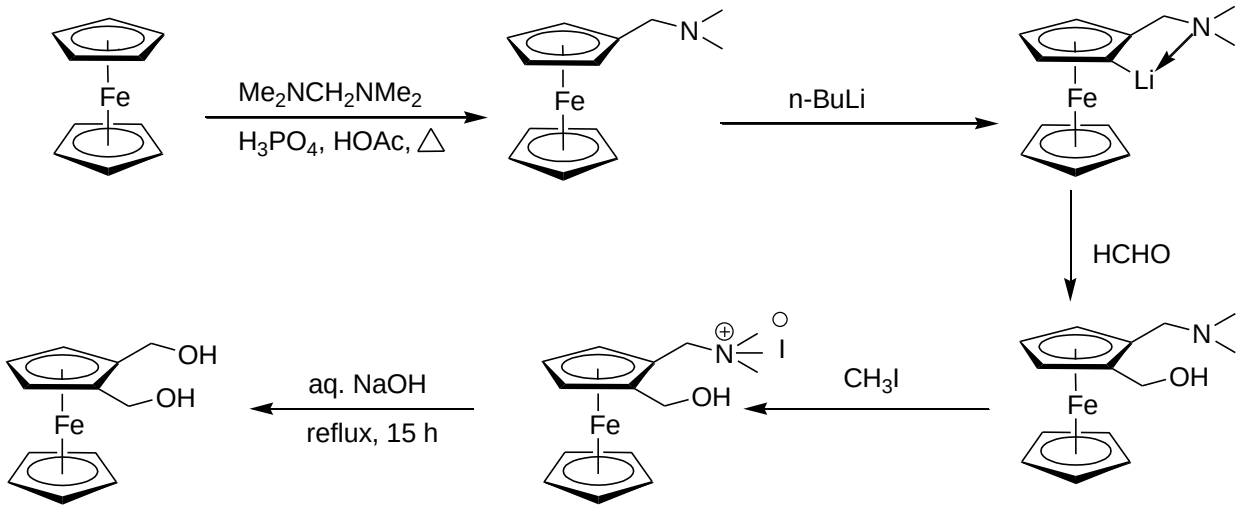

Scheme 1.1 Preparation of 1,2-di(hydroxymethyl)ferrocene[17, 18,19]

We sought a more convenient, higher-yield method to prepare the diol.[23,24,25,26,27] (Scheme 1.2). The route shown below avoids the troublesome lithiation step. Intermediates 1-(3-carboxypropionyl)ferrocene, 1-(3-carboxypropyl)ferrocene and α–keto-1,2-tetramethyleneferrocene were prepared according to literature procedures by Rinehart *et al.*[23-24] Although oxidation of α–keto-1,2-tetramethyleneferrocene to 1,2-ferrocenedicarboxylic acid has been reported in the literature by Maier *et al.*,[27] we were unable to reproduce the results.

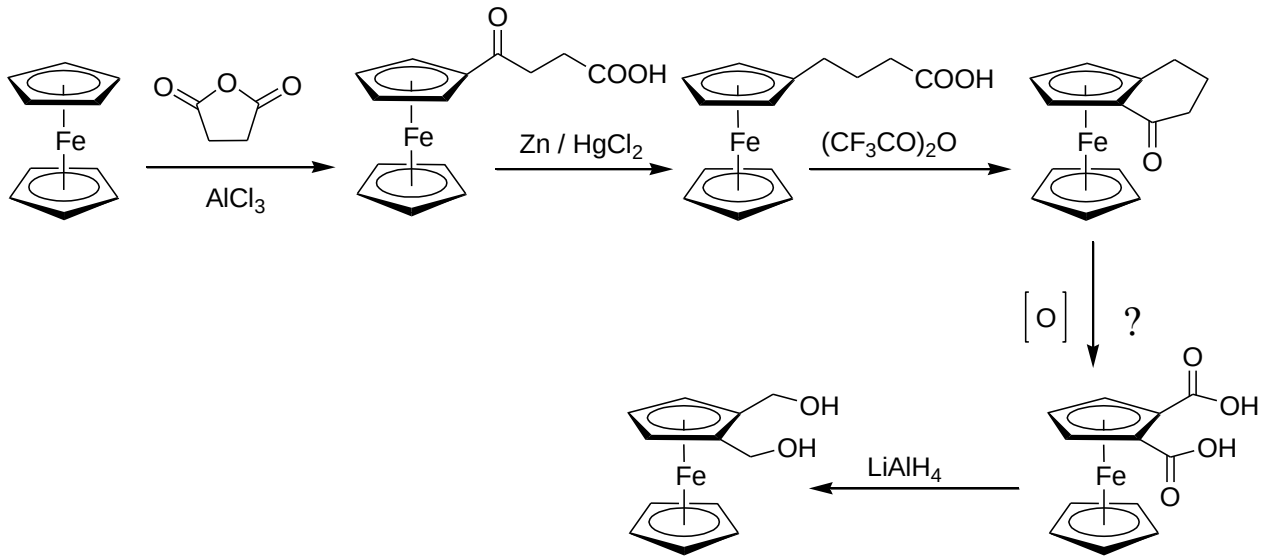

Scheme 1.2 Attempted alternative preparation of ferrocene 1,2-dicarboxylic acid[23,24,25,26,27]

Oxidation of acetylferrocene to ferrocenecarboxylic acid is well known.[25,26,27] Following the procedures for oxidation of acetylferrocene to ferrocenecarboxylic acid, several attempts to oxidize ferrocene cyclic ketone to ferrocenedicarboxylic acid such as reaction with NaOCl, Br_2/NaOH, I_2/NaOH, potassium superoxide in the presence of crown ether were made. All of the above reactions lead to either no reaction or the decomposed product. Repeated attempts to synthesize the acid have failed so far.

1.3.1.1 Preparation of 2,16-dithia[3.3](1,2)ferrocenophane

1,3-dihydroferroceno[*c*]thiophene is a very important intermediate for our desired heterocyclic chemistry (Scheme 1.3)

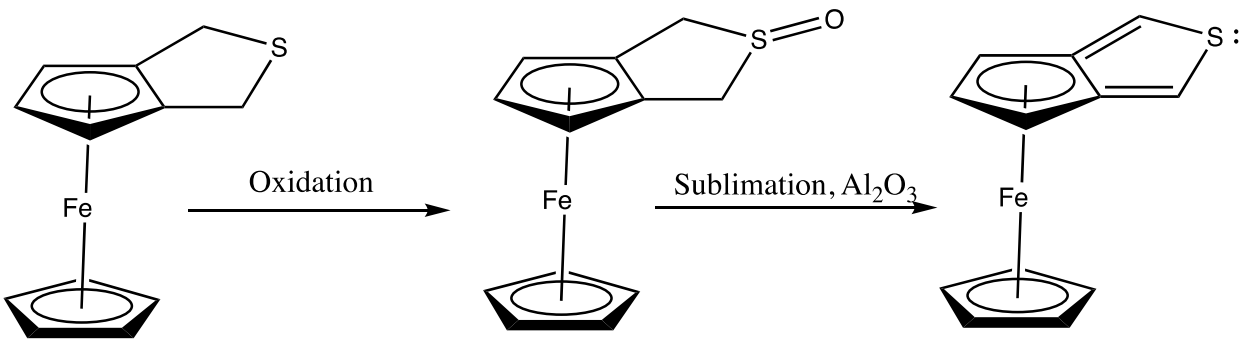

Scheme 1.3 Preparation of ferroceno[*c*]thiophene

In order to prepare starting material 1,3-dihydroferroceno[*c*]thiophene, we followed the strategy of Ratajczak *et al.*,[28] but we were not able to obtain the monomeric 1,3-dihydroferroceno[*c*]thiophene. We tried another approach by Boev *et al.*[29] in order to prepare the monomer. Reaction of 1,2-di(hydroxymethyl)ferrocene with either H_2S/H_2SO_4 or Na_2S/HBF_4 results in 2,16-dithia[3.3](1,2)ferrocenophane instead of monomeric 1,3-dihydroferroceno[*c*]thiophene (Scheme 1.4). The dimer is thought to be more stable than the monomer because of strain in the five-membered dihydrothiophene ring.

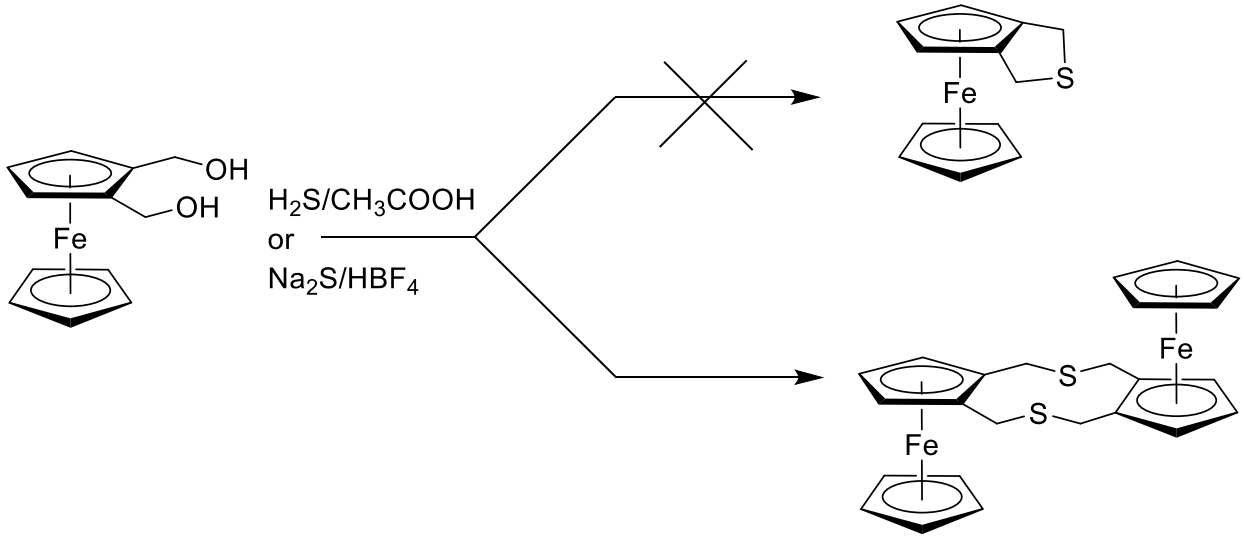

Scheme 1.4 Preparation of 2,16-dithia[3.3](1,2)ferrocenophane

1.3.1.2 Preparation of 2,16-dioxa[3.3](1,2)ferrocenophane

In order to determine whether monomer is possible in furan system, we attempted to dehydrate 1,2-di(hydroxymethyl)ferrocene with dilute H_2SO_4, but the reaction resulted in 2,16-dioxa[3.3](1,2)ferrocenophane instead of monomeric 1,3-dihydroferroceno[*c*]furan. We tried another approach to monomeric 1,3-dihydroferroceno[*c*]furan. As synthesized by Hillman *et al.* on 1,2' derivative[30], we hoped to get intramolecular reaction, but reaction of 1,2-di(hydroxymethyl)ferrocene with tosyl chloride also results in the formation of 2,16-dioxa[3.3](1,2)ferrocenophane (Scheme 1.5).

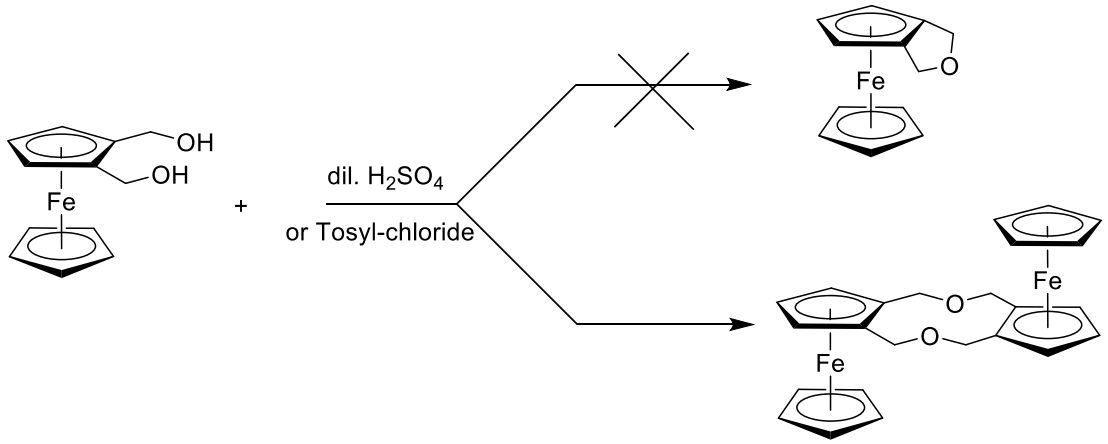

Scheme 1.5 Preparation of 2,16-dioxa[3.3](1,2)ferrocenophane

Formation of the five-membered tetrahydrothiophene or tetrahydrofuran rings is probably disfavored compared to formation of the ten-membered ferrocenophane rings because of greater strain in the five-membered rings.

1.3.1.3 Preparation of 1,4-dihydro-2,3-ferrocenodithiin

Thus, in order to achieve our target ferrocene-fused thiophene polymer, we thought of taking an alternate route. We decided to pursue route with 1,4-dihydro-2,3-ferrocenodithiin being the precursor to our final target molecule (Scheme 1.6).

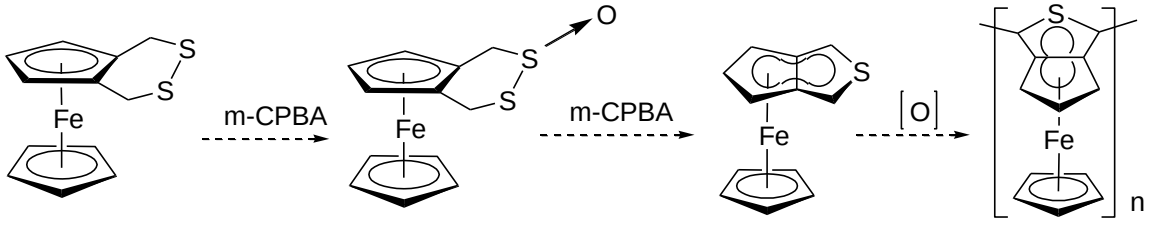

Scheme 1.6 Preparation of ferroceno[*c*]thiophene polymer

1,4-dihydro-2,3-ferrocenodithiin is a very important intermediate for our desired heterocyclic chemistry. We picked this idea from the similar type of chemistry done on benzo analogues by Sato and coworkers.[26] (Scheme 1.7)

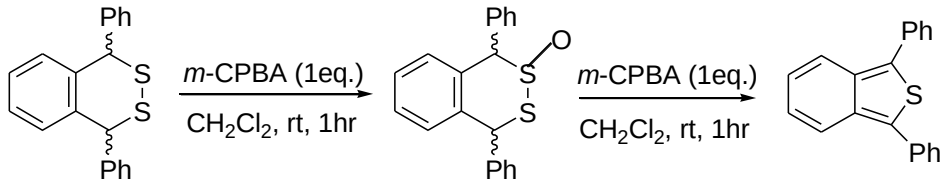

Scheme 1.7 Preparation of 1,3-diphenylbenzo[*c*]thiophene

1,2-Di(hydroxymethyl)ferrocene reacts with thiourea in the presence of catalytic trifluoroacetic acid to give a water-soluble thiouronium salt, which reacts with aqueous potassium hydroxide in air to give 1,4-dihydro-2,3-ferrocenodithiin, via oxidation of the intermediate 1,2 di(mercaptomethyl)ferrocene. (Scheme 1.8)

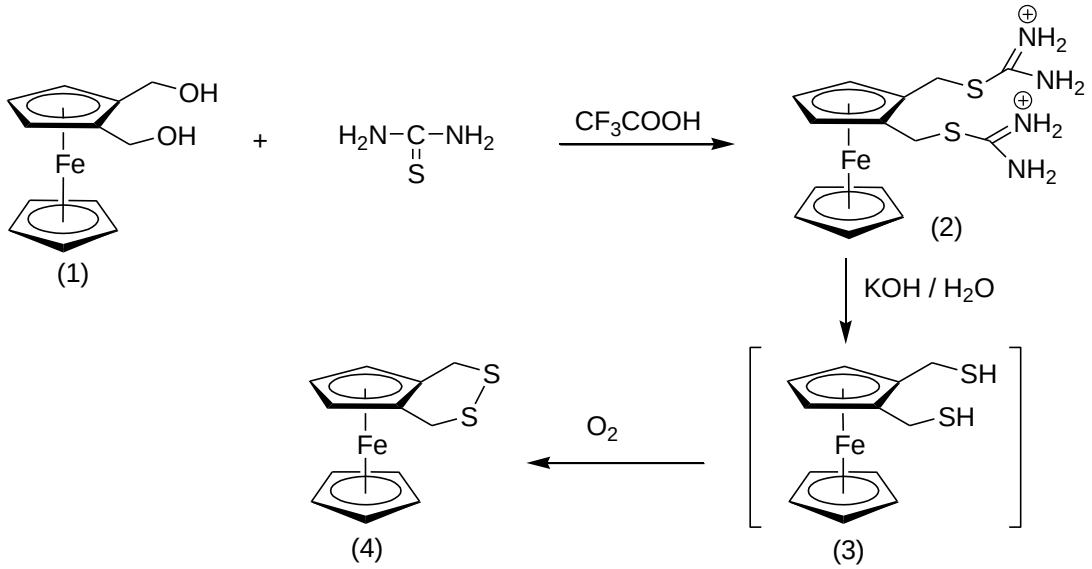

Scheme 1.8 Preparation of 1,4-dihydro-2,3-ferrocenodithiin[31,32]

1.3.2 Spectroscopy

New compounds were characterized by spectroscopic methods, including ^{1}H and ^{13}C NMR, MS and IR. The compound 1,4-dihydro-2,3-ferrocenodithiin has C–S bands at 649 cm^{-1} and 661 cm^{-1}, typical aromatic C–H stretching vibrations at 3000 cm^{-1} and above (variable), and C=C ring bands at about 1600 cm^{-1} (medium to weak). Strong to medium aromatic C–H bending vibrations is also present around 600–900 cm^{-1}. Fragmentation of all the new compounds was observed as expected. Fragmentation of 1,4-dihydro-2,3-ferrocenodithiin is as follows: 276(M^{+}), 212, 152, 121, 91, 77, 65, 56. Fragmentation of 2,16-dioxa[3.3](1,2)ferrocenophane: 456(M^{+}), 390, 362, 227, 200, 186, 128, 91, 73, 56. Fragmentation of 2,16-dithia[3.3](1,2)ferrocenophane: 488(M^{+}), 308, 307, 306, 304, 244, 241, 212, 186, 121, 91, 65, 56. ^{1}H NMR resonances of the unsubstituted cyclopentadienyl ring for all compounds lie in the range of 3.95 to 4.12 ppm as a characteristic singlet. The proton resonances of the substituted cyclopentadienyl ligand of all compounds display characteristic doublet and triplet with an integration of 2:1. ^{1}H NMR resonances of all compounds are listed in Table 1.1.

Table 1.1 Selected ^{1}H NMR spectroscopic data (ppm) for complexes

Complex	C_5H_5	C***H***CHC***H***	CHC***H***CH	CH_2	Solvent
1,4-dihydro-2,3-ferrocenodithiin	4.122	4.13	3.99	3.89, 3.59	$CDCl_3$
2,16-dioxa[3.3](1,2)ferrocenophane	3.98	4.41	4.29	4.34, 4.01	$CDCl_3$
2,16-dithia[3.3](1,2)ferrocenophane	3.95	4.39	4.16	3.35, 3.09	$CDCl_3$

1.3.3 Structure

The structures of complexes 2,16-dioxa[3.3](1,2)ferrocenophane, 2,16-dithia[3.3](1,2)ferrocenophane and 1,4-dihydro-2,3-ferrocenodithiin were determined by single X–ray crystallography. The compound 1,4-dihydro-2,3-ferrocenodithiin was crystallized as bright yellow-orange crystals by slow evaporation of hexane and ethyl ether at room temperature. Single crystals of 2,16-dioxa[3.3](1,2)ferrocenophane and 2,16-dithia[3.3](1,2)ferrocenophane were grown by slow evaporation of ethyl ether at room temperature. Molecular structures of 2,16-dioxa[3.3](1,2)ferrocenophane, 2,16-dithia[3.3](1,2)ferrocenophane and 1,4-dihydro-2,3-ferrocenodithiin with numbering are shown in Figures 1.4–1.6. The crystal structure and refinement data for these complexes are in Tables 1.2–1.5.

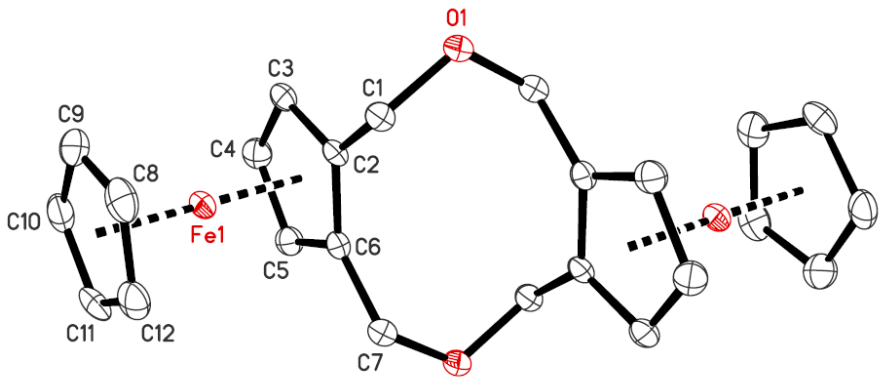

Figure 1.4 Crystal structure of 2,16-dioxa[3.3](1,2)ferrocenophane (1)

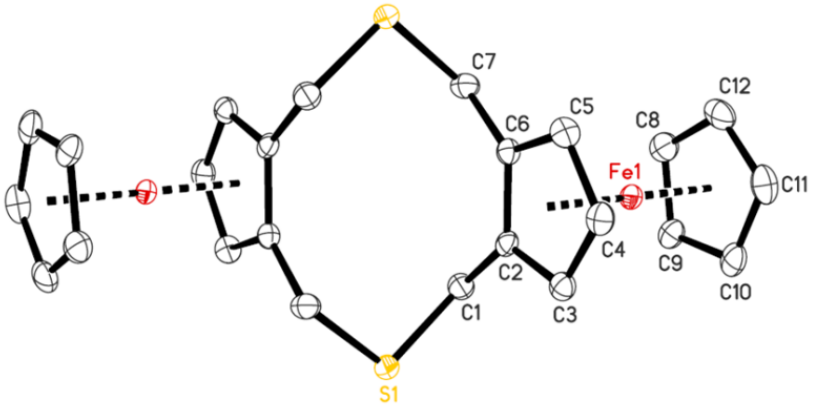

Figure 1.5 Crystal structure of 2,16-dithia[3.3](1,2)ferrocenophane (2)

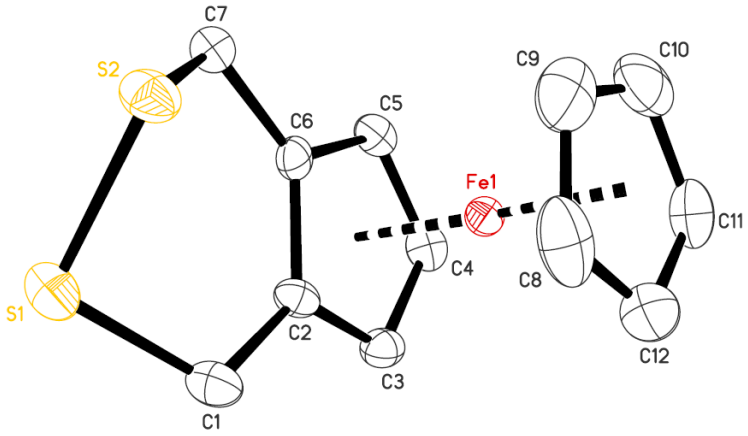

Figure 1.6 Crystal structure of 1,4-dihydro-2,3-ferrocenodithiin (3)

Table 1.2 Crystal Data and Structure Refinement for Compounds **1**, **2** and **3**.

Compound	**1**	**2**	**3**
Formula	$C_{24}H_{24}Fe_2O_2$	$C_{24}H_{24}Fe_2S_2$	$C_{12}H_{12}FeS_2$
Formula wt (amu)	456.13	488.25	276.19
T, K	90.0(2)	90.0(2)	90.0(2)
Crystal system	Monoclinic	Monoclinic	Orthorhombic
Space group	$P2_1/n$	$P2_1/n$	$Pbca$
Z	2	2	8
a, Å	11.0426(4)	10.5707(4)	10.6203(4)
b, Å	7.4969(3)	8.4321(3)	7.8144(3)
c, Å	12.0805(5)	12.2601(4)	26.2852(9)
α,(deg)	90	90	90
β, (deg)	112.1742(18)	114.422(1)	90
γ, (deg)	90	90	90
V, Å^3	926.12(6)	995.00(6)	2181.44(14)
d_{calc}, Mg/m^3	1.636	1.630	1.682
F(000)	472	504	1136
Crystal size (mm^3)	0.34 x 0.08 x 0.05	0.18 x 0.16 x 0.03	0.25 x 0.10 x 0.02
Radiation	Mo K_α (λ = 0.7107 Å)	Cu K_α (λ= 1.54178 Å)	Cu K_α (λ= 1.54178 Å)
Monochromator	Graphite	Graded Multilayer Optics	Graded Multilayer Optics
Absorption coef (mm^{-1})	1.584	13.691	14.312
Diffractometer	NoniusKappaCCD	Bruker X8 Proteum	Bruker X8 Proteum
Range (deg)	2.13 to 27.50	4.66 to 68.52	3.36 to 68.37
Limiting indices	$-14 \le h \le 14$	$-12 \le h \le 11$	$-12 \le h \le 12$
	$-9 \le k \le 9$	$0 \le k \le 10$	$-9 \le k \le 9$
	$-15 \le l \le 15$	$0 \le l \le 14$	$-31 \le l \le 31$
Reflections collected	18281	1814	24965
Independent reflections	2129 (R_{int} = 0.0650)	1814 (R_{int}= 0.0604)	1990 (R_{int} = 0.0850)
Absorption correction	Semi-empirical from equivalents	Semi-empirical from equivalents	Semi-empirical from equivalents
Refinement method	SHELXL-97	SHELXL-97	SHELXL-97
Refinement method	Full-matrix least-squares on F^2	Full-matrix least-squares on F^2	Full-matrix least-squares on F^2
Data/restraints/parameters	2129 / 0 / 127	1814 / 0 / 127	1990 / 0 / 136
Goodness-of-fit on F^2	1.079	1.059	1.167
Final R indices [I>2σ (I)]	R1 = 0.0311, wR2 = 0.0743	R1 = 0.0493, wR2 = 0.1382	R1 = 0.0662, wR2 = 0.1467
R indices (all data)	R1 = 0.0407, wR2 =	R1 = 0.0504, wR2 =	R1 = 0.0747, wR2 =

	0.0792	0.1405	0.1506
Largest diff. peak and hole	0.795 e•Å^{-3} and –0.461 e•Å^{-3}	0.875 e•Å^{-3} and –1.186 e•Å^{-3}	0.734 e•Å^{-3} and –0.703 e•Å^{-3}

Table 1.3 Bond Distances (Å) and Bond Angles (°) for 2,16-dioxa [3.3](1,2)ferrocenophane (1)

Atoms	Distance (Å)
Fe(1)–C(2)	2.0350(19)
Fe(1)–C(10)	2.036(2)
Fe(1)–C(6)	2.0367(19)
Fe(1)–C(3)	2.038(2)
Fe(1)–C(5)	2.040(2)
Fe(1)–C(4)	2.041(2)
Fe(1)–C(9)	2.043(2)
Fe(1)–C(8)	2.043(2)
Fe(1)–C(11)	2.046(2)
Fe(1)–C(12)	2.052(2)
O(1)–C(7)#1	1.430(2)
O(1)–C(1)	1.434(2)
C(1)–C(2)	1.502(3)
C(2)–C(3)	1.430(3)
C(2)–C(6)	1.433(3)
C(3)–C(4)	1.422(3)
C(4)–C(5)	1.421(3)
C(5)–C(6)	1.432(3)
C(6)–C(7)	1.492(3)
C(7)–O(1)#1	1.430(2)
C(8)–C(12)	1.413(3)
C(8)–C(9)	1.427(3)
C(9)–C(10)	1.417(3)
C(10)–C(11)	1.418(3)
C(11)–C(12)	1.427(3)
Atoms	Angle (°)
C(7)#1–O(1)–C(1)	114.42(15)
O(1)–C(1)–C(2)	113.21(17)
C(3)–C(2)–C(6)	107.64(18)
C(3)–C(2)–C(1)	124.81(18)
C(6)–C(2)–C(1)	127.54(18)
C(3)–C(2)–Fe(1)	69.55(11)
C(6)–C(2)–Fe(1)	69.46(11)
C(1)–C(2)–Fe(1)	125.55(14)
C(4)–C(3)–C(2)	108.35(18)
C(4)–C(3)–Fe(1)	69.72(12)
C(2)–C(3)–Fe(1)	69.33(11)
C(5)–C(4)–C(3)	108.08(18)
C(5)–C(4)–Fe(1)	69.59(11)
C(3)–C(4)–Fe(1)	69.48(11)
C(4)–C(5)–C(6)	108.24(18)
C(4)–C(5)–Fe(1)	69.65(12)
C(6)–C(5)–Fe(1)	69.30(11)
C(5)–C(6)–C(2)	107.68(18)
C(5)–C(6)–C(7)	124.68(18)
C(2)–C(6)–C(7)	127.59(18)
C(5)–C(6)–Fe(1)	69.57(11)
C(2)–C(6)–Fe(1)	69.34(11)
C(7)–C(6)–Fe(1)	124.50(14)
O(1)#1–C(7)–C(6)	113.96(17)
C(12)–C(8)–C(9)	108.3(2)
C(12)–C(8)–Fe(1)	70.15(12)
C(9)–C(8)–Fe(1)	69.56(12)
C(10)–C(9)–C(8)	107.7(2)
C(10)–C(9)–Fe(1)	69.41(13)
C(8)–C(9)–Fe(1)	69.57(13)
C(9)–C(10)–C(11)	108.3(2)
C(9)–C(10)–Fe(1)	69.94(12)
C(11)–C(10)–Fe(1)	70.03(12)
C(10)–C(11)–C(12)	107.9(2)
C(10)–C(11)–Fe(1)	69.32(12)
C(12)–C(11)–Fe(1)	69.87(12)
C(8)–C(12)–C(11)	107.8(2)
C(8)–C(12)–Fe(1)	69.47(12)
C(11)–C(12)–Fe(1)	69.38(12)

Table 1.4 Bond Distances (Å) and Bond Angles (°) for 2,16-dithia[3.3](1,2)ferrocenophane (2)

Atoms	Distance (Å)
Fe(1)–C(3)	2.035(3)
Fe(1)–C(9)	2.036(3)
Fe(1)–C(4)	2.039(3)
Fe(1)–C(6)	2.042(3)
Fe(1)–C(8)	2.044(3)
Fe(1)–C(11)	2.047(3)
Fe(1)–C(2)	2.049(3)
Fe(1)–C(5)	2.049(3)
Fe(1)–C(12)	2.051(3)
Fe(1)–C(10)	2.055(4)
S(1)–C(1)	1.807(3)
S(1)–C(7)#1	1.810(3)
C(1)–C(2)	1.491(4)
C(2)–C(3)	1.432(4)
C(2)–C(6)	1.439(4)
C(3)–C(4)	1.418(4)
C(4)–C(5)	1.424(4)
C(5)–C(6)	1.435(4)
C(6)–C(7)	1.500(4)
C(7)–S(1)#1	1.810(3)
C(8)–C(12)	1.420(5)
C(8)–C(9)	1.426(5)
C(9)–C(10)	1.430(5)
C(10)–C(11)	1.419(5)
C(11)–C(12)	1.418(5)
Atoms	Angles (°)
C(1)–S(1)–C(7)#1	101.72(14)
C(2)–C(1)–S(1)	114.0(2)
C(3)–C(2)–C(6)	107.1(2)
C(3)–C(2)–C(1)	125.9(3)
C(6)–C(2)–C(1)	127.1(3)
C(3)–C(2)–Fe(1)	68.97(16)
C(6)–C(2)–Fe(1)	69.17(16)
C(1)–C(2)–Fe(1)	126.9(2)
C(4)–C(3)–C(2)	108.6(3)
C(4)–C(3)–Fe(1)	69.76(17)
C(2)–C(3)–Fe(1)	69.98(16)
C(3)–C(4)–C(5)	108.5(3)
C(3)–C(4)–Fe(1)	69.51(16)
C(5)–C(4)–Fe(1)	70.00(17)
C(4)–C(5)–C(6)	107.6(3)
C(4)–C(5)–Fe(1)	69.23(17)
C(6)–C(5)–Fe(1)	69.21(16)
C(5)–C(6)–C(2)	108.2(2)
C(5)–C(6)–C(7)	124.9(3)
C(2)–C(6)–C(7)	126.9(3)
C(5)–C(6)–Fe(1)	69.71(17)
C(2)–C(6)–Fe(1)	69.66(15)
C(7)–C(6)–Fe(1)	125.2(2)
C(6)–C(7)–S(1)#1	114.7(2)
C(12)–C(8)–C(9)	107.9(3)
C(12)–C(8)–Fe(1)	70.00(18)
C(9)–C(8)–Fe(1)	69.26(18)
C(8)–C(9)–C(10)	107.9(3)
C(8)–C(9)–Fe(1)	69.82(18)
C(10)–C(9)–Fe(1)	70.23(18)
C(11)–C(10)–C(9)	107.6(3)
C(11)–C(10)–Fe(1)	69.5(2)
C(9)–C(10)–Fe(1)	68.86(18)
C(12)–C(11)–C(10)	108.5(3)
C(12)–C(11)–Fe(1)	69.92(19)
C(10)–C(11)–Fe(1)	70.03(19)
C(11)–C(12)–C(8)	108.1(3)
C(11)–C(12)–Fe(1)	69.62(18)
C(8)–C(12)–Fe(1)	69.42(18)

Table 1.5 Bond Distances (Å) and Bond Angles (°) for 1,4-dihydro-2,3-ferrocenodithin (3)

Atoms	Distance (Å)
Fe(1)–C(8)	2.022(7)
Fe(1)–C(12)	2.033(8)
Fe(1)–C(6)	2.035(6)
Fe(1)–C(9)	2.037(7)
Fe(1)–C(10)	2.042(7)
Fe(1)–C(4)	2.046(6)
Fe(1)–C(5)	2.047(6)
Fe(1)–C(3)	2.048(6)
Fe(1)–C(11)	2.049(7)
Fe(1)–C(2)	2.055(6)
S(1)–C(1)	1.816(7)
S(1)–S(2)	2.046(2)
S(2)–C(7)	1.820(6)
C(1)–C(2)	1.496(8)
C(2)–C(3)	1.420(8)
C(2)–C(6)	1.431(8)
C(3)–C(4)	1.432(9)
C(4)–C(5)	1.415(9)
C(5)–C(6)	1.427(8)
C(6)–C(7)	1.502(8)
C(8)–C(9)	1.378(13)
C(8)–C(12)	1.414(11)
C(9)–C(10)	1.393(12)
C(10)–C(11)	1.393(11)
C(11)–C(12)	1.389(10)
Atoms	Angles (°)
C(1)–S(1)–S(2)	99.0(2)
C(7)–S(2)–S(1)	98.6(2)
C(2)–C(1)–S(1)	113.3(5)
C(3)–C(2)–C(6)	107.4(5)
C(3)–C(2)–C(1)	125.0(6)
C(6)–C(2)–C(1)	127.5(5)
C(3)–C(2)–Fe(1)	69.5(3)
C(6)–C(2)–Fe(1)	68.8(3)
C(1)–C(2)–Fe(1)	127.7(4)
C(2)–C(3)–C(4)	108.4(5)
C(2)–C(3)–Fe(1)	70.0(3)
C(4)–C(3)–Fe(1)	69.4(3)
C(5)–C(4)–C(3)	107.8(5)
C(5)–C(4)–Fe(1)	69.8(3)
C(3)–C(4)–Fe(1)	69.6(3)
C(4)–C(5)–C(6)	108.2(5)
C(4)–C(5)–Fe(1)	69.7(4)
C(6)–C(5)–Fe(1)	69.1(3)
C(5)–C(6)–C(2)	108.1(5)
C(5)–C(6)–C(7)	124.4(6)
C(2)–C(6)–C(7)	127.4(5)
C(5)–C(6)–Fe(1)	70.0(3)
C(2)–C(6)–Fe(1)	70.3(3)
C(7)–C(6)–Fe(1)	125.9(4)
C(6)–C(7)–S(2)	112.2(4)
C(9)–C(8)–C(12)	107.3(7)
C(9)–C(8)–Fe(1)	70.8(4)
C(12)–C(8)–Fe(1)	70.0(4)
C(8)–C(9)–C(10)	108.5(7)
C(8)–C(9)–Fe(1)	69.5(4)
C(10)–C(9)–Fe(1)	70.2(4)
C(9)–C(10)–C(11)	108.6(7)
C(9)–C(10)–Fe(1)	69.9(4)
C(11)–C(10)–Fe(1)	70.4(4)
C(12)–C(11)–C(10)	107.3(7)
C(12)–C(11)–Fe(1)	69.5(4)
C(10)–C(11)–Fe(1)	69.8(4)
C(11)–C(12)–C(8)	108.4(7)
C(11)–C(12)–Fe(1)	70.7(4)
C(8)–C(12)–Fe(1)	69.2(4)

1.4 Summary and Future Work

Exploring a shorter synthetic route to starting material, 1,2-di(hydroxymethyl)ferrocene was the first task. This was followed by attempts to synthesize an important precursor, 1,3-dihydroferroceno[*c*]thiophene, to our target molecule, ferroceno[*c*]thiophene. We reacted 1,2-di(hydroxymethyl)ferrocene with H_2S/H_2SO_4 and Na_2S/HBF_4 respectively. Reaction of 1,2-di(hydroxymethyl)ferrocene with either H_2S/H_2SO_4 or Na_2S/HBF_4 resulted in 2,16-dithia[3.3](1,2)ferrocenophane instead of monomeric 1,3-dihydroferroceno[*c*]thiophene. Dehydration of 1,2-di(hydroxymethyl)ferrocene with dilute H_2SO_4 resulted in 2,16-dioxa[3.3](1,2)ferrocenophane. Thus, in order to achieve our target molecule, 1,3-dihydroferroceno[*c*]thiophene, we decided to pursue the route with 1,4-dihydro-2,3-ferrocenodithin being the precursor to our final target molecule. 1,2-Di(hydroxymethyl)ferrocene reacts with thiourea in the presence of catalytic trifluoroacetic acid to give a water-soluble thiouronium salt, which reacts with aqueous potassium hydroxide in air to give 1,4-dihydro-2,3-ferrocenodithin, via oxidation of the intermediate 1,2-di(mercaptomethyl)ferrocene. This project was further pursued by a coworker.[33] The desired end product, ferrocene–fused thiophene monomer, hasn't been obtained yet. Further optimization of synthetic pathway to the target molecule is needed. Investigation into polymerization (electrochemical and chemical) is the next logical step

once the monomer (aromatic or quinoid form) is achieved. When synthesized, polymerization of 1,3-dihydroferroceno[*c*]thiophene will give the Type II polymer. This will be the simplest metallocene-fused thiophene polymer of Type II. This will open a new route to synthesize Fe thiophene complexes. Future work will also involve study of electronic and electrochromic properties and changing other conjugated substituents to obtain different forms of metallocene-fused thiophene polymer.

Chapter 2 Introduction to Development of Carbonic Anhydrase Active-site mimics for CO_2 hydration

2.1 Increasing Carbon Dioxide Levels in Atmosphere

Fundamentals for habitability of terrestrial planets followed by emergence and creating habitable zones has been studied by Kathryn *et al*.[34] Several computational models discussed by Luisa *et al* [35] exhibits the condition for a habitable zone on a planet. The atmospheric temperature and pressure are key variables that make earth different from other planets. The chief terrestrial greenhouse gases are water vapors and carbon dioxide which clearly governs the earth atmospheric temperature. Since, water vapors condense and precipitate actively, they are identified as fast feedback processes in the ecosystem. However, carbon dioxide, similar to N_2O, ozone, CH_4 and chlorofluorocarbons, does not condense or precipitate from the atmosphere and thus, pose serious threat levels.[36] Air bubbles trapped in the ice at Antarctica region, measured for carbon dioxide ppm levels are found to be the highest in recent years. Furthermore, Mauna Loa record installed at Hawai has shown extremely high CO_2 ppm levels above 400 ppm.[37-38] High ppm levels raise concerns over reduction and control of atmospheric CO_2 as compared to thousands of years. Since 1970s, daily CO_2 trend was recorded and raised concerns among researchers about increasing CO_2 levels.[37-38] Winter ages were recorded with 200 ppm while warmer periods recorded with 280 ppm, this trend

identified throughout 400,000 years prior to 1950s. In 1958, the month of June was recorded with a ppm of 317.10 as compared to 408.84 ppm in June of 2017. There is a consistent upward trend of 91.74 ppm within last 59 years as compared to an upward and downward trend that was present before 1950s.[39] Human activities mainly burning of fossil fuels but not limited to deforestation and industrial activity, cause the ppm levels of carbon dioxide to increase. Carbon present in fossil fuels get mixed with atmospheric oxygen resulting in formation of CO_2. Ultimately, increased CO_2 is directly proportional to increased greenhouse gas effect. An interagovernment panel on climate change called as IPCC, in 2014 has demonstrated the global emissions of key greenhouse gases with CO_2 consisting of 75% followed by CH_4, NO_2 and F-Gases consisting of 25%.[40] There is a concern whether solar rays from sun are manipulating earth's atmospheric temperature. Scientific studies have shown that variation in solar energy has affected climate on earth.[41-42]

Based up on scientific facts, it has been ruled out that sun is the reason behind changing the climate on earth. In addition, if climate has to be extremely affected by the sun then all the layers of the atmosphere should have exhibited similar temperature zones as compared to cooler temperature levels in upper layer while warmer towards surface or lower levels of atmosphere. Temperatures measured in stratospheric levels by NOAA between 1979-2016 has not shown a major difference to demonstrate that solar activity is

a reason behind increasing atmospheric temperatures in stratosphere. It has been concluded that there is more than 95% probability that raised CO_2 levels have occurred due to human activity.[40] At 1 hPA, with measurement location at 90N-65N Latitudes with a range of 55 km from earth's surface, mean temperature is measured between 5 ºC during July 1979 and -20 ºC during months of January 1979 as compared to similar temperatures in relative months of 2016.[43] It is clearly evident that lower levels in atmosphere produce greenhouse effect and trap CO_2 causing increase in atmospheric temperature. Global land-ocean temperature monitoring atmospheric temperatures reflect 0.99 ºC increase compared to 1950-1980 levels.[44] Further details shown by GISTEMP, the warmer each month than the annual global mean, August 2017 is 2.15 ºC warmer than August 1880.[45-46] In 1881, Hansen *et al*[46] concluded that global temperature rose between 0.2 ºC during 1960-1980s, yielding a warming of 0.4 ºC in past century. This change in temperature consistently correlates with increasing measured CO_2 levels in troposphere.

2.2 CO_2 Emissions in the United States and the World

Global emissions of CO_2 are mainly contributed by China 30%, US 15%, European Union 9%, India 7%, Russia 5% and Japan 4% and rest of the world 30%.[40, 47] In the United States, 6586.7 million metric tonnes of CO_2 Equivalent Greenhouse Gas emissions were noted in 2015[48], a total of 3.5% increase from 1990 to 2015 in

greenhouse gas emissions. However, in 2015 CO_2 emissions were noticed with a 2.3% decrease from 2014. Several key factors contributed to the decrease including transition from coal to natural gas in electricity generation and warmer winter conditions reduced electricity & heating fuel consumption. In 2015, CO_2 emissions consist of 82.2% of overall US emissions of GHG from human activities with electricity generation and consumption contributed 35% followed by 32% and 15% contribution from Transportation and Industry sectors respectively. Extensive combustion of fossil fuels resulted with 5049.8 MMT Equivalent CO_2 emissions out of total of 6586.7 MMT GHG emissions in 2015.[48] The effect of increased CO_2 levels has been seen clearly with glaciers been shrunk, ice melting earlier, plant and animal ranges shifted, sea level rise and more intense heat waves. Sea level has rose to 8 inches globally since 1880s[40] and expected to increase between 1-4 feet by 2100. In United States, climate change impacts have been noted by the United States Global Research Program. A 2014 Third Climate Assessment[49] exhibited impact of rising CO_2 levels on oceans and land. As oceans absorb CO_2, their acidic level starts increasing because of formation of carbonic acid. Ocean waters have become acidic with 30% increase in acidity in last 250 years which directly impacts the corrosiveness in water and marine food chain.[50] Extreme impacts of climate change are expected in different parts of the United States. South-East and Carribean region where the state of Kentucky region lies is projected with decreased availability of

water and increase in hurricanes.[49] Definitely, GHG emissions linked to human activity must be reduced with effective and sustainable methods. As discussed above, CO_2 is a key GHG which must be primarily addressed. The robust way to reduce CO_2 emissions is to reduce the consumption of fossil fuels. In 1990, the key CO_2 generation sector was electricity generation from power plants utilizing fossil fuels mainly coal powered plants. It comprised of 52% electric generation followed by 12% Natural Gas and remaining coming from other sources.[51] However, strict environmental rules and regulations lead towards prematurely retirement of few coal powered plants. In addition, cheaper natural gas prices driven by shale gas availability drove increased availability and consumption of natural gas which resulted in future power plants designed for natural gas. In 2016, fossil fuels accounted for 65% share in electricity generation with natural gas dominated electric generation at 34%, coal 30%, nuclear 20% followed by renewable 15% and other sources.[51] In 2017 EIA Energy Conference meeting identified the completion of coal vs natural gas where pricing and reliability has been discussed. Reliability of Natural Gas is still in question since events similar to polar vortex in 2014 limited the availability of natural gas which ultimately raised the prices. Natural gas does carry more risk of methane leakage during extraction process. The key CO_2 reduction strategy lies with switching to alternate non-fossil fuels and Carbon Capture and Storage (CCS). Non-fossil fuels are mainly renewable sources of energy such as Wind, Hydropower and Solar and

are cleaner. However, application of renewable energies suffers the limitation that they are not as reliable as coal for e.g. calm days may cut off the continuous wind supply; droughts greatly affect hydropower; weather conditions limit solar energy collection. Backup plants driven by fossil fuels are required to take over when the renewable energy sources are interrupted. In addition, the transition from fossil fuels to the clean energy technologies requires considerable modifications of existing power plants which involves huge capital investment. Carbon Capture and Storage (CCS) is an important method to reduce carbon emissions into the atmosphere since combustion of fossil fuels is still a major source of energy generation for human activities, before a more environmentally sustainable energy generation infrastructure is available.

2.3 Carbon Capture and Storage (CCS)

The basic fundamental goal is to capture carbon and prevent it to be released in the atmosphere. CCS is a process that enable the capture of carbon dioxide (CO_2) from fuel combustion or industrial processes, then transportation of CO_2 via ships or pipelines, and its storage underground, in depleted oil and gas fields and deep saline formations.[52] International Energy Agency released a report in 2016 highlighting the status over two decades of carbon capture and storage.[53] CCS is classified into pre-combustion, post-combustion and oxy-fuel combustion process. Abanades *et al*[54] has mentioned emerging

CO_2 capture systems by referencing capture toolbox identified in IPCC 2005 report.[55] IPPC break down pre, post and oxy fuel combustion in further details and classified carbon capture systems as absorption, cryogenics, high temperature solid looping, solid sorbents and membranes. The concentration of CO_2 in the gas stream, the pressure of the gas stream and the fuel type (solid or gas) are important factors in selecting the capture system.[56] A 2014 Technological readiness Assessment Report identified the technology readiness level (TRL) of several carbon capture processes. Carbon capture systems are discussed in next sections of this chapter.

2.3.1 Pre-combustion Carbon Capture

Pre-combustion process involves processing of fuel with air or oxygen into a steam reactor to produce a mixture of carbon monoxide and hydrogen gas which together is called a synthesis or syngas.[56] In next steps, carbon monoxide and steam react again in a shift convertor or catalytic reactor which generates additional hydrogen and CO_2. CO_2 is then separated from hydrogen using a chemical or physical absorption process. Hydrogen can be used as fuel for power generation and CO_2 is compressed and transported for storage. Jansen *et al*[57] focused on pre-combustion CO_2 capture from natural gas combined capture cycles (NGCC) and Integrated gasification combined cycles (IGCC) for power generation. The key element of pre-combustion is synthesis gas or syngas.[58] Syngas composition varies depending on type of fuel utilized. It can be

produced through steam reforming where steam is added to primary fuel. Another method is partial oxidation where gaseous and liquid fuels are utilized as primary fuel. As compared to solid fuel as a primary fuel, the term is called as gasification, to produce syngas. Syngas produced with coal through gasification process typically consists of 30~60% of carbon monoxide, 25 to 30% of H_2 gas, 0 to 5% CH_4, 5 to 15% CO_2 followed by varying amount of water vapor, minor traces of hydrogen sulfide (H_2S), carbonyl sulfide (COS), ammonia (NH_3) and few contaminants.[59] Higman and burgt[60-65] mentioned the detailed gasification process including the thermodynamics and kinetics of gasification process. Practical issues were reported such as contaminated syngas. Additional treatment of the flue gas may be needed to remove air pollutants and non-condensed gases (such as nitrogen) from the flue gas before the CO_2 is sent to storage.

2.3.2 Oxyfuel Combustion

Oxyfuel combustion involves O_2 instead of air for combustion of the primary fuel to produce a flue gas consisting mainly of water vapor and CO_2. As a result, flue gas with high CO_2 concentrations (greater than 80% by volume) is produced. The water vapor is then removed by cooling and compressing the gas stream.[56] Oxygen is the main element of oxyfuel combustion since it requires a purity of 95–99% oxygen assumed in most current designs. An upstream oxygen separation process from air is required which results in additional emissions. Oxyfuel systems are also being studied in gas turbine

systems, but conceptual designs for such applications are still in the research phase. Stanger *et al* [66] primarily focused on the development of the boiler and gas turbine (GT) with Oxy-GT combustion as an emerging option for capturing the emissions from natural gas combined cycles, with the pre-combustion capture technology related to coal gasification. In case of coal fired oxy-combustion, the Air Separator Unit and CO_2 Processing Unit are the main components which consumed additional energy. The higher efficiencies of the combined cycles are expected to manage an overall efficiency of 44-59%. Oxygen must be supplied at high pressure and different cycles are currently being investigated. Oxy-GT technology is currently in development at small pilot scale with tests on-going for a large scale implementation (i.e. CES cycle).[66]

2.3.3 Post-combustion Carbon Capture

Post-combustion process involves capturing of flue gas produced after combustion of fuel by absorbing flue gas into a suitable liquid solvent. The concentration range of the components of flue gas varies for different combustion processes and coals. Flue gas contains mainly nitrogen and 3~15% of CO_2 by volume. Typical concentration generated from bulk species include 76–77 vol% N_2, 10–14 vol% CO_2, 4–16 vol% H_2O, and 2–6 vol% O_2 and also different combustion by products, such as 5–100 ppmv HCl, 2 gr/dscf fly ash and sulfur and nitrogen oxides (500–3000 ppmv SO_2, 5–60 ppmv SO_3, 50–300 ppmv NO and 10–40 ppmv NO_2).[67-68] Conventionally, chemical or physical

absorption has been utilized to perform solvent based post combustion absorption. Deschermeier *et al* focused-on characterization of solvents for physical absorption process. Physical Absorption process consists of absorption of acidic gases such as CO_2 with solvent, desorption includes separation of solute from solvent stream and regeneration of solvent back to absorption process after adjusting its temperature and pressure.[69] Physical Absorption has an advantage over chemical absorption as no chemical reaction is invlolved.[70]

Oko *et al* identified chemical absorption post combustion technology with solvent based carbon capture as a key near term technical and commercial option highlighting the current and future status of PCC implementation.[71] Pulverized Coal and NGCC Power Plants would typically utilize monoethanolamine (MEA) as an organic solvent.[56] Sask Power Boundary Dam Carbon Capture project is a good example of post combustion carbon capture technology. In 2014, boundary dam became the first full scale post combustion capture coal fired powered power plant to demonstrate successful use of CCS technology with a full capacity of 1 Mpta CO_2.[53] Captured carbon was transported 3.2 kilometers below the earth's surface and captured safely in a layer of brine filled sandstone, also called as deadwood formation.[72] Cebrucian *et al*[73] reviewed the performance of large scale power plants installed or upcoming projects with carbon capture, and presented development and demonstration status of current carbon capture

activities. Unfortunately, CCS application may reduce the net efficiency of a power plant by up to 14% points thereby increasing the electricity generation costs by 30-70%. As far as output and optimization of post combustion capture process, Oexmann *et al*[74] discussed about the heat requirement for solvent regeneration that contributed towards the largest impact on the power output of the overall process, the optimal process parameters required for the lowest possible heat requirement of the capture unit do not necessarily coincide with the optimal process parameters that make for the most energy efficient operation of the overall capture process. Therefore, when optimizing process parameters of CO_2 absorption processes in power plants, a key focus should be inclined towards the minimization of the overall power loss instead of solely reducing the heat requirement for solvent regeneration. As part of improvement and separation of CO_2 capture, Soong *et al* initiated a study to develop amine enriched solid sorbents. Their results preliminary exhibited a capability of CO_2 capture while sorbents are regenerable.[75] Dabrowski *et al* presented current status of application and characterization of new environmental sorbents.[76] Since current carbon dioxide capture methods result in corrosivity and heat losses, Vericella *et al* proposed microencapsulation by creating microencapsulated carbon sorbents.[77] Tachy *et al* worked on a hybrid model to combine amines and membranes during chemical absorption process since amines are one of the best solvent in chemical absorption process due to higher purity of CO_2 capture.[78] In

addition to solvent, sorbent and membrane based post carbon combustion technologies; other novel concepts evolved such as hybrid models and CO_2 adsorption. Kim *et al* presented an experimental data exhibiting measurements of heat of adsorption of CO_2 using aqueous MEA based solvent and partial pressure of CO_2 with a calorimeter.[79] Choma *et al* developed four nanoporous carbons from polymers which exhibited developed microporosity and exceptional CO_2 adsorption.[80]

Out of three technological pathways for CO_2 capture from combustion of fossil fuels: pre-combustion capture, post-combustion capture, and oxyfuel combustion,[5] post combustion capture has been used on an industrial scale for decades in certain applications, and is being further developed for broader use due to the fact that it can be retrofitted to existing power plants with minimal modification, though the corresponding energy penalty is high. Chemical absorption has been discussed further with aqueous amines as focus of solvent based carbon capture.

2.3.3.1 Chemical Absorption

Chemical absorption systems at present are the preferred option for post-combustion capture of CO_2. Most existing post-combustion CO_2 capture systems are related to chemical absorption/desorption using aqueous solvents such as alkanolamines, and have been practiced for gas cleanup applications since 1930.[81] In the process, CO_2 is separated from the flue gas by passing the flue gas through a continuous scrubbing

system. The system consists of an absorber (also called scrubber) and a desorber (also called stripper, regeneration tower). Absorption processes utilize the reversible chemical reaction of CO_2 with an aqueous alkaline solvent, usually an amine. Flue gas is fed into the CO_2 absorber at the bottom and ascending through the column. In order to assure an efficient gas-liquid contact in the absorber column, the column is filled with metal structured packing. CO_2 lean solution enters into the absorber at the top and passes through the packing materials. At a temperature of 40–50 °C, CO_2 is absorbed during the countercurrent contact with the absorbent solution, which becomes carbon-rich in the bottom of the absorber. In the desorber, a higher temperature (usually 100–140 °C depending on the thermal stability of the absorbent) is applied to the CO_2 rich solution.[82-83] The absorbed CO_2 is stripped from the CO_2 rich solution and a pure stream of CO_2 is then dried and pressurized to 100–150 bar and sent for compression while the regenerated solvent is sent back to the absorber for further CO_2 absorption after cooling down in the heat exchanger.

A key issue of solvent based capture systems is the heat requirement for solvent regeneration, which significantly reduces the net power output of the power plant.[84] Heat is required in the reboiler to heat up the solvent to the required temperature to strip CO_2 and to produce steam in order to establish the required driving force for CO_2 stripping from the solvent. This leads to the main energy penalty on the power plant. In addition,

energy is required to compress the CO_2 to the conditions needed for storage and to operate the pumps and blowers in the process. Therefore, for economic reasons, the solutions for CO_2 absorption should have the advantages of (a) large capacity for CO_2; (b) capable of being regenerated using minimal energy; and (c) a high specific absorption rate.[85]

Potassium carbonate-bicarbonate solution is a common absorbent to capture CO_2 with high vapor pressure from natural gas or petroleum refinery process since it is moderately alkaline and undergoes slight change in pH during the absorption process,[86-87] has negligible volatility and degradation, and possesses the higher solubility of potassium bicarbonate. However, its slow reaction kinetic almost counter-balance all these benefits when applying to low vapor pressure CO_2 stream such as post-combustion utility flue gas stream. On another hand, considering these advantages potassium carbonate based solvents remain of interest for post-combustion-CO_2 absorption[88] particularly with a promoter.[89-90]

Alkanolamines are one of the best absorbents to separate CO_2 from gas streams in a chemical absorption process. Primary and secondary alkanolamines react with CO_2 to form carbamate $RNHCOO^-$ as shown below. The tertiary amines and hindered amines form the bicarbonate ion in a reaction with water as they do not possess an N–H bond, which is required in carbamate formation (Equations 1, 2 and 3).

$$CO_2 + 2RNH_2 \rightleftarrows RNHCOO^- + RNH_3^+ \quad 1$$

$$CO_2 + R_3N + H_2O \rightleftarrows HCO_3^- + R_3NH^+ \quad 2$$

$$CO_2 + H_2O \rightleftarrows H_2CO_3 \ (H^+ + HCO_3^-) \quad 3$$

According to Davidson, Trachtenberg and Bao,[91] the absorption capacity of tertiary amines is twice that of primary or secondary amines; however, the rate of absorption is lower. Key alkanolamines used in industrial capture of CO_2 are primary amines such as mono-ethanolamine or MEA and diglycolamine or DGA, secondary amines diethanolamine or DEA and diisopropanolamine or DIPA and the tertiary amines methyldiethanolamine or MDEA and triethanolamine or TEA.[81] The most widely studied alkanolamine in post-combustion CO_2 capture is monoethanolamine (MEA). It is a primary amine with several advantages over other alkanolamines, such as fast CO_2 absorption kinetics, favorable physical properties and relatively low cost. Conventionally, 30 wt% MEA aqueous solution has been considered as a benchmark CO_2 absorbent in industry. Prakash and Eugeny provided a detailed overview of recent studies completed on kinetics of reaction of CO_2 with aqueous solutions of alkanolamines.[92] There are implications of producing MEA on global scale since it requires production of Ammonia (NH_3) and Ethylene Oxide (EO) which finally reacts to produce MEA. This whole process includes direct and indirect CO_2 emissions.[93] The viscosity of MEA is usually high causing difficulty in generating large surface areas of fast absorption of CO_2. Aines

et al has developed an encapsulated form of carbon capture solvents where amines or carbonate is enclosed in a thin polymer shell forming a 200~400μm beads thereby increasing absorption surface area.[94]

2.4 Importance of Catalysts for CO_2 Capture and Storage

Capturing and compressing CO_2 with CCS requires much energy. These and other system costs are estimated to increase the cost of the overall CCS process by more than 80% for a unit with alkanolamine-based CO_2 capture.[95-96] Hence, optimizing the rate of CO_2 hydration (for capture) and dehydration (for release) can reduce the overall costs of energy production. To discover a catalyst that could enhance the rate of hydration and dehydration reaction of CO_2 is of major importance. Naturally occurring enzymes, e.g. carbonic anhydrase (CA) and carboxypeptidases, catalyzes these reactions in living systems.

2.5 Carbonic Anhydrase and its Mechanism

In biological systems, CO_2 hydration is essential in maintaining acid-base balance in blood, transporting carbon dioxide out of tissues, nerve signaling and numerous other processes. Because the uncatalyzed hydration of CO_2 is too slow to keep up with respiration in living systems, nature has developed the carbonic anhydrase enzymes to speed up the reaction (and its reverse) to essentially the limit of diffusion control.

Carbonic anhydrase (CA) is one of the fastest enzyme found in plants and animals that accelerates CO_2 hydration converting CO_2 to bicarbonate and the reverse bicarbonate dehydration drastically.

$$CO_2(g) + H_2O(l) \rightleftarrows H^+(aq) + HCO_3^-(aq) \qquad (1)$$

The most active enzymes, human carbonic anhydrase II, hydrate CO_2 at rates as high as $k_{cat} = 10^6\ s^{-1}$. Molar mass of carbonic anhydrase is around 30,000 Da with a Zn^{II} ion located at the active site, coordinated by three imidazoles groups of histidine amino acid residues and a water/hydroxide, resulting in distorted tetrahedral geometry.[97] The water ligand is polarized by the zinc ion, shifting its pK_a into physiological range. The active site steers carbon dioxide to the bound hydroxide, facilitating nucleophilic attack and a proton shift to form bicarbonate. Activity of CA is pH dependent. At pH 8, the reaction proceeds near its maximal rate. As the pH decreases, the rate of the reaction drops. The midpoint of this transition is near pH 7, suggesting that a group with pK_a = 7 plays an important role in the activity of carbonic anhydrase and that the deprotonated (high pH) form of this group participates more effectively in catalysis. Although some amino acids, notably histidine, have pK_a values near 7, a variety of evidence suggests that the group responsible for this transition is not an amino acid but is the zinc-bound water molecule. Thus, the binding of a water molecule to the positively charged zinc center reduces the pK_a of the water molecule from 15.7 to 7. With the lowered pK_a, a substantial

concentration of hydroxide ion (bound to zinc) is generated at neutral pH. A zinc-bound hydroxide ion is sufficiently nucleophilic to attack carbon dioxide much more readily than water does. The importance of the zinc-bound hydroxide ion suggests a simple mechanism for carbon dioxide hydration.

1) Zinc facilitates the release of a proton from a water molecule, which generates a hydroxide ion.

2) The carbon dioxide substrate binds to the enzyme's active site and is positioned to react with the hydroxide ion.

3) The hydroxide ion attacks the carbon dioxide, converting it into bicarbonate ion.

4) The catalytic site is regenerated with the release of the bicarbonate ion and the binding of another molecule of water.

There are many different types of carbonic anhydrase enzymes, with the potential to develop improved enzymes depending on what the process requires. The reaction and the catalytic activity of carbonic anhydrase have been widely studied for their physiological importance using certain very pure enzymes.[98-99] Tsao,[100] Alper,[101-102] and Donaldson[103] investigated CO_2 absorption in the presence of carbonic anhydrase enzyme in the stirred cell and the wetted wall column with pure CO_2. These studies were aimed to collect kinetic data about the catalytic activity of carbonic anhydrase on CO_2 absorption and so solution concentration was not as high. For example, Tsao employed 0.2 M

phosphate buffer solution with pH=7, and Alper and Deckwer used 0.2 M phosphate buffer solutions (pH=6.6 and 11) and 0.5 M carbonate buffer solution (pH=9.6) in the presence of crude carbonic anhydrase for their CO_2 absorption studies.

Recently, attentions have been paid on utilization of enzyme carbonic anhydrase on the CO_2 capture and sequestration from evolved stream of fossil fuels combustion, where carbonic anhydrase was used to increase the CO_2 absorption rate. Researcher at New Mexico Institute of Mining and Tech. have developed of system resembling a CO_2 scrubber, in which carbonic anhydrase catalyzed the rate of CO_2 hydration for subsequent geologic fixation into stable mineral carbonates for CO_2 sequestration.[104-105] Immobilized carbonic anhydrase (CA)-based CO_2 separation processes are currently under development. Carbozyme Inc. employed a membrane-contained CA enzyme process to capture CO_2 from flue gas with CO_2 concentration range of 1%-20%.[91] Dilmore *et al.* developed a novel concept of a CA-facilitated CO_2 absorption with regenerable amine-bearing polyacrylamide buffering beads (PABB).[106] CO_2 Solution Inc. of Montreal, Quebec, Canada, has patented a CO_2 capture process from flue gas using enzyme carbonic anhydrase. This system was based on a packed-bed aqueous CO_2 scrubber, where CA was fixed to a solid support, and increased the CO_2 absorption rate of aqueous amine solutions.[107]

2.6 Goal of this Project

Carbonic anhydrase is typically not stable at the high temperatures used during the solvent regeneration process for CO_2 capture, making it important to design robust, synthetic catalysts for CO_2 fixation. Our basic thought started with selecting a molecule that could mimic the enzyme carbonic anhydrase. Mostly, the solvent based data reported so far are collected from experiments conducted at diluted reagent conditions. Lower reactant concentration will result in a low carbon loading exit solution from CO_2 capture process (scrubber). Unfortunately, a low-carbon content rich solution/sorbent will require more energy input for reactant regeneration in the solution stripper. Generally speaking, the cost (capital and operational) for gaseous CO_2 separation processes is controlled by the combination of reaction kinetics, reaction enthalpy, and solvent carbon capacity in the rich solution. Low reaction rates will necessitate the need for larger absorption towers, which will result in higher capital costs. The solvent carbon capacity (sorbent type and reactant concentration) determines the majority of the energy input, e.g. sensible heat and steam evaporated for CO_2 stripping. The reaction enthalpy between a solvent and CO_2 will determine the heat released during the capture process and a larger portion of the heat input for carbon-component dissociation in the stripper.

We intended to explore some of the most effective ways to minimize CO_2 emission by developing a catalyst that could enhance the rate of CO_2 hydration. We

focused mainly on the synthesis and characterization of Cu, Co, and Zn with ligands, such as 1,5,7,7,12,14,14-hexamethyl-1,4,8,11-tetraazacyclotetradecane (teta, tetb)[108-109], 1,4,7,10-tetraazacyclododecane (cyclen)[110-112], tris(2-benzimidazoylmethyl)amine (NTB), nitrilotris(2-benzimidazoylmethyl-6-sulfonic acid) (NTBSA).[113] We found these complexes very interesting, affordable and conveniently prepared. We opted for the basic criteria of the catalyst, i.e., it should mimic the enzyme, be soluble in the solvent, be easy to synthesize and increase the rate of reaction at room temperature. We studied the CO_2 absorption at CAER in K_2CO_3 and MEA (monoethanolamine) solution at room temperature and the results were calculated by plotting the CO_2 loading (mol/kg) vs. flux ($mol \bullet cm^{-2} \bullet sec^{-1}$). Tests mentioned in this research were conducted in wetted-wall column (WWC) available at CAER. Wetted wall columns have been widely used in the investigation of mass transfer between gas and liquid, partially because the interfacial area can be measured accurately.[90, 114-115] With a known and uniform liquid contact area for gas diffusion the flux per unit area can be calculated.

Chapter 3 Development of Catalysts for CO_2 Capture

3.1 Introduction

Solvent-based post-combustion CO_2 capture is one of the preferred options for CO_2 removal from coal-fired combustion power plants. Post-combustion CO_2 capture has been used on an industrial scale for decades, and is being further developed for broader use due to the fact that it can be retrofitted to existing power plants with minimal modification, though the corresponding energy penalty is high. Most existing post-combustion CO_2 capture systems are related to chemical absorption/desorption using aqueous solvents such as alkanolamines, and have been practiced for gas cleanup applications since 1930.[81] In the process, CO_2 is absorbed at low temperature in the absorber, and is desorbed in the stripper at high temperature with solvent recycled to the absorption process.

A key issue of solvent-based capture systems is the heat requirement for solvent regeneration, which significantly reduces the net power output of the power plant.[84] Therefore, for economic reasons, the solutions for CO_2 absorption should have the advantages of (a) large capacity for CO_2; (b) capable of being regenerated using minimal energy; and (c) a high specific absorption rate.[85]

Potassium carbonate-bicarbonate solution is a common absorbent to capture CO_2 with high vapor pressure from natural gas or petroleum refinery process since it is moderately alkaline and undergoes slight change in pH during the absorption process,[87] has negligible volatility and degradation, and possesses the higher solubility of potassium bicarbonate. However, the major challenge of using a K_2CO_3−$KHCO_3$ solvent is the low absorption rate due to the slow CO_2 hydration step resulting in poor absorption performance. On another hand, considering these advantages, potassium carbonate-based solvents remain of interest for post-combustion CO_2 absorption.

We intended to explore some of the most effective ways to minimize CO_2 emission by developing a catalyst that could enhance the rate of CO_2 hydration. We focused mainly on the synthesis and characterization of Cu, Co, and Zn complexes with ligands, 1,5,7,7,12,14,14-hexamethyl-1,4,8,11-tetraazacyclotetradecane (teta, tetb)[108-109], 1,4,7,10-tetraazacyclododecane (cyclen)[110-112], tris(2-benzimidazoylmethyl)amine (NTB)[116-117], and nitrilotris(2-benzimidazoylmethyl-6-sulfonic acid) (NTBSA)[113]. There are various rationales behind choosing these complexes as these have many interesting CO_2 capture properties,[112,111,118,119] i.e., similar structural, thermodynamic and kinetic properties to carbonic anhydrase, stability towards heat, pH change and ionic strength as compared to carbonic anhydrase. We intended to test these molecules in a wetted-wall column experiment.

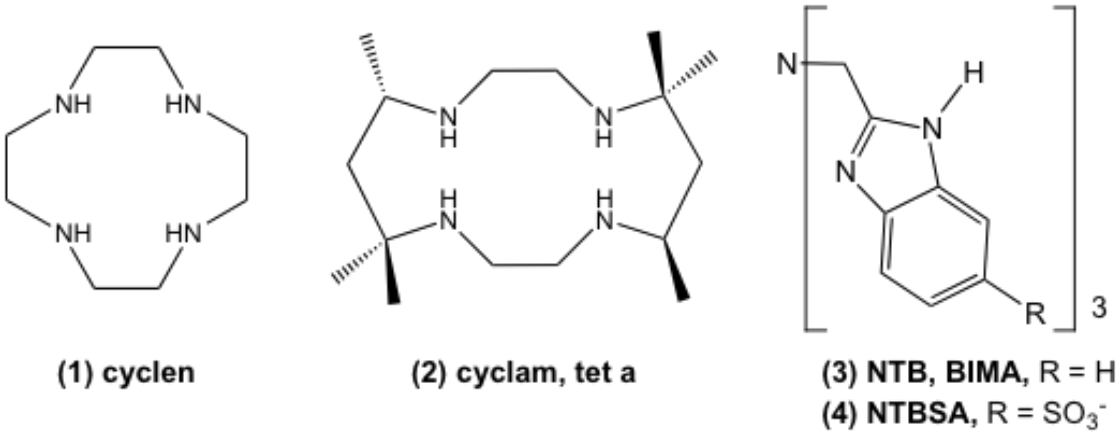

(1) cyclen **(2) cyclam, tet a** **(3) NTB, BIMA,** R = H
(4) NTBSA, R = SO_3^-

Figure 3.1 Ligands for CO_2 capture

Wetted-wall columns have been widely used for the determination of the fundamental gas–liquid absorption process (laminar film), partially because the interfacial area can be measured accurately.[90, 114-115] The essence of the WWC is a gas–liquid contactor in which CO_2 absorption by an aqueous solvent occurs on a known surface area. With a known and uniform liquid contact area for gas diffusion the flux per unit area can be calculated. This allows simplification of the second-order rate for CO_2 reaction to a pseudo first-order reaction by means of the surface renewal theory. In a wetted-wall column, the liquid flows in a film, under the influence of gravity, down a surface, usually a tube or rod. The contacting gas flows countercurrent to the liquid and mass transfer occurs over the gas-liquid contact area. The rigid tube or rod has a known surface area which is entirely coated by the thin film of solvent. The length of the rod can be adjustable to vary the contact time and thus vary the liquid film physical mass transfer coefficient. One major advantage of the wetted-wall column is its versatility. It can

operate over a wide range of conditions and can absorb or desorb CO_2 equally well. Among the concerns of the wetted-wall column are the entrance effects. It is important that the solvent is evenly dispersed so that a uniform film coats the entire surface of the rod. Any dry spots on the surface of the rod will not contribute to the flux and will lead to erroneous calculations. It is important to prevent the solution from rippling as it flows down the side of the contactor. The ripples enhance the liquid film physical mass transfer coefficient, and may affect the rate of absorption.

3.1.1 Setup of Wetted-Wall Column

A small wetted-wall column (WWC, Figure 3.2) built at the Center for Applied Energy Research (University of Kentucky) has been used for this research.[120] The system includes the main reactor of the WWC, the metering gas supply device, a water bath for gas saturation, a solvent reservoir, a pump, a CO_2 analyzer and a LabView control and data acquisition unit. The main reactor of the wetted-wall column, depicted in Figure 3.2, was used as the gas-liquid contactor throughout the experiments. The column is a stainless steel hollow rod measuring 15.3 cm in height and 1.26 cm in diameter with a well-defined surface area (60.56 cm^2). The WWC is enclosed in a reaction chamber, enclosed by a heating jacket to achieve and maintain the experimental temperature.

During the experiment, the chemical solution of interest is pumped from a reservoir through the inside of the tube, and flows down along the outer surface of the

tube to form a thin liquid film with a known surface area. The gas stream enters the WWC near the base of the column, counter-currently contacting the liquid film as it flows up into the gas outlet. The water bath, with circulation of the water inside, is used to control the temperature of the inlet gas, liquid and the reactor. The liquid is pumped back to a reservoir after collection at the base of the column. A Cole-Parmer peristaltic pump at 180 mL/min moves the solution from the reservoir through a preheater immersed in the heating bath. Preheater is a metal vessel with dip tube and packed with metal mesh. This cylinder serves two purposes, to pre-heat the gas before it enters the wetted-wall column and to moisten and saturate the gas before it enters the wetted-wall column. The saturation of the gas is important because if the gas is dry when it enters the reactor, it will pull the liquid film off the column, disrupting the flow and reaction. The saturated gas prevents this from happening and allows the gas and liquid to undergo the desired reaction. After heating, the solution flows into the WWC and later after contacting the gas stream, the solvent returns to the reservoir. The total pressure used in this work was 14 to 16 psi. The metered gases were mixed prior to entering the WWC. The gas flow rates were regulated using mass flow controllers and were calibrated by a soap bubble flow meter. After exiting the contactor, excess water was removed by passing the stream through a condenser. The acid traps eliminate any unwanted elements that might have entered the gas outlet line. Two tubes of crystalline silica gel pellets serve as a desiccant

for the gas stream, protecting the CO_2 analyzer from moisture damage. Absorption or desorption of CO_2 across the contacting area gives a CO_2 concentration difference in the gas stream between the inlet and outlet of the column. The Horiba VIA-510 NDIR CO_2 analyzer, which is an infrared CO_2 analyzer, was used to quantitatively measure the CO_2 concentration of the dry gas.

National Instruments NI LabVIEW 2010 (32-bit) with FieldPoint software (Version 6.0.5) is used to record the data and to simulate the gas flow inside the reactor and the inlet gas diffusion.

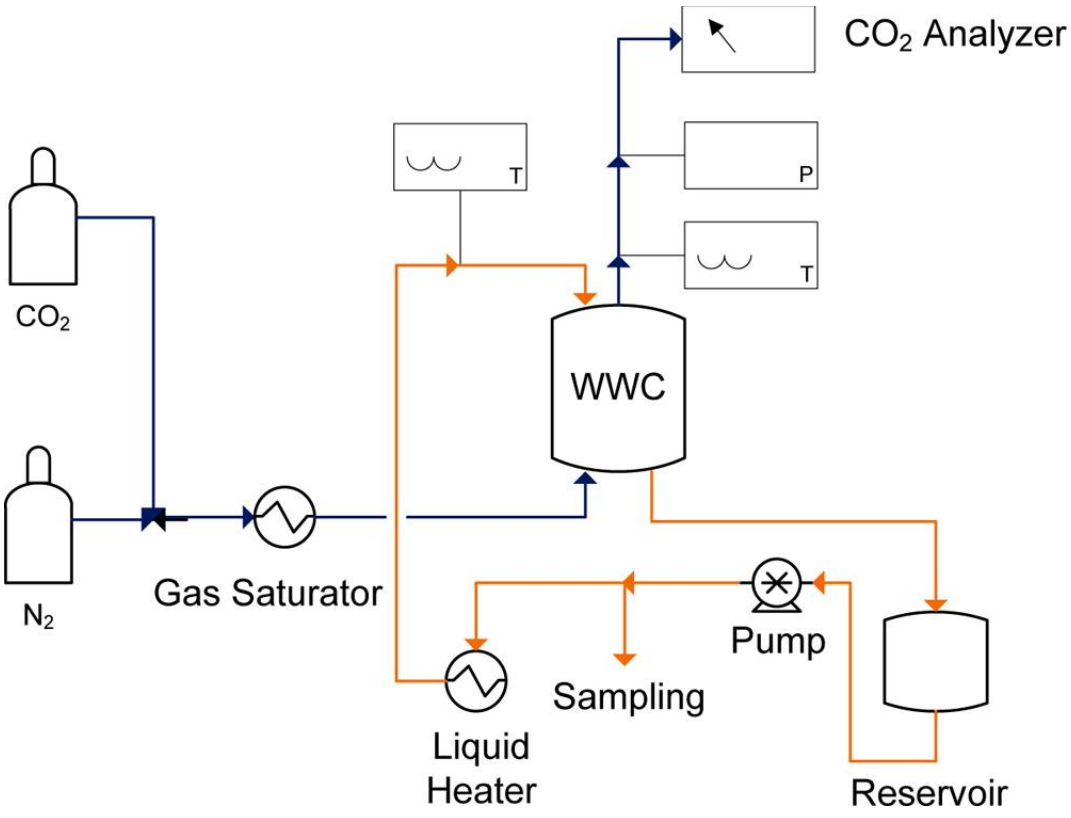

Figure 3.2 The experimental setup of the wetted-wall column (Reprinted with permission from Liu, K.; Jinka, K. M.; Remias, J. E.; Liu, K.; *Ind. Eng. Chem. Res.* **2013,** *52*, 15932). Copyright 2013 American Chemical Society.[120]

3.2 Experimental

3.2.1 Materials

All reactions were run under a nitrogen atmosphere with constant stirring. Ligands 1,4,8,10-tetraazacyclododecane (cyclen)[110], tris(2-benzimidazoylmethyl)amine (NTB)[121] and nitrilotris(2-benzimidazoylmethyl-6-sulfonic acid) NTBSA[113] were prepared by using known procedures. $CDCl_3$, acetone-d_6, DMSO-d_6 and D_2O (Cambridge Isotopes) and reagent-grade solvents (acetone, methanol, ethanol) were used as obtained commercially. Acetonitrile was dried and distilled over magnesium sulfate. Potassium carbonate (purity > 99%), 1,2-diaminoethane, hydrobromic acid, phenylenediamine, $Zn(BF_4)_2 \cdot 6H_2O$, $Cu(BF_4)_2 \bullet xH_2O$ and $Co(BF_4)_2 \bullet xH_2O$ were procured from Sigma Aldrich. Carbonic anhydrase NS81239 (batch PPE31476) with 38.0 g/L concentration was generously provided by Novozymes North America, Inc. Span gas (14% CO_2 in N_2), pure N_2 and pure CO_2 were supplied by Scott Gross. N,N-Dimethylformamide dimethyl acetal (ca. 97%), triethylenetetramine (technical 60%), nitrilotriacetic acid (Acros), boric acid (Fisher Scientific), $ZnCl_2$ and $NaBH_4$ (EMD), NH_4BF_4 (Alfa Ventron), NH_4PF_6 (Advanced Research Chemicals), $AgBF_4$ and $TlPF_6$ (Ozark Fluorine Specialists) and other reagents were obtained from the indicated commercial sources and used without purification. Melting points were recorded on either a Thomas-Hoover melting apparatus or Digi-Melt apparatus. TGA analyses were done on Thermal Analysis Hi-Res TGA

2950 instrument. In a typical run, 10–15 mg of the sample was loaded in a platinum pan. For all the analyses, a Hi-Res dynamic ramp 12.5 °C min^{-1}, Hi-Res 4.0, RT to 1000 °C was used under constant argon flow (65 mL/min). Infrared spectra of solid complexes were recorded in ATR mode between 4000 and 400 cm^{-1} on a Perkin-Elmer Paragon 1000 FT-IR spectrophotometer. ^{1}H and ^{13}C NMR spectra were recorded on a Varian Gemini 400 spectrometer at room temperature, unless mentioned otherwise, and were referenced to residual solvent peaks. Mass spectra were acquired by the University of Kentucky mass spectrometry facility. High-resolution electron impact (EI) ionization mass spectra were recorded at 25 eV on JEOL JMS-700T station and were referenced to perfluorokerosene (PFK). FAB-mass spectra were obtained on a Finnigan Polaris Q in EI mode via direct insertion probe. The mass spectrometer was operated in positive ion mode and mass spectra were calibrated by Alkali-CsI positive. X-ray diffraction data was collected on at 90K on either a Nonius Kappa CCD diffractometer or a Bruker-Nonius X8 Proteum diffractometer. Crystal indexing and data processing were performed either with DENZO-SMN (KappaCCD) or with Bruker APEX2 (X8 Proteum). The structures were solved and refined with SHELXS-97. Elemental analyses were performed at the Center for Applied Energy and Research at University of Kentucky.

3.2.2 Synthesis of ligands

3.2.2.1 Cyclen[110]

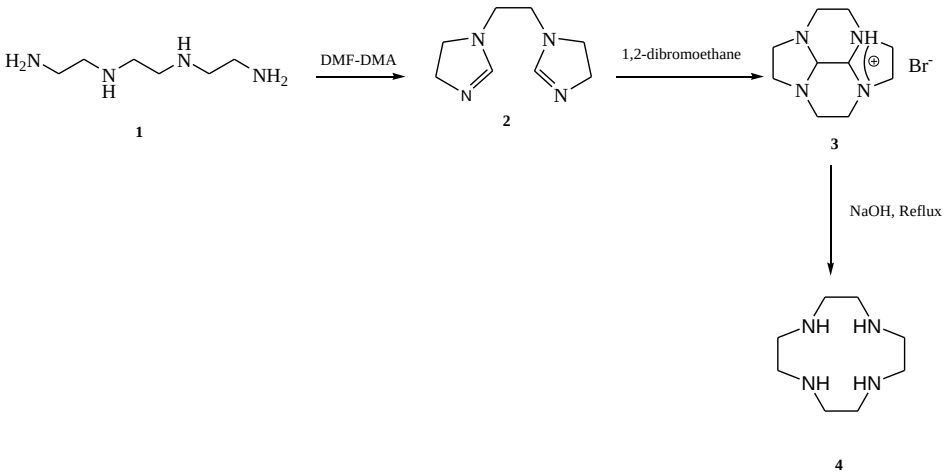

Linear teta (1). TETA (technical, 50.0 g, 0.30 mol) was added dropwise to a stirring solution of HCl (200 mL) and water (200 mL) over a period of fifteen minutes. This was then added all at once to HCl conc. (200 mL) and allowed to sit for two hours. A white precipitate of teta HCl formed. The solid was vacuum-filtered and washed twice with HCl conc. (2 × 50 mL) then dissolved in the minimal amount of water. While cooling and stirring, solid NaOH was added slowly until the pH reached approximately 10. The solution was then evaporated to remove the water and the remaining salt slurry was extracted with EtOH. The EtOH was then removed by rotary evaporation to yield a yellow oil salt, which was then distilled under a vacuum to give a clear oil **(1)**. 11.0 mL (37.0 %) was recovered.

1,1'-Ethylene-2-imidazoline (2). Linear teta **(1)** (10.0 mL, 0.07 mol) and DMF−DMA (18.0 mL, 0.14 mol) were added to a clean, dry round-bottom flask. The flask was purged

with N_2 and brought to reflux for thirty minutes, removed from heat and rotary-evaporated to give a thick, yellow oil, which crystallized upon standing **(2)**. 11.0 g were recovered for a yield of 97.0%.

2,3,4,5,6,7,8,8*c*-Octahydro-1*H*-4*a*,6*a*,8*a*-triaza-2*a*-azoniacyclopent[*fg*]-acenaphthylene bromide salt (3). Compound (**2)** (11.0 g, 0.07 mol), 1,2-dibromoethane (8.7 mL, 0.1 mol), anhydrous K_2CO_3 (7.70 g 0.06 mol) and acetonitrile (576 mL) were charged to a 1000 mL round-bottom flask and brought to reflux for three hours. The solution was removed from heat, filtered hot and rotary-evaporated to dryness to yield 17.0 g (86.0%) of brownish yellow crystals of (**3)**.

Cyclen (4). Compound (**3)** (17.0 g, 0.03 mol) was dissolved in 34 mL H_2O. This was added dropwise to a refluxing solution of NaOH (14.0 g, 0.24 mol) in 30 mL H_2O. The solution was allowed to reflux for thirty minutes. It was then filtered hot and rotary-evaporated. When the volume was sufficiently reduced, crystal formation began. Evaporation was stopped and the solution was allowed to cool. Crystals were then filtered and rotary evaporation of filtrate begun. When most of the water had been removed, a dark oil formed on top of the aqueous base. The mixture was allowed to cool and extracted with hot toluene to yield 4.0 g (38%) of (**4).** Spectroscopic and physical properties of the ligand matched the literature.

3.2.2.2 Tris(2-benzimidazoylmethyl)amine (NTB) [121]

Tripod, tris-(2-benzimidazoylmethyl)-amine and NTB complexes were synthesized from o-phenylenediamine and nitrilotriacetic acid by the method described by Thompson *et al*.[121]

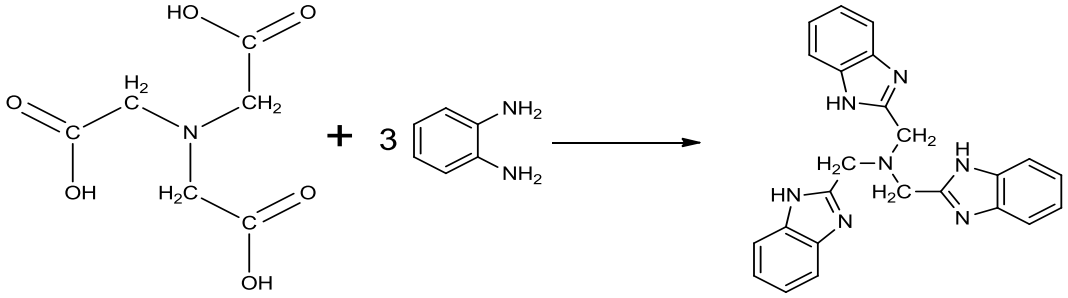

(4.59 g, 24.0 mmol) Nitrilotriacetic acid (8.10 g, 74.9 mmol) and o-phenylenediamine were finely ground with a mortar and pestle. Both were heated together at 190–200 °C for an hour in an oil bath. The mixture was then cooled and crushed once again with mortar and pestle and refluxed in methanol with decolorizing charcoal. The solution was filtered hot with gravity filtration. Volume of the solution was reduced until crystals formed, which were recrystallized from methanol. The product was vacuum filtered and dried under vacuum to get 4.69 g, 48% yield. Spectroscopic and physical properties of the ligand matched the literature.

3.2.2.3 Nitrilotris(2-benzimidazoylmethyl-6-sulfonic acid), NTBSA.[113]

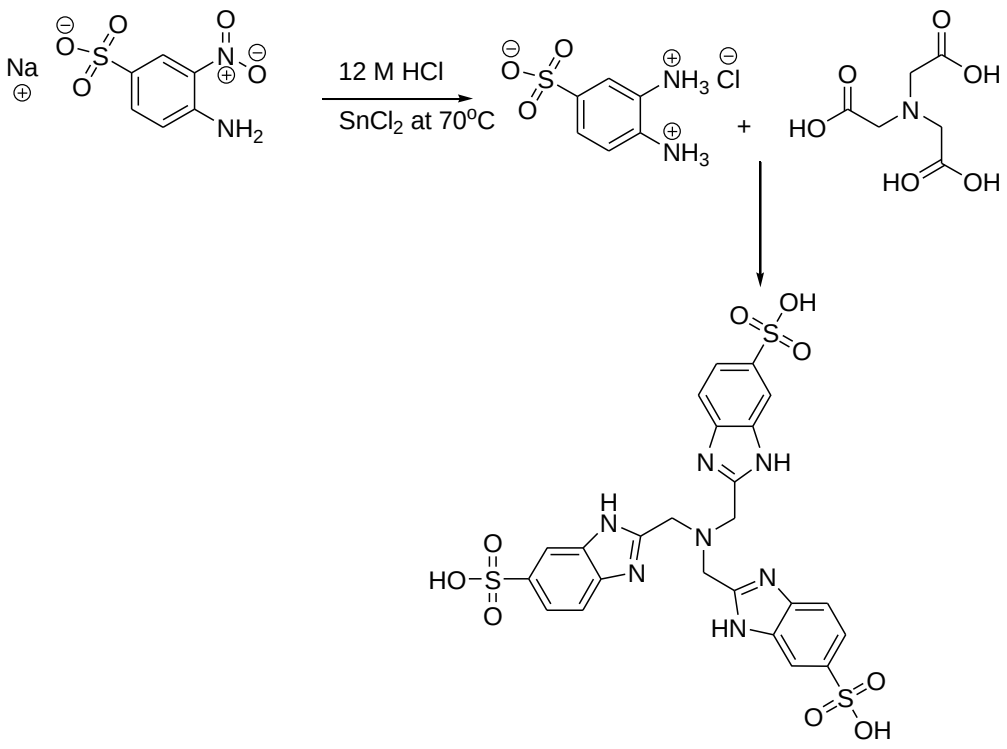

Tripod, (nitrilotris(2-benzimidazoylmethyl-6-sulfonic acid) NTBSA and NTBSA complexes were synthesized from o-phenylenediamine and nitrilotriacetic acid by the method described by Nakata *et al.*[113] Sodium 3-nitro-4-aminobenzenesulfonate (5.00 g, 20.8 mmol) was dissolved in 20 mL of 12 M HCl and reduced by $SnCl_2$ (14.1 g, 62.5 mmol) at 70 °C. The solution was concentrated for about 4 hours to form a white precipitate of 3,4-diaminobenzenesulfonate hydrochloride. 3,4-Diaminobenzenesulfonate hydrochloride (7.41 g, 33.2 mmol) and nitrilotriacetic acid (2.12 g, 11.1 mmol) were refluxed in 25 mL of 4.0 M HCl for 4 days. The formed blue precipitate with white

specks was dissolved in water by the addition of 25 mL NaOH solution. After the solution was decolorized by charcoal and acidified to less than pH 3 by *p*-toluenesulfonic acid, the white product was filtered and dried in vacuo to get 6.10 g of product (86.4% yield). Spectroscopic and physical properties of the ligand matched the literature.

3.2.3 Synthesis of complexes

3.2.3.1 Synthesis of [Cu(teta)][BF_4]$_2$ [122]

Teta (2.09 g, 7.01 mmol) was dissolved in 25 mL methanol and added to a warm solution of $Cu(BF_4)_2 \cdot xH_2O$ (1.68 g, 7.01 mmol) in 25 mL of methanol and refluxed at 60 °C under nitrogen for 1 h. The solution was allowed to cool to room temperature and stand for 30 min and then filtered. Magenta crystals were formed (1.22 g) and washed with methanol. The filtrate was kept overnight, filtered and was refluxed again at 60 °C under nitrogen for 1 h. After that the solution was allowed to stand at room temperature overnight. Deep blue crystals were filtered and washed with methanol. Both compounds were recrystallized from methanol and water (99:01), filtered, washed with ethyl ether and dried in *vacuo* to give solids. The theoretical yield for magenta and blue complexes were (1.12 g, 0.28 g ~38.3 % total yield based on limiting reagent) and IR (ATR, cm–1): 3237 (NH), 2976 (CH), broad peak ~1035 (BF_4). The magenta product was characterized by an X-ray diffraction study.

3.2.3.2 Synthesis of [{Cu(cyclen)(H_2O)}$_2$(μ-CO_3)][BF_4]$_2$ [122]

Cyclen (1.01 g, 5.80 mmol) dissolved in 30 mL methanol was added to warm solution of $Cu(BF_4)_2$•xH_2O (1.39 g, 5.81 mmol) in 30 mL of methanol and refluxed at 60 °C under nitrogen for 1 h. The solution was allowed to cool to room temperature and filtered. The volume was reduced to 25 % by evaporating the solution on a hot water bath. After the solution was allowed to stand at room temperature overnight, the deep blue precipitate formed was filtered and washed with methanol. The second crop of the material was obtained by evaporating the filtrate on a rotary evaporator at 55 °C. The compound was recrystallized from methanol and water (99:01), filtered washed with ethyl ether and dried *in vacuo* to give a deep blue solid (2.14 g, 49.8 % based on limiting reagent). IR (ATR, cm–1): 3628 (OH), 3359 (NH), 3296 (NH) multiple peaks between ~1410–1490 (CO_3) and ~1030 (BF_4). Elemental analysis data: (Anal. Calcd for $C_{17}H_{42}N_8O_4B_2F_8Cu_2$: % C 27.55, % H 5.98, % N 15.11. Found: % C 28.16, % H 6.02, % N 15.60).

3.2.3.3 Synthesis of [Co(cyclen)(OH)(H_2O][BF_4]$_2$•(CH_3OH) [122]

Cyclen (1.01 g, 5.80 mmol) dissolved in 30 mL methanol was added to $Co(BF_4)_2$•xH_2O (1.39 g, 5.81 mmol) in 30 mL of methanol and refluxed at 60 °C under nitrogen for 1 h. The solution was allowed to cool to room temperature and was then filtered. The volume was reduced to 25 % by evaporating the solution on a hot water bath. After the solution was allowed to stand at room temperature, the mixture was kept overnight and the dark

brown precipitate was filtered and washed with methanol. The second crop of the material was obtained by evaporating the filtrate on a rotary evaporator at 55 °C. The compound was titrated with pentane and recrystallized from methanol, filtered, washed with ethyl ether and dried in *vacuo* to give a dark brown solid (1.84 g, 67.2 % based on limiting reagent). IR (ATR, cm–1): 3571(OH), 3305 (NH), 3230 (NH), ~1000(BF). Elemental analysis data: Anal. calcd. for $C_9H_{27}N_4O_3B_2F_8Co$: % C 22.9, % H 5.8, % N 11.9 Found: % C 23.1, % H 5.1, % N 11.8.

3.2.3.4 Synthesis of $[Zn(cyclen)(H_2O)][SiF_6]•2H_2O$

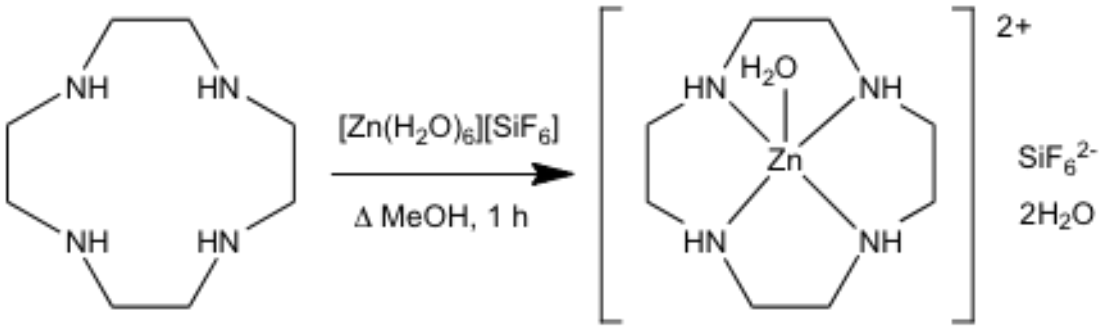

Cyclen (1.00 g, 5.80 mmol) dissolved in 30 mL methanol was added to $[Zn(H_2O)_6]SiF_6$ (1.39 g, 5.81 mmol) in 30 mL of methanol and refluxed at 60 °C under nitrogen for 1 h. The solution was allowed to cool to room temperature and filtered to obtain 2.38 g (95.0 % yield) of the catalyst. IR (ATR, cm^{-1}): 3342 (NH), 3247 (NH), 688 (SiF_6^{2-}). Crystal structure determination was done via X-ray crystallography.

3.2.3.5 Synthesis of $[Zn(NTB)(H_2O)][BF_4]_2$

NTB (1.51 g, 3.70 mmol) and $Zn(BF_4)_2 \cdot 6H_2O$ (1.30 g, 3.75 mmol) were separately dissolved in ethanol. The metal tetrafluoroborate solution was added dropwise with stirring to the NTB solution. The mixed solution was then stirred for an hour at 80 °C with a condenser. Volume was reduced for the product to crystallize, then vacuum filtered and dried under vacuum to get 2.31 g, 87.1% yield. Compound was characterized with X-ray crystallography.

3.2.3.6 Synthesis of $[Cu(NTB)(H_2O)](BF_4)_2$

NTB (2.00 g, 4.91 mmol) and $Cu(BF_4)_2 \cdot 6H_2O$ (1.25 g, 4.91 mmol) were separately dissolved in ethanol. The metal tetrafluoroborate solution was added dropwise with stirring to the NTB solution. The solution was stirred for an hour at 80 °C with a condenser. Volume was reduced for the product to crystallize, then vacuum filtered and dried under vacuum to get 1.0 g, 31% yield. Compound was characterized with X-ray crystallography.

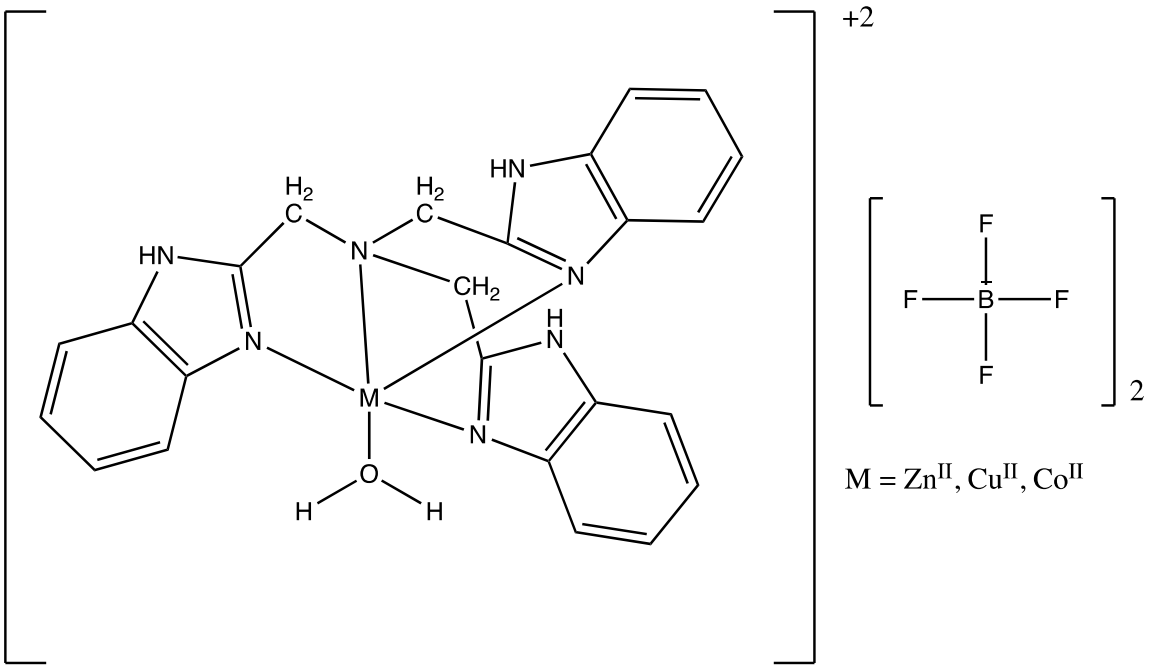

3.2.4 Setup for fast catalyst screening

The reactions were carried out in a 4-necked 250 mL round-bottom flask equipped with a pH meter. A 14 vol% CO_2 gas with balanced N_2, was supplied through an MFC (Aalborg) at 1.0 L/min. The temperature was monitored throughout the reaction with experiments conducted at room temperature. The progress of the experiment was monitored for the change in pH with time as CO_2 was absorbed.

3.2.5 Setup for catalysts and enzyme testing in wetted-wall column

Experiments were conducted with 500 mL of solution, which was run continuously over the wetted-wall (to and from the same reservoir). A liquid sample was taken when the CO_2 analyzer reading stabilized and the mass transfer rate and solution composition were determined based on this sample. The solution was then carbon-loaded by sparging the solution reservoir with 40% CO_2 (balance N_2) for 5 minutes with stirring before passing

the solution again to the WWC for a mass transfer measurement. The purpose of carbon loading is to speed up the entire process by helping the solution reach its carbon saturation point (carbon capacity) quicker, which would result in the conclusion of the experiment. Every time carbon loading is performed on the solvent, the carbon level increases as the solvent absorbs carbon dioxide. Faster rates come from higher CO_2 concentration and so 100% is ideal, but some solvents may not allow this (i.e. ammonia solution will have a gas-phase reaction with high CO_2 levels forming solid ammonium bicarbonate in the reaction chamber.) At the same time, there is an exothermic reaction that takes places between the carbon dioxide and the solvent, which results in the temperature of the solvent increasing substantially in the beginning but less and less as the solvent approaches its saturation point. For all tests, a 1.9 M concentration of K_2CO_3 was used. The enzyme and catalysts were tested at 50 °C and 1.51 SLPM of total inlet gas flow was nominally set at 18% CO_2.

3.3 Results and Discussion

$[Zn(cyclen)][ClO_4]_2$ is a promising CO_2 hydration catalyst.[118-119, 123] Zhang *et al.*[118] showed that the catalytic activity of $[Zn(cyclen)(OH)]^+$ with perchlorate counteranion is the highest of all of their studied model complexes. A number of other simple zinc complexes like 1,5,9-triazacyclododecane-([12]aneN_3) prepared by Kimura *et al.*[124], modeled on carbonic anhydrase, have been shown to activate the bound ligand water

molecule for nucleophilic attack towards CO_2. Based on this result, our group's first targets were the Cu, Co and Zn cyclen mono- or di-aqua complexes with counteranions, including PF_6^-, BF_4^-, Cl^-, CH_3COO^-, NO_3^-, $CF_3SO_3^-$. The initial aim in doing this was to synthesize complexes that did not possess the potentially explosive perchlorate counteranion. Perchlorate is also toxic to the environment. It is generally not expected that the counteranion participates in the reaction mechanism, and so the change was anticipated as a simple process. However, it was found that substitution of other non-coordinating counteranions for perchlorate was not trivial. Substitution of other weakly or non-coordinating counteranions including PF_6^-, Cl^-, CH_3COO^-, NO_3^- and $CF_3SO_3^-$ showed strong coordination to the Zn center. For example, the use of zinc acetate dihydrate to provide the zinc ion gives $[Zn(teta)(CH_3COO)][PF_6]$, which was characterized by single-crystal X-ray diffraction.[122] Zinc nitrate hexahydrate gives similarly characterized $[Zn(teta)(NO_3)][PF_6]$.[122] The acetate and nitrate ions both bind to the zinc ion in a dihapto (κ^2O,O) mode. Tetrafluoroborate ligand was found to have further reactions in aqueous-based solvents.

The reaction of $[Zn(H_2O)_6][BF_4]_2$ with cyclen gives $[\{Zn(cyclen)\}_3(\mu_3\text{-}CO_3)][BF_4]_4 \bullet H_2O$, which was characterized by single-crystal X-ray diffraction.[122] It contains three roughly square pyramidal zinc centers bound to cyclen in the basal positions and bicarbonate in the apical site, forming a trimeric μ_3-carbonato complex. The

carbonate complex appears to be a dead end in carbon dioxide hydration. Finally, $[Zn(H_2O)_6][SiF_6]$ reacts with cyclen to give $[Zn(cyclen)(H_2O)][SiF_6]\bullet 2H_2O$ which has the desired H_2O bound to Zinc. A coordinated water that ionizes to a coordinated hydroxide around neutral pH could be the key to rapid CO_2 fixation. According to Vahrenkamp,[117] the pK_a of unbound water is around 14 but in presence of the zinc ion surrounded by ligands, the pK_a of the bound water decreases to around 7-8 pK_a units in CA (similarly in mimetic zinc complexes) making OH^- available to react with CO_2 at near neutral pH. According to Kimura[125], since the ligated water in CA has pK_a around 6.8 the predominant form of CA above pH 6.8 will be $L_3Zn\text{-}OH^-$. This OH^- form catalyzes the hydration of CO_2 to HCO_3^- ion, while below pH 6.8 $L_3Zn\text{-}OH_2$ is the predominant form, which catalyzes the reverse reaction, dehydration of HCO_3^-. Zn^{II} has a high affinity for HCO_3^- as a monodentate ligand. Koike and Kimura[125-126] postulated that if the zinc were more acidic, the HCO_3^- may become deprotonated to CO_3^{2-} and act as a bidentate ligand.

A crystal structure of $[Zn(cyclen)(H_2O)][SiF_6]\bullet 2H_2O$ complex (Figure 3.3) shows that hexafluorosilicate neither fragments under the reaction conditions nor coordinates to the zinc(II) ion. $[Zn(cyclen)(H_2O)][SiF_6]\bullet 2H_2O$ prepared at CAER was sent to LLNL for stopped-flow kinetics comparison of its activity with $[Zn(cyclen)(H_2O)][ClO_4]_2$ synthesized at LLNL. The catalyst was dissolved in 0.1 M AMPSO buffer, 0.2 M $NaClO_4$, 10^{-5} M thymol blue pH indicator, and pH 9.0, at 25 ºC**.** The above solution was

rapidly mixed 1:1 with a CO_2-saturated water solution ([CO_2] = 0.034 M) and the change of pH was monitored versus time. The rate constant found for the SiF_6^{2-} salt was 2100 ± 100 $M^{-1}s^{-1}$, and for the perchlorate salt from LLNL salt was 2300 ± 200 $M^{-1}s^{-1}$. These rates compare favorably to the literature values (2200 $M^{-1}s^{-1}$ for pH 8.8, 2600 $M^{-1}s^{-1}$ for pH 9.1).[118]

A series of metal(II) tetrafluoroborate salts was reacted with a tripodal ligand, tris(2-benzimidazoylmethyl)amine (NTB), by Dunbar High School student, Christopher Sato, to form metal complexes [M(NTB)(H_2O)][BF_4]$_2$ that are able to catalyze the hydration of CO_2. The reaction of NTB with Zn^{II} and Cu^{II} hydrated tetrafluoroborate salts in ethanol gave new Zn-NTB Cu-NTB complexes. Zn-NTB structure does not allow the water to bind to the zinc. The structure of Cu-NTB complex was found to be same as previously reported by a coworker when methanol was used as solvent.[122] However, these metal complexes do not dissolve well in water or a weak base. This makes it difficult to test in the wetted-wall column experiment for the rate of absorption of carbon dioxide. Therefore, a sulfonate derivative ligand, nitrilotris(2-benzimidazolylmethyl-6-sulfonic acid) (NTBSA)[127], is reacted with the same metal tetrafluoroborate hydrates to produce a soluble complex, Na[M(NTBSA)(H_2O)]. Both Zn and Cu NTBSA metal complexes are soluble in water and weak base. According to Davy *et al.*[119] Zn^{II} complex with NTBSA, was able to catalyze the capture of CO_2 at a rate extrapolated almost to an order of

magnitude of that of CA. Both ligands, NTB and NTBSA have three benzimidazole branches stemming out from a nitrogen atom to form a trigonal pyramidal shape. However, after their reaction with the metal tetrafluoroborate, the product becomes trigonal bipyramidal. The trigonal bipyramid creates a guarded pocket in the center of the molecule underneath the metal atom for CO_2 binding. This coordination is important to mimic the CA active site. A coordinated water that ionizes to a coordinated hydroxide around neutral pH could be the key to rapid CO_2 fixation. A hydrophobic pocket that can hold CO_2 may activate the substrate toward hydration. The optimum distance should be about 3.2 Å from the zinc center.[118]

In the crystallography of NTB catalysts, it was found that SiF_6^{2-} is formed during the reaction using the metal tetrafluoroborates. Reaction of $[Zn(H_2O)_6][BF_4]_2$ and $[Cu(H_2O)_6][BF_4]_2$ with tris(2-benzimidazoylmethyl)amine (NTB) resulted in $[Zn_2(\mu\text{-}F)(NTB)_2][SiF_6][BF_4]$ and $[Cu(NTB)(H_2O)]_2[BF_4]_2[SiF_6]\bullet(CH_3OH)_3\bullet(H_2O)_{11}$, containing fluoride and SiF_6^{2-} derived from BF_4^-. Evidently, tetrafluoroborate is attacked by the electrophilic center and the glass reaction vessel, suggesting that BF_4^- could compromise the stability of a catalyst. It is recommended to do the synthesis of $[M(NTB)(H_2O)][BF_4]_2$ and $Na[M(NTBSA)(H_2O)]$ in a plastic container.

The X-ray crystal structure of the Zn NTB complex (Figure 3.4) shows a fluoride bridge between two zinc centers, resulting in a Zn–F–Zn moiety with a Zn–F distance of

1.9692(7) Å. A crystallographic inversion center at the fluorine atom resulted in a 180.00(4)° Zn–F–Zn bond angle. On the other hand, the Cu NTB catalyst formed the proposed structure, but still had the SiF_6^{2-} form with it (Figure 3.5). The single-crystal X-ray structure (Figure 5) shows that the compound is pseudo trigonal pyramidal at Cu with a bond angle of 106.34(6)° for N(5)-Cu(1)-N(7), 117.21(6)° for N(3)-Cu(1)-N(7) and 129.58(6)° for N(5)-Cu(1)-N(3) with the bond distances of 2.0050(16) Å for Cu1-N5, 2.0122(16) Å for Cu1-N3 and 2.0904(15) Å for Cu1-N7 and the axial position is occupied by the water molecule with a bond distance of 1.9484(14) Å for Cu1-O1.

We were not able to crystallize NTBSA complexes for crystallography. It has been difficult to crystallize them due to the sodium cation. Attempts were made to react the complexes with tetramethylammonium chloride dissolved in methanol to get rid of the sodium cation for easier crystallization.

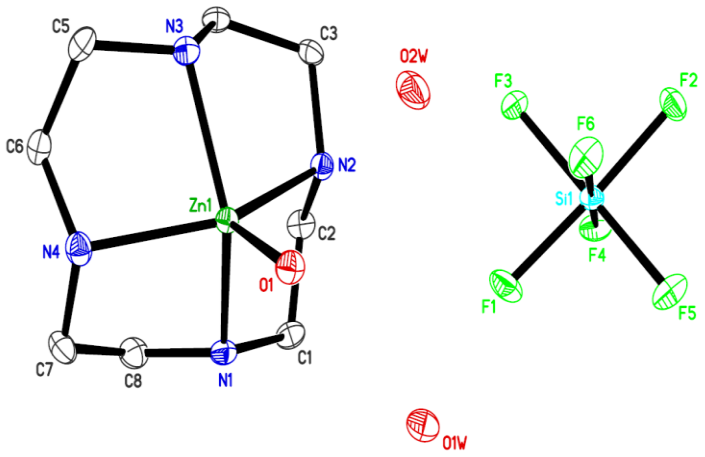

Figure 3.3 Thermal ellipsoid plot of the X-ray crystal structure of $[Zn(cyclen)(H_2O)][SiF_6]•2H_2O$

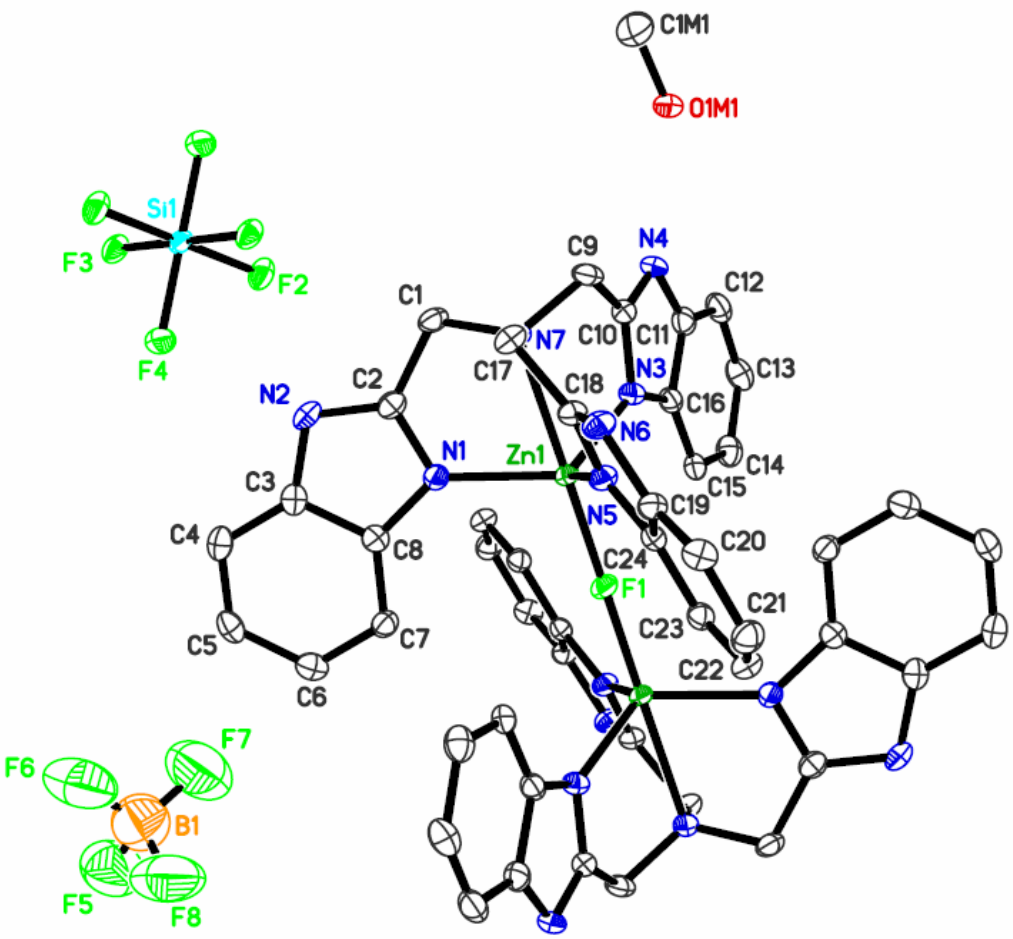

Figure 3.4 Thermal ellipsoid plot of the X-ray crystal structure of $[Zn_2(\mu\text{-}F)(NTB)_2][SiF_6][BF_4]$

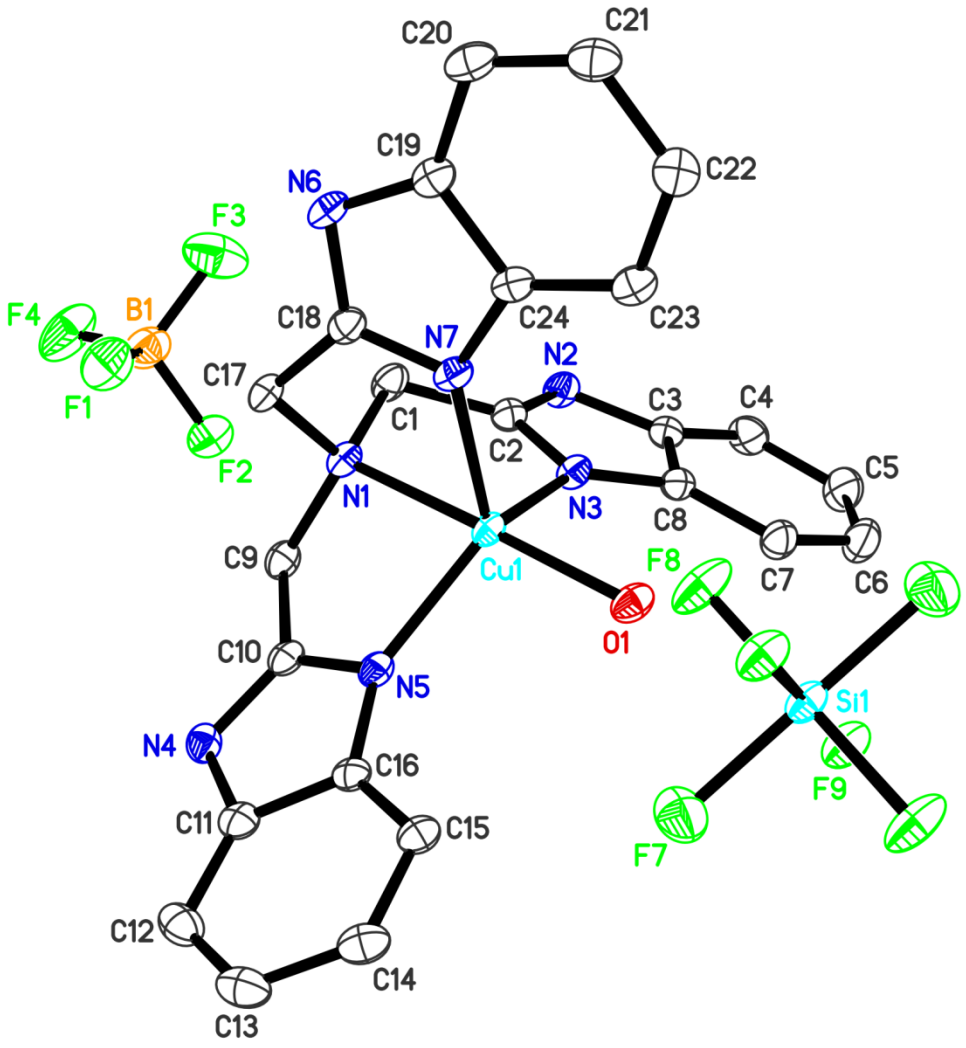

Figure 3.5 Thermal ellipsoid plot of the X-ray crystal structure of $[Cu(NTB)(H_2O)]_2[SiF_6][BF_4]_2\,(H_2O)_{9.29}(CH_3OH)_{3.35}$ [122]

3.3.1 Catalytic Activity

Based on the carbonic anhydrase (CA) experiments conducted in the wetted-wall column as shown in Figure 3.6 (carbonic anhydrase in 1.9 M K_2CO_3 in wetted-wall column), baseline threshold was established. Using the 95% confidence interval, catalyst

concentration needed in the wetted-wall column to see the change in the flux can be found out. Based on CA k_{cat} and CA concentration used, method was demonstrated effective using CA. Though, with the concentrations for mimics here and the rate constants reported, we should have been able to see a difference in the flux with catalysts.

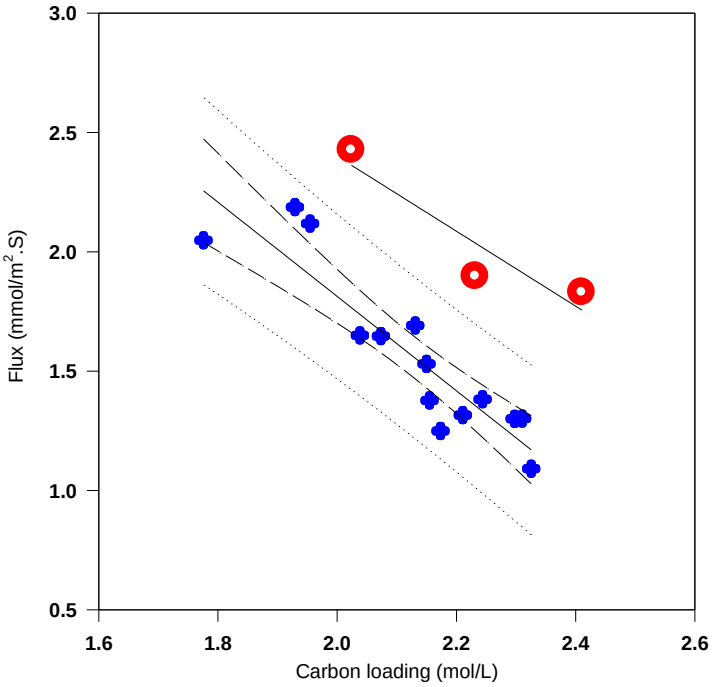

Figure 3.6 Establishment of baseline in 1.9 M aqueous K_2CO_3 in wetted-wall column and demonstration of observed catalytic enhancement using carbonic anhydrase. Blue = control (no carbonic anhydrase); red = 2×10^{-3} mM carbonic anhydrase.

Figure 3.7 (wetted-wall column measurements in 1.9 M aqueous K_2CO_3) shows the results of the experiment. Before testing catalysts, it was first necessary to establish the baseline experiment for the solvent alone and also to show good reproducibility. For all tests, a 1.9 M concentration of K_2CO_3 was used. The catalysts were tested at 50 °C

and 1.51 SLPM of total gas flow inlet flow was nominally set at 18% CO_2. $[Cu(teta)][BF_4]_2$, $[\{Cu(cyclen)(H_2O)\}_2(\mu\text{-}CO_3)][BF_4]_2$, $[Co(cyclen)(OH)(H_2O][BF_4]_2 \bullet (CH_3OH)$ and $[Zn(cyclen)(H_2O)][SiF_6] \bullet 2H_2O$ catalysts were tested. In following figure, they are identified as $[Cu(teta)][BF_4]_2$, $[Cu(cyclen)][BF_4]_2$, $[Co(cyclen)][BF_4]_2$ and $[Zn(cyclen)][SiF_6]$ respectively. From figure 3.7, it is seen that out of the various catalysts tested, none of them show significant absorption.

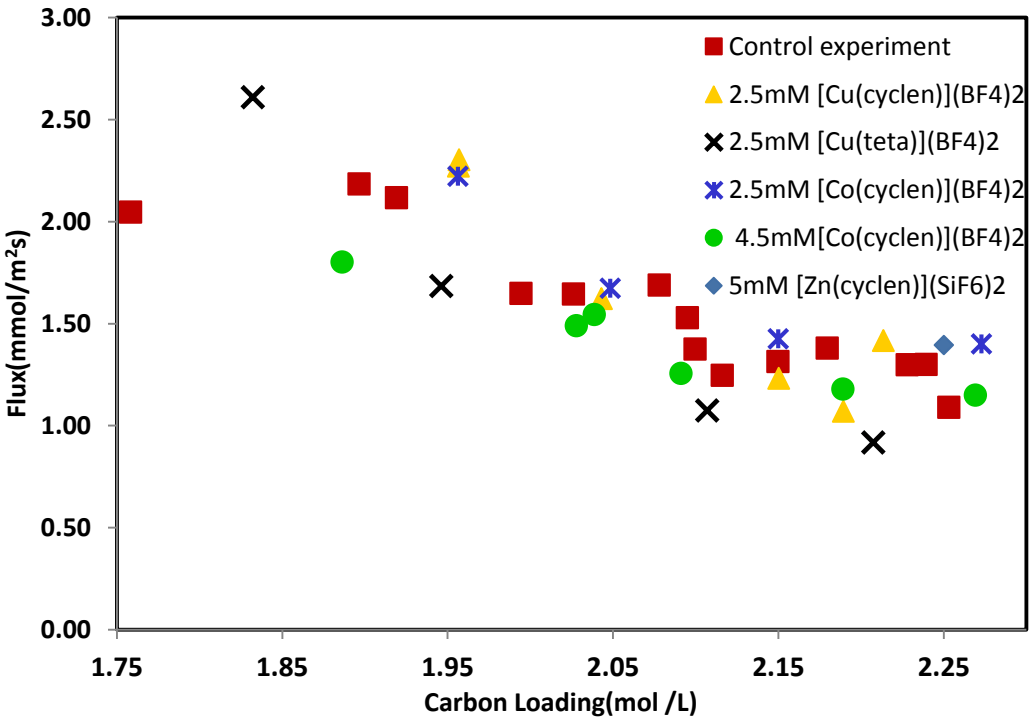

Figure 3.7 Wetted-wall column measurements in 1.9 M aqueous K_2CO_3.

Furthermore, to improve the efficiency and decrease the amount of catalyst needed, a smaller-scale screening test was developed for CO_2 capture. Figure 3.8 shows the pH drop method. Using a decrease in pH over time method a series of catalysts was

tested. Compared to the WWC method, 5 times lower catalyst and only a few hours of evaluation time are required. This, further saves time since the smaller amount of catalyst needed reduces time spent synthesizing complexes.

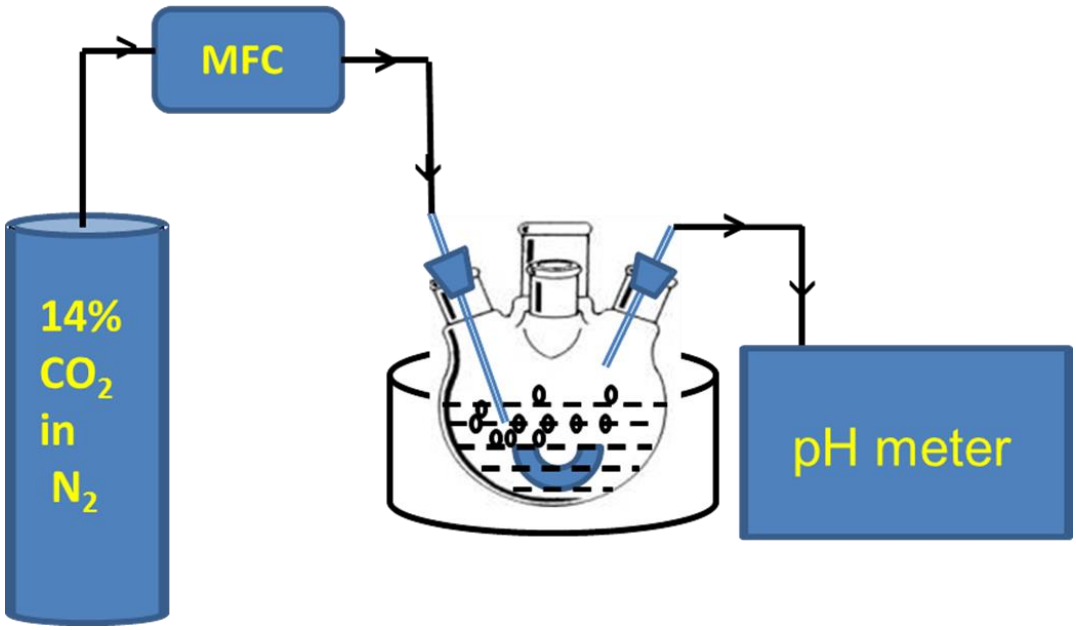

Figure 3.8 pH drop experiment setup

Figure 3.9 highlights the results obtained using the pH drop evaluation method. The complexes tested include $[Cu(teta)][BF_4]_2$, $[\{Cu(cyclen)(H_2O)\}_2(\mu\text{-}CO_3)][BF_4]_2$ $[Co(cyclen)(OH)(H_2O][BF_4]_2 \bullet (CH_3OH)$, $[Zn(cyclen)(H_2O)][SiF_6] \bullet 2H_2O$, $Na[Zn(NTBSA)(H_2O)]$ and $Na[Cu(NTBSA)(H_2O)]$. In (Figure 3.9), they are identified as Cu(teta), Cu(cyclen), Co(cyclen), Zn(cyclen), Zn(NTBSA) and Cu(NTBSA) respectively. However, regardless of species or testing method, as discussed above, the enhancement in the measured rate is insignificant here. Note that for carbonic anhydrase (at the same concentration) to show minimum activity increase in the WWC was also tested and so

establishes a threshold value for testing using pH drop. Based on these results, the crystal structures obtained and discussion with LLNL as part of project collaboration, it is believed that the lack of activity in the tested solvent, at least for the Zn(cyclen) complex, is related to a strong interaction of the solvent with catalyst.

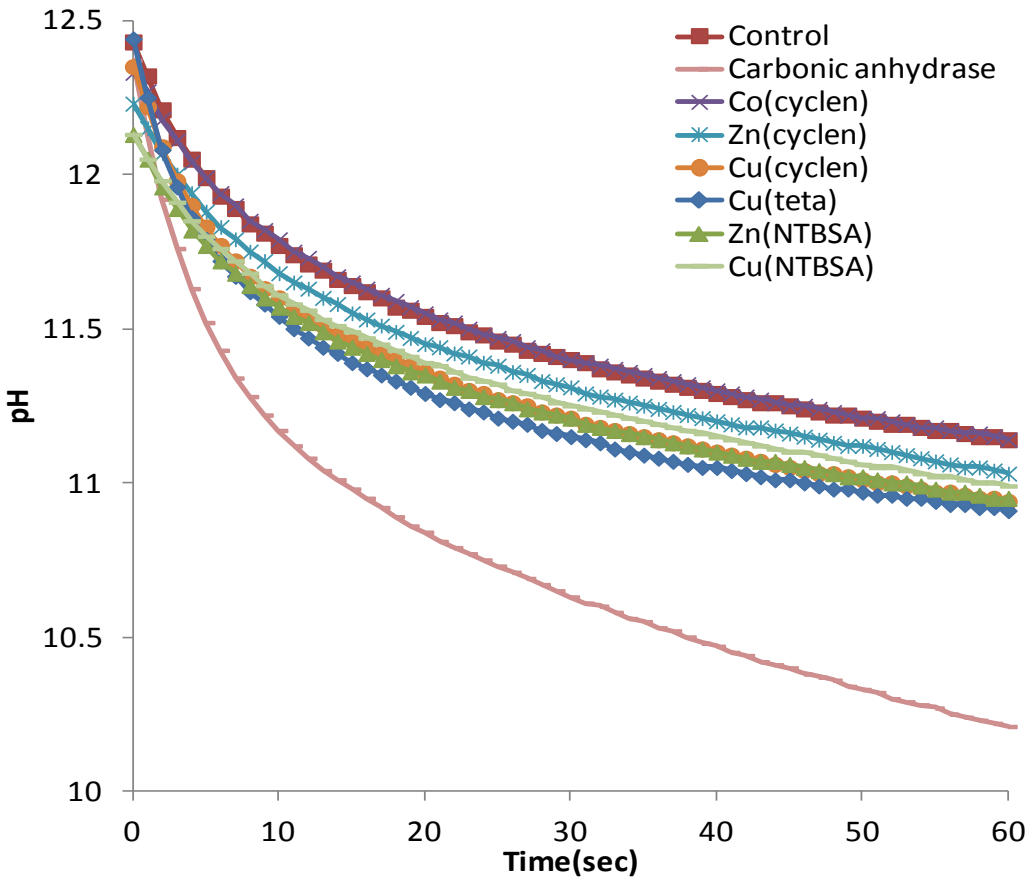

Figure 3.9 Results for catalyst screening experiment using pH drop over time method in 1.9 M K_2CO_3.

3.4 Conclusions

Our group's first targets were the Cu, Co and Zn cyclen mono- or di-aqua complexes with environmentally safe counteranions instead of perchlorates. However, it was found that substitution of other non-coordinating counteranions for perchlorate was

not trivial. Substitution of other weakly or non-coordinating counteranions including PF_6^-, Cl^-, CH_3COO^-, NO_3^- and $CF_3SO_3^-$ showed strong coordination to the Zn center. None of the compounds were found to be catalytically active in the conditions conducive to post carbon capture when tested in a wetted-wall experiment. It was proposed that the lack of activity may be related to coordination of the solvent to the metal. A new laboratory setup was designed to reduce the screening time of catalysts for CO_2 capture. Using a decrease in pH over time method a series of catalysts was tested. Compared to the WWC method, lower catalyst quantity and only a few hours of evaluation time are required. This further save time since the smaller amount of catalyst needed reduces time spent synthesizing complexes.

Table 3.1 Crystal data and structure refinement for $[Cu(NTB)(H_2O)]_2[SiF_6][BF_4]_2(H_2O)_{9.29}(CH_3OH)_{3.35}$

Formula	$C_{51.35}H_{78}B_2Cu_2F_{14}N_{14}O_{14.83}Si$
Formula wt (amu)	1571.59
T,K	90.0(2)
Crystal system,	Triclinic
Space group	*P* –1
Z	1
a, Å	10.8160(2)
b, Å	13.7558(3)
c, Å	14.0715(5)
α,(deg)	118.516(1)
β, (deg)	101.512(1)
γ, (deg)	101.053(1)
V, A^3	1699.51(8)
d_{calc}, Mg/m^3	1.536
Crystal size(mm^3)	0.12 x 0.11 x 0.02
F(000)	811
Radiation	CuK_a (λ= 1.54178 Å)
Monochromator	Graded Multilayer Optics
Absorption coef(mm^{-1})	1.916
Diffractometer	Bruker X8 Proteum
Range (deg)	3.70 to 68.29
Limiting indices	$-13 \le h \le 13$
	$-16 \le k \le 16$
	$-16 \le l \le 16$
Reflections collected	23902
Independent Reflections	6114 [R(int) = 0.0368]
Absorption correction	Semi-empirical from equivalents
Refinement method	SHELXL-97
Refinement method	Full-matrix least-squares on F^2
Max. and min. transmission	0.963 and 0.774
Data / restraints / parameters	6114 / 48 / 511
Goodness-of-fit on F^2	1.046
Final R indices [I>2 σ (I)]	R1 = 0.0346, wR2 = 0.0905

R indices (all data)	R1 = 0.0370, wR2 = 0.0927
Largest diff. peak and hole	0.525 and –0.400 e.A^{-3}

Table 3.2 Bond Angle and Bond Distances for $[Cu(NTB)(H_2O)]_2[SiF_6][BF_4]_2(H_2O)_{9.29}(CH_3OH)_{3.3}$

Atoms	Distance (Å)
Cu(1)-O(1)	1.9484(14)
Cu(1)-N(5)	2.0050(16)
Cu(1)-N(3)	2.0122(16)
Cu(1)-N(7)	2.0904(15)
Cu(1)-N(1)	2.1154(15)
O(1)-H(1O)	0.793(18)
O(1)-H(2O)	0.791(18)
N(1)-C(1)	1.488(2)
N(1)-C(9)	1.489(2)
N(1)-C(17)	1.491(2)
N(2)-C(2)	1.343(2)
N(2)-C(3)	1.382(3)
N(3)-C(2)	1.316(2)
N(3)-C(8)	1.393(2)
N(4)-C(10)	1.339(2)
N(4)-C(11)	1.383(3)
N(5)-C(10)	1.322(2)
N(5)-C(16)	1.388(2)
N(6)-C(18)	1.348(2)
N(6)-C(19)	1.387(3)
N(7)-C(18)	1.317(2)
N(7)-C(24)	1.391(2)
C(1)-C(2)	1.491(3)
C(3)-C(4)	1.391(3)
C(3)-C(8)	1.399(3)
C(4)-C(5)	1.378(3)
C(5)-C(6)	1.405(3)
C(6)-C(7)	1.380(3)
C(7)-C(8)	1.390(3)
C(9)-C(10)	1.488(3)
C(11)-C(12)	1.392(3)
C(11)-C(16)	1.403(3)
C(12)-C(13)	1.381(3)
C(13)-C(14)	1.402(3)
C(14)-C(15)	1.382(3)
C(15)-C(16)	1.397(3)
C(17)-C(18)	1.493(3)
C(19)-C(20)	1.392(3)
C(19)-C(24)	1.405(3)
C(20)-C(21)	1.378(3)
C(21)-C(22)	1.407(3)
C(22)-C(23)	1.380(3)
C(23)-C(24)	1.392(3)
B(1)-F(4)	1.370(3)
B(1)-F(1)	1.378(3)
B(1)-F(2)	1.401(3)
B(1)-F(3)	1.419(3)
Si(1)-F(8)	1.6775(11)
Si(1)-F(8)#1	1.6776(11)
Si(1)-F(7)#1	1.6790(12)
Si(1)-F(7)	1.6790(12)
Si(1)-F(9)#1	1.6929(10)
Si(1)-F(9)	1.6929(10)
O(2W)-H(1W2)	0.785(18)
O(2W)-H(2W2)	0.793(18)
O(3W)-H(1W3)	0.789(19)
O(3W)-H(2W3)	0.817(18)
O(4W)-H(1W4)	0.812(19)
O(4W)-H(2W4)	0.794(19)
O(5W)-H(1W5)	0.820(19)
O(5W)-H(2W5)	0.82(2)
O(1M)-C(1M)	1.398(4)
O(2M)-C(2M)	1.43(2)
O(2M)-H(1W6)	0.96(7)
O(2M)-H(2W6)	1.04(7)

O(6W)-H(1W6)	0.82(2)
O(6W)-H(2W6)	0.81(2)

Atoms	Angle (°)
O(1)-Cu(1)-N(5)	98.20(6)
O(1)-Cu(1)-N(3)	95.00(6)
N(5)-Cu(1)-N(3)	129.58(6)
O(1)-Cu(1)-N(7)	103.51(6)
N(5)-Cu(1)-N(7)	117.21(6)
N(3)-Cu(1)-N(7)	106.34(6)
O(1)-Cu(1)-N(1)	175.71(6)
N(5)-Cu(1)-N(1)	81.39(6)
N(3)-Cu(1)-N(1)	82.09(6)
N(7)-Cu(1)-N(1)	80.39(6)
Cu(1)-O(1)-H(1O)	116.5(19)
Cu(1)-O(1)-H(2O)	120.0(19)
H(1O)-O(1)-H(2O)	111(2)
C(1)-N(1)-C(9)	112.14(15)
C(1)-N(1)-C(17)	111.15(14)
C(9)-N(1)-C(17)	110.94(14)
C(1)-N(1)-Cu(1)	109.06(11)
C(9)-N(1)-Cu(1)	106.54(11)
C(17)-N(1)-Cu(1)	106.74(11)
C(2)-N(2)-C(3)	106.89(15)
C(2)-N(2)-H(2N)	126.6
C(3)-N(2)-H(2N)	126.6
C(2)-N(3)-C(8)	105.87(15)
C(2)-N(3)-Cu(1)	113.62(13)
C(8)-N(3)-Cu(1)	140.18(13)
C(10)-N(4)-C(11)	107.12(16)
C(10)-N(4)-H(4N)	126.4
C(11)-N(4)-H(4N)	126.4
C(10)-N(5)-C(16)	105.92(15)
C(10)-N(5)-Cu(1)	112.39(12)
C(16)-N(5)-Cu(1)	141.12(13)
C(18)-N(6)-C(19)	107.17(15)
C(18)-N(6)-H(6N)	126.4
C(19)-N(6)-H(6N)	126.4
C(18)-N(7)-C(24)	106.13(15)
C(18)-N(7)-Cu(1)	111.16(12)
C(24)-N(7)-Cu(1)	141.32(13)
N(1)-C(1)-C(2)	108.90(15)
N(1)-C(1)-H(1A)	109.9
N(1)-C(1)-H(1B)	109.9
N(3)-C(2)-N(2)	112.97(17)
N(3)-C(2)-C(1)	121.30(17)
N(2)-C(2)-C(1)	125.71(17)
N(2)-C(3)-C(4)	131.70(18)
N(2)-C(3)-C(8)	106.12(16)
C(4)-C(3)-C(8)	122.12(18)
C(5)-C(4)-C(3)	116.62(19)
C(4)-C(5)-C(6)	121.64(19)
C(7)-C(6)-C(5)	121.5(2)
C(6)-C(7)-C(8)	117.31(19)
C(7)-C(8)-N(3)	131.07(17)
C(7)-C(8)-C(3)	120.75(18)
N(3)-C(8)-C(3)	108.15(16)
C(10)-C(9)-N(1)	106.56(15)
N(5)-C(10)-N(4)	112.79(16)
N(5)-C(10)-C(9)	120.93(17)
N(4)-C(10)-C(9)	126.26(17)
N(4)-C(11)-C(12)	131.95(18)
N(4)-C(11)-C(16)	105.91(16)
C(12)-C(11)-C(16)	122.02(18)
C(13)-C(12)-C(11)	116.72(19)
C(12)-C(13)-C(14)	121.65(19)
C(15)-C(14)-C(13)	121.75(19)
C(14)-C(15)-C(16)	117.16(18)
N(5)-C(16)-C(15)	131.10(17)
N(5)-C(16)-C(11)	108.23(16)
C(15)-C(16)-C(11)	120.64(17)
N(1)-C(17)-C(18)	106.84(15)
N(1)-C(17)-H(17A)	110.4
N(1)-C(17)-H(17B)	110.4
N(7)-C(18)-N(6)	112.64(17)

N(7)-C(18)-C(17)	120.56(16)
N(6)-C(18)-C(17)	126.77(17)
N(6)-C(19)-C(20)	132.43(18)
N(6)-C(19)-C(24)	105.62(16)
C(20)-C(19)-C(24)	121.89(18)
C(21)-C(20)-C(19)	116.47(18)
C(20)-C(21)-C(22)	122.14(19)
C(23)-C(22)-C(21)	121.20(19)
C(22)-C(23)-C(24)	117.37(18)
N(7)-C(24)-C(23)	130.66(17)
N(7)-C(24)-C(19)	108.43(16)
C(23)-C(24)-C(19)	120.89(18)
F(4)-B(1)-F(1)	112.4(2)
F(4)-B(1)-F(2)	110.4(2)
F(1)-B(1)-F(2)	108.7(2)
F(4)-B(1)-F(3)	109.4(2)
F(1)-B(1)-F(3)	108.1(2)
F(2)-B(1)-F(3)	107.8(2)
F(8)-Si(1)-F(8)#1	180
F(8)-Si(1)-F(7)#1	89.87(7)
F(8)#1-Si(1)-F(7)#1	90.13(7)
F(8)-Si(1)-F(7)	90.13(7)
F(8)#1-Si(1)-F(7)	89.87(7)
F(7)#1-Si(1)-F(7)	180
F(8)-Si(1)-F(9)#1	89.07(5)
F(8)#1-Si(1)-F(9)#1	90.93(5)
F(7)#1-Si(1)-F(9)#1	90.31(6)
F(7)-Si(1)-F(9)#1	89.69(6)
F(8)-Si(1)-F(9)	90.93(5)
F(8)#1-Si(1)-F(9)	89.08(5)
F(7)#1-Si(1)-F(9)	89.68(6)
F(7)-Si(1)-F(9)	90.32(6)
F(9)#1-Si(1)-F(9)	180
H(1W2)-O(2W)-H(2W2)	107(2)
H(1W3)-O(3W)-H(2W3)	108(3)
H(1W4)-O(4W)-H(2W4)	109(3)
H(1W5)-O(5W)-H(2W5)	98(3)
H(1W6)-O(6W)-H(2W6)	105(4)
H(1W7)-O(7W)-H(2W7)	104.5

Table 3.3 Crystal data and structure refinement for $[Zn_2(\mu\text{-}F)(NTB)_2][SiF_6][BF_4]$

Formula	$C_{25}H_{24}B_{0.50}F_{0.50}N_6OSi_{0.50}Zn$
Formula wt (amu)	518.82
T, K	90.0(2)
Z	4
a, Å	11.8046(3)
b, Å	11.8669(3)
c, Å	13.4027(3)
α,(deg)	113.1730(10)
β, (deg)	93.0140(10)
γ, (deg)	115.4790(10)
V, Å^3	1501.45(6)
d_{calc}, Mg/m^3	2.295
F(000)	1072
Crystal size (mm^3)	.12 x .10 x .01
Radiation	Cu K_α (λ= 1.54178 Å)
Monochromator	Graded Multilayer Optics
Absorption coef (mm^{-1})	3.104
Diffractometer	Bruker X8 Proteum
Range (deg)	3.72 to 68.66
Limiting indices	$-14 \leq h \leq 14$
	$-14 \leq k \leq 12$
	$-16 \leq l \leq 15$
Reflections collected	21450
Independent reflections	5092 (R_{int} = 0.0414)
Absorption correction	Semi-empirical from equivalents
Refinement method	SHELXL-97
Refinement method	Full-matrix least-squares on F^2
Data/restraints/parameters	5431 / 16 / 395
Goodness-of-fit on F^2	0.996
Final R indices [l>2σ (l)]	R1 = 0.0732, wR2 = 0.1793
R indices (all data)	R1 = 0.0705, wR2 = 0.1778

Table 3.4 Bond Angle and Bond Distances for $[Zn_2(\mu\text{-}F)(NTB)_2][SiF_6][BF_4]$

Atoms	Distance (Å)
Zn(1)-F(1)	1.9692(6)
Zn(1)-N(5)	2.014(4)
Zn(1)-N(1)	2.025(4)
Zn(1)-N(3)	2.026(4)
Zn(1)-N(7)	2.425(4)
F(1)-Zn(1)	1.9693(6)
N(1)-C(2)	1.320(6)
N(1)-C(8)	1.390(6)
N(2)-C(2)	1.340(7)
N(2)-C(3)	1.370(7)
N(3)-C(10)	1.332(6)
N(3)-C(16)	1.401(6)
N(4)-C(10)	1.332(6)
N(4)-C(11)	1.386(7)
N(5)-C(18)	1.323(6)
N(5)-C(24)	1.386(6)
N(6)-C(18)	1.337(6)
N(6)-C(19)	1.383(6)
N(7)-C(17)	1.465(6)
N(7)-C(1)	1.462(6)
N(7)-C(9)	1.469(6)
C(1)-C(2)	1.497(7)
C(3)-C(4)	1.397(7)
C(3)-C(8)	1.408(7)
C(4)-C(5)	1.374(8)
C(5)-C(6)	1.410(8)
C(6)-C(7)	1.386(7)
C(7)-C(8)	1.396(7)
C(9)-C(10)	1.499(7)

C(11)-C(16)	1.405(7)
C(11)-C(12)	1.402(7)
C(12)-C(13)	1.379(8)
C(13)-C(14)	1.406(8)
C(14)-C(15)	1.380(7)
C(15)-C(16)	1.386(7)
C(17)-C(18)	1.497(7)
C(19)-C(20)	1.392(7)
C(19)-C(24)	1.401(7)
C(20)-C(21)	1.376(7)
C(21)-C(22)	1.408(7)
C(22)-C(23)	1.371(7)
C(23)-C(24)	1.392(7)
Si(1)-F(4)	1.670(3)
Si(1)-F(4)	1.670(3)
Si(1)-F(2)	1.688(3)
Si(1)-F(2)	1.688(3)
Si(1)-F(3)	1.707(3)
Si(1)-F(3)	1.707(3)
O(1M1)-C(1M1)	1.424(7)
B(1)- F(8)	1.301(7)
B(1)-F(6)	1.306(7)
B(1)-F(7)	1.325(7)
B(1)-F(5)	1.338(7)

Atoms	Angle (°)
F(1)-Zn(1)N(5)	103.43(11)
F(1)-Zn(1)-N(1)	102.78(11)
N(5)-Zn(1)-N(1)	114.37(16)
F(1)-Zn(1)-N(3)	102.98(11)
N(5)-Zn(1)-N(3)	116.32(16)
N(1)-Zn(1)-N(3)	114.45(16)
F(1)-Zn(1)-N(7)	179.45(10)
N(5)-Zn(1)-N(7)	76.91(15)
N(1)-Zn(1)-N(7)	76.67(15)
N(3)-Zn(1)-N(7)	77.22(15)
Zn(1)-F(1)-Zn(1)	179.998(1)
C(2)-N(1)-C(8)	106.3(4)
C(2)-N(1)-Zn(1)	117.8(3)
C(8)-N(1)-Zn(1)	135.8(3)
C(2)-N(2)-C(3)	108.3(4)
C(2)-N(2)-H(2)	125.8
C(3)-N(2)-H(2)	125.9
C(10)-N(3)-C(16)	105.8(4)
C(10)-N(3)-Zn(1)	117.2(3)
C(16)-N(3)-Zn(1)	135.6(3)
C(10)-N(4)-C(11)	107.4(4)
C(10)-N(4)-H(4)	126.3
C(11)-N(4)-H(4)	126.3
C(18)-N(5)-C(24)	106.4(4)
C(18)-N(5)-Zn(1)	118.4(3)
C(24)-N(5)-Zn(1)	135.1(3)
C(18)-N(6)-C(19)	107.9(4)
C(18)-N(6)-H(6)	126.1
C(19)-N(6)-H(6)	126.1
C(17)-N(7)-C(1)	113.8(4)
C(17)-N(7)-C(9)	113.6(4)
C(1)-N(7)-C(9)	113.1(4)
C(17)-N(7)-Zn(1)	105.3(3)
C(1)-N(7)-Zn(1)	105.4(3)
C(9)-N(7)-Zn(1)	104.4(3)
N(7)-C(1)-C(2)	109.4(4)
N(7)-C(1)-H(1A)	109.8
N(7)-C(1)-H(1B)	109.8
N(1)-C(2)-N(2)	111.9(4)
N(1)-C(2)-C(1)	123.8(4)
N(2)-C(2)-C(1)	124.3(4)
N(2)-C(3)-C(8)	105.5(4)
C(4)-C(3)-C(8)	122.4(5)
C(5)-C(4)-C(3)	116.8(5)
C(4)-C(5)-C(6)	121.5(5)
C(7)-C(6)-C(5)	121.7(5)
C(6)-C(7)-C(8)	117.4(5)
N(1)-C(8)-C(7)	131.8(4)
N(1)-C(8)-C(3)	108.0(4)
C(7)-C(8)-C(3)	120.2(4)
N(7)-C(9)-C(10)	108.6(4)
N(7)-C(9)-H(9A)	110
N(7)-C(9)-H(9B)	110
N(3)-C(10)-N(4)	112.8(4)
N(3)-C(10)-C(9)	122.3(4)
N(4)-C(10)-C(9)	124.8(4)
N(4)-C(11)-C(16)	106.3(4)
N(4)-C(11)-C(12)	131.6(5)
C(16)-C(11)-C(12)	122.1(5)
C(13)-C(12)-C(11)	115.9(5)
C(12)-C(13)-C(14)	122.3(5)
C(15)-C(14)-C(13)	121.5(5)
C(14)-C(15)-C(16)	117.3(5)
C(15)-C(16)-C(11)	121.0(5)
C(15)-C(16)-N(3)	131.3(4)
C(11)-C(16)-N(3)	107.7(4)
N(7)-C(17)-C(18)	110.3(4)
N(7)-C(17)-H(17A)	109.6
N(7)-C(17)-H(17B)	109.6
N(5)-C(18)-N(6)	111.9(4)
N(5)-C(18)-C(17)	123.3(4)
N(6)-C(18)-C(17)	124.6(4)
N(6)-C(19)-C(20)	132.1(5)
N(6)-C(19)-C(24)	105.5(4)
C(20)-C(19)-C(24)	122.5(4)
C(21)-C(20)-C(19)	116.5(5)
C(20)-C(21)-C(22)	121.2(5)
C(23)-C(22)-C(21)	122.3(5)
C(22)-C(23)-C(24)	117.0(4)

N(5)-C(24)-C(23)	131.2(4)
N(5)-C(24)-C(19)	108.3(4)
C(23)-C(24)-C(19)	120.5(4)
F(4)-Si(1)-F(4)	180
F(4)-Si(1)-F(2)	89.63(15)
F(4)-Si(1)-F(2)	90.37(15)
F(4)-Si(1)-F(2)	90.37(15)
F(4)-Si(1)-F(2)	89.63(15)
F(2)-Si(1)- F(2)	180
F(4)-Si(1)-F(3)	90.68(14)
F(4)-Si(1)-F(3)	89.32(14)
F(2)-Si(1)-F(3)	89.99(13)
F(2)-Si(1)-F(3)	90.01(13)
F(4)-Si(1)-F(3)	89.32(14)
F(4)-Si(1)-F(3)	90.68(14)
F(2)-Si(1)-F(3)	90.01(13)
F(2)-Si(1)-F(3)	89.99(13)
F(3)-Si(1)-F(3)	180
F(8)-B(1)-F(6)	107.1(7)
F(8)-B(1)-F(7)	113.3(7)
F(6)-B(1)-F(7)	109.7(8)
F(8)-B(1)-F(5)	100.9(8)
F(6)-B(1)-F(5)	111.7(7)
F(7)-B(1)-F(5)	113.7(7)

Table 3.5 Crystal Data and Structure Refinement for $[Zn(cyclen)(H_2O)][SiF_6]\bullet 2H_2O$

Formula	$C_8\ H_{26}\ F_6\ N_4\ O_3\ Si\ Zn$
Formula wt (amu)	433.79
T, K	90.0(2)
Crystal system	Monoclinic
Space group	$P2_1/c$
Z	4
a, Å	8.0122(1)
b, Å	14.1608(2)
c, Å	14.7302(2)
α,(deg)	90
β, (deg)	96.1924(5)
γ, (deg)	90
V, Å^3	1661.52(4)
d_{calc}, Mg/m^3	1.734
F(000)	896
Crystal size (mm^3)	0.26 × 0.17 × 0.10
Radiation	Mo Kα (λ = 0.7107 Å)
Monochromator	Graphite
Absorption coef (mm^{-1})	1.628
Diffractometer	NoniusKappaCCD
range (deg)	2 to 27.47
Limiting indices	$-10 \le h \le 10$
	$-18 \le k \le 18$
	$-19 \le l \le 19$
Reflections collected	41951
Independent reflections	3809 [*R*(int) = 0.0360]
Absorption correction	Semi-empirical from equivalents
Refinement method	Full-matrix least-squares on F^2
Refinement method	SHELXL-97
Data/restraints/parameters	3809 / 9 / 229
Goodness-of-fit on F^2	1.099
Final R indices [I>2σ(I)]	R1 = 0.0211, wR2 = 0.0502
R indices (all data)	R1 = 0.0243, wR2 = 0.0514
Largest diff. peak and hole	0.348 and −0.288 e.Å^3

Table 3.6 Bond Distances (Å) and Bond Angles (°) for $[Zn(cyclen)(H_2O)][SiF_6]\bullet 2H_2O$

Atoms	Distance (Å)
Zn(1)–O(1)	1.9916(10)
Zn(1)–−N(1)	2.1181(12)
Zn(1)–N(3)	2.1263(12)
Zn(1)–N(4)	2.1322(12)
Zn(1)–N(2)	2.1519(12)
O(1)–H(1O)	0.822(15)
O(1)–H(2O)	0.816(15)
N(1)–C(1)	1.4778(19)
N(1)–C(8)	1.4807(18)
N(2)–C(2)	1.4750(18)
N(2)–C(3)	1.4881(17)
N(3)–C(5)	1.4793(18)
N(3)–C(4)	1.4796(18)
N(4)–C(6)	1.4796(18)
N(4)–C(7)	1.483(2)
C(1)–C(2)	1.5208(19)
C(3)–C(4)	1.519(2)
C(5)–C(6)	1.518(2)
C(7)–C(8)	1.516(2)
Si(1)–F(5)	1.6540(9)
Si(1)–F(6)	1.6872(9)
Si(1)–F(4)	1.6910(9)
Si(1)–F(1)	1.6970(9)
Si(1)–F(2)	1.7029(9)
Si(1)–F(3)	1.7066(9)
O(1W)–H(1W1)	0.806(16)
O(1W)–H(2W1)	0.797(16)
O(2W)–H(1W2)	0.777(17)
O(2W)–H(2W2)	0.800(16)
Atoms	Angle **(°)**
O(1)–Zn(1)–N(1)	109.32(4)
O(1)–Zn(1)–N(3)	111.85(4)
N(1)–Zn(1)–N(3)	138.82(4)
O(1)–Zn(1)–N(4)	109.24(4)
N(3)–Zn(1)–N(4)	83.17(5)
O(1)–Zn(1)–N(2)	112.24(4)
N(1)–Zn(1)–N(2)	82.50(4)
N(3)–Zn(1)–N(2)	82.54(4)

N(4)–Zn(1)–N(2)	138.51(5)
Zn(1)–O(1)–H(1O)	108.4(13)
Zn(1)–O(1)–H(2O)	102.4(13)
H(1O)–O(1)–H(2O)	103.6(17)
C(1)–N(1)–C(8)	114.55(11)
C(1)–N(1)–Zn(1)	108.87(8)
C(8)–N(1)–Zn(1)	105.24(9)
C(2)–N(2)–C(3)	113.82(11)
C(2)–N(2)–Zn(1)	105.77(8)
C(3)–N(2)–Zn(1)	108.18(8)
C(5)–N(3)–C(4)	113.40(11)
C(5)–N(3)–Zn(1)	107.77(9)
C(4)–N(3)–Zn(1)	104.97(8)
C(6)–N(4)–C(7)	114.26(12)
C(6)–N(4)–Zn(1)	105.18(8)
C(7)–N(4)–Zn(1)	107.77(9)
N(1)–C(1)–C(2)	110.42(11)
N(2)–C(2)–C(1)	108.85(11)
N(2)–C(3)–C(4)	109.95(11)
N(3)–C(4)–C(3)	109.06(11)
N(3)–C(5)–C(6)	110.50(12)
N(4)–C(6)–C(5)	108.69(12)
N(4)–C(7)–C(8)	110.59(12)
N(1)–C(8)–C(7)	108.72(12)
F(5)–Si(1)–F(6)	91.50(5)
F(5)–Si(1)–F(4)	90.92(5)
F(6)–Si(1)–F(4)	177.26(5)
F(5)–Si(1)–F(1)	91.57(5)
F(6)–Si(1)–F(1)	90.81(5)
F(4)–Si(1)–F(1)	90.41(5)
F(5)–Si(1)–F(2)	91.72(5)
F(6)–Si(1)–F(2)	89.29(5)
F(4)–Si(1)–F(2)	89.36(4)
F(1)–Si(1)–F(2)	176.70(5)
F(5)–Si(1)–F(3)	179.52(5)
F(6)–Si(1)–F(3)	88.95(4)
F(4)–Si(1)–F(3)	88.64(4)
F(1)–Si(1)–F(3)	88.24(4)
F(2)–Si(1)–F(3)	88.46(4)

H(1W1)–O(1W)–H(2W1)	106(2)
H(1W2)–O(2W)–H(2W2)	111(2)

Chapter 4 Catalytic activity of [Zn(cyclen)(H_2O)]•2H_2O for Industrial Carbon Capture

4.1 Introduction

The enhancement of CO_2 absorption using a catalyst is a critical component to reduce the capital cost of CO_2 capture.[84] Specifically, an effective catalyst will increase the CO_2 hydration rate and will decrease the size of the required absorber tower needed compared to the uncatalyzed reaction. Carbonic anhydrase enzymes being metalloproteins are susceptible to thermal denaturation[128] and are therefore expected to lose activity at harsh conditions associated with industrial processes such as higher regeneration temperatures (above 100 °C), high pH and high ionic environment found in industrial conditions, where both denaturation and peptide hydrolysis can occur.[129] While carbonic anhydrases cannot be employed under industrial conditions despite their unparalleled catalytic activity, they serve as a template for development of biomimetic catalysts for carbon capture. Metal, particularly zinc, 1,4,7,10-tetraazacyclododecane (cyclen) perchlorate complexes have been reported to catalyze CO_2 hydration.[123,118,119] Based on these results, we became interested in exploring the chemistry of $[Zn(cyclen)]^{2+}$ with SiF_6^{2-} anion in order to avoid the potentially explosive perchlorate salts. [Zn(cyclen)(H_2O)]SiF_6•2H_2O was synthesized and evaluated under rigorous conditions resembling those in an industrial setting, that is, with amine and carbonate. Previous

studies of small molecule carbonic anhydrase mimics were usually evaluated only under the mild, physiologically relevant conditions optimal for carbonic anhydrase.[118,130,131] While the design of improved small molecule carbonic anhydrase mimics for carbon capture is an important endeavor,[119,130,131,132,133,134] it is equally important to ensure that this class of compounds will remain functional during industrial use. In order to circumvent the potential limitations of carbonic anhydrase and other enzymatic catalysts, here we explore the stability and activity of a small molecule zinc cyclen, which will be the focus of this work.

The overall rate constant, $k_{obs,}$ for the absorption of CO_2 in an amine or carbonate/bicarbonate solution can be expressed with the below equation:

$$k_{obs} = k_{amine}[\text{amine}] + k_{OH}[\text{OH}^-] + k_{H_2O}$$

In a carbonate/bicarbonate solution, the amine component is zero and the reaction is driven purely by the hydroxide and the hydrolysis of water. The k_{OH} term has a fast rate constant but is limited by the concentration of OH^- in solution, $<1 \times 10^3$ M, under CO_2 capture conditions (pH < 11). k_{H_2O} is so small that it can be excluded in carbonate/bicarbonate solutions at pH values above 10. When monoethanolamine (MEA) or another primary/secondary amine is present the k_{H_2O} can generally be excluded under all conditions.

The addition of catalyst to the solution allows a further term to be included in the model as expressed below:

$$k_{obs} = k_{amine}[\text{amine}] + k_{OH}[\text{OH}^-] + k_{H_2O} + k_{cat}[\text{cat}]$$

The first observation of note is that the overall rate constant for MEA, or any primary or secondary amine, is primarily driven by the extremely high concentrations of amine used in CO_2 capture solvents. This makes it extremely challenging to find a catalyst capable of enhancing the rate for primary amine absorption. Therefore, the application of catalyst to carbonate/bicarbonate or tertiary amines is a more reasonable goal. The use of tertiary amines removes the ability of the amine to react with CO_2 directly, therefore simplifying the solution speciation, and any enhancement will most likely come from the direct reaction of CO_2 with the catalyst complexes, similar to the proposed mechanism for CO_2 hydration by carbonic anhydrase. As a result, methyl diethanolamine (MDEA) and K_2CO_3 solution were chosen to study the catalytic activity.

To determine the catalytic effect of the catalyst under pseudo-first-order conditions, the reaction rate constant k_{cat} is determined by subtracting the reaction rate in the absence of enzyme, k_o from the total reaction rate k_{obs} using below equation.[135,136]

$$k_{obs} = k_0 + k_{cat}[\text{cat}]$$

Where k_o is the reaction rate without enzyme, k_{cat} is the reaction rate constant of enzyme solution, and [cat] is the catalyst solution concentration. The overall mass transfer of the system is approximated using a pseudo-first-order approximation, where the catalyst contribution is bundled into the k_{obs} term. To determine the rate constant of the overall reaction, k_{obs} is determined from the slope of the plot of rate of reaction [s^{-1}] vs. concentration of catalyst [M]. The slope of the graph gives the rate constant assuming a linear relationship is satisfied.

Using the pH-drop method[105], rate constants for CO_2 hydration in the presence of [Zn(cyclen)(H_2O)]SiF_6•2H_2O in 0.1000 M K_2CO_3 and 0.5000 M MDEA were measured: k_{obs} = 4.7374 M^{-1} s^{-1} in 0.1000 M K_2CO_3 and 0.5138 M^{-1} s^{-1} in 0.5000 M MDEA. These rate constants are lower than what was expected from the stopped-flow measurements, probably because of bicarbonate coordination to the Zn active site in these systems. Thus, it became necessary to test the catalysis of benchmark enzyme carbonic anhydrase under similar conditions to determine the threshold k_{obs} value. Carbonic anhydrase has the highest known rate constant of 10^6 M^{-1} s^{-1} at ambient temperatures and physiological pH[137,138,139] but in our system (CAER pH drop screening) k_{obs} came out to be 438797 M^{-1} s^{-1}. While zinc cyclen displays significantly slower CO_2 hydration kinetics[118] than carbonic anhydrase, on a per mass basis zinc cyclen has only a 5-fold

lower activity than carbonic anhydrase due to its lower molecular weight (455 Da vs 30000 Da). Additionally, the cyclen ligand is commercially available in large scale.[140]

4.2 Experimental

4.2.1 Materials

Potassium carbonate and methyl diethanolamine were purchased from Acros-Fisher. N_2, CO_2, 14% CO_2 in N_2 (span gas) was purchased from Scott Gross. Carbonic anhydrase NS81239 (batch PPE31476) with 38.0 g/L concentration was generously provided by Novozymes North America, Inc.

4.2.2 Setup for faster catalyst screening

The reactions were carried out in a 4-necked 250 cm^3 round-bottom flask equipped with a pH meter. 14 vol % CO_2 gas in N_2 was supplied through a mass flow controller Aalborg) at 1.0 L/min. Temperature was monitored throughout the reaction with experiments conducted at room temperature. Reaction progress was followed by monitoring the change in pH with time, as CO_2 was absorbed. Initial pH of each solution was adjusted to the same as that without catalyst solution by addition of KOH.

4.3 Results and Discussion

In order to determine catalysis of reaction by $[Zn(cyclen)(H_2O)]SiF_6 \cdot 2H_2O$, concentrations of $[Zn(cyclen)(H_2O)]SiF_6 \cdot 2H_2O$ ranging from 5.00 mM to 50.00 mM

were tested in 0.1000 M K_2CO_3 and 0.5000 M MDEA. 0.1000 M K_2CO_3 was chosen because of low concentration of K_2CO_3 to observe catalytic difference. 0.5000 M MDEA was chosen as rate of reaction was very fast in 0.1000 M MDEA to observe any catalytic difference. The rates for 0.5000 M and 1.000 M MDEA were almost the same consistent with a reaction that is limited by CO_2 concentration, and thus independent of amine. Figures 4.1−4.3 depict catalysis by [Zn(cyclen)(H_2O)]SiF_6•2H_2O in 0.1000 M K_2CO_3 with k_{obs} = 4.7374 $M^{-1}s^{-1}$. As can be seen from Figure 4.1, pH drop rate increases with the increasing [Zn(cyclen)(H_2O)]SiF_6•2H_2O concentration from 25.00 mM to 50.00 mM in 0.1000 M K_2CO_3. For the pH-drop experiments of each buffer solution, the concentration of bicarbonate species has been calculated using Henderson-Hasselbalch relation for every data point using pK_a value. These values have been plotted against time for 0.1000 M K_2CO_3 (Figure 4.2). As can be seen in Figure 4.2, as the catalyst concentration is increased, a rate enhancement of bicarbonate formation is observed. A maximum $[HCO_3]^-$, corresponding to complete conversion to bicarbonate, is observed at *ca*. 10 min regardless of catalyst concentration. k_{obs} has been calculated at pH = pK_a of the solvent.

Figures 4.4–4.5 depict catalysis by 50.00 mM [Zn(cyclen)(H_2O)]SiF_6•2H_2O in 0.1000 M K_2CO_3 when started at pH = 8.4. As can be seen from the Figure 4.1, that no measurable difference can be observed between control experiment and the catalyst

experiment from pH = 11.5 to pH = 10 whereas considerable catalytic activity can be observed at pH = 8.5. This result is consistent with the hydroxide-dominated reaction and is presumably due to the reduced contribution from [OH^-] at lower pH. Thus, a separate experiment was conducted starting at pH = 8.4 (Figures 4.4−4.5) to confirm this. As can be seen in Figure 4.4, a measurable pH difference can be observed between the control experiment and the 50.00 mM [Zn(cyclen)(H_2O)]SiF_6•$2H_2O$ at starting pH itself, thus proving that considerable effect due to catalyst can be observed at lower pH due to decreased role of OH^- concentration.

Figures 4.6−4.8 depict catalysis by [Zn(cyclen)(H_2O)]SiF_6•$2H_2O$ in 0.5000 M MDEA, with, k_{obs} = 0.5138 M^{-1} s^{-1}. As can be seen from Figure 4.6, pH drop rate increases with the increasing catalyst concentration from 5.00 mM to 30.00 mM. As noted above, the rates are very similar above pH 10, consistent with a hydroxide-dominated reaction. Again, the concentration of bicarbonate species was calculated using the Henderson-Hasselbalch relation as shown in Figure 4.7. k_{obs} has been calculated at pH = pK_a of the solvent as shown in Figure 4.8.

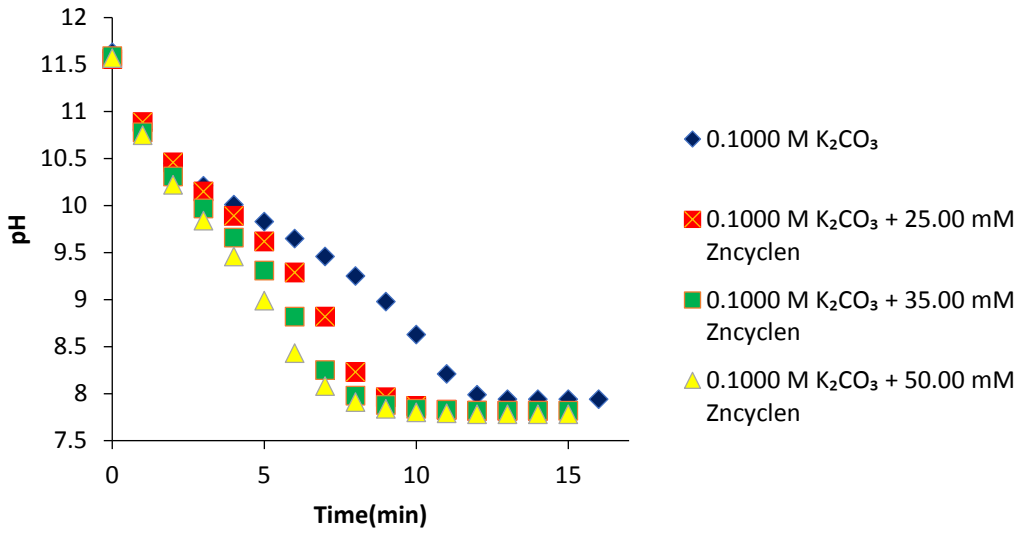

Figure 4.1 pH vs. time for $[Zn(cyclen)(H_2O)]SiF_6 \cdot 2H_2O$ in 0.1000 M K_2CO_3

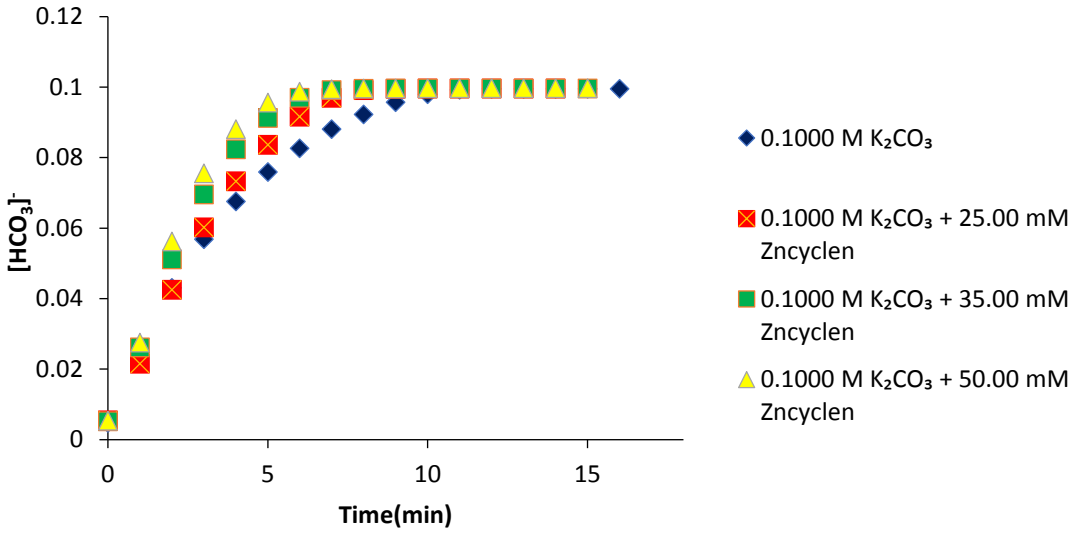

Figure 4.2 Bicarbonate concentration vs. time for $[Zn(cyclen)(H_2O)]SiF_6 \cdot 2H_2O$ in 0.1000 M K_2CO_3

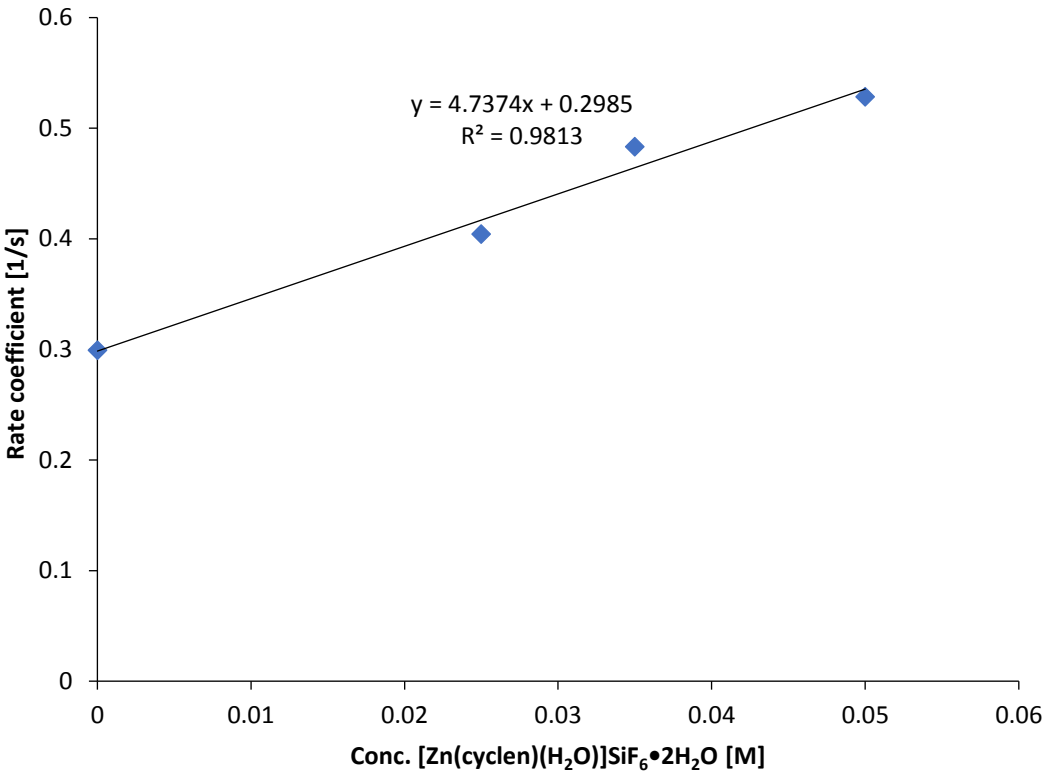

Figure 4.3 Rate constant for catalysis of bicarbonate formation by $[Zn(cyclen)(H_2O)]SiF_6 \bullet 2H_2O$ in 0.1000 M K_2CO_3 at pH = pK_a = 10.33

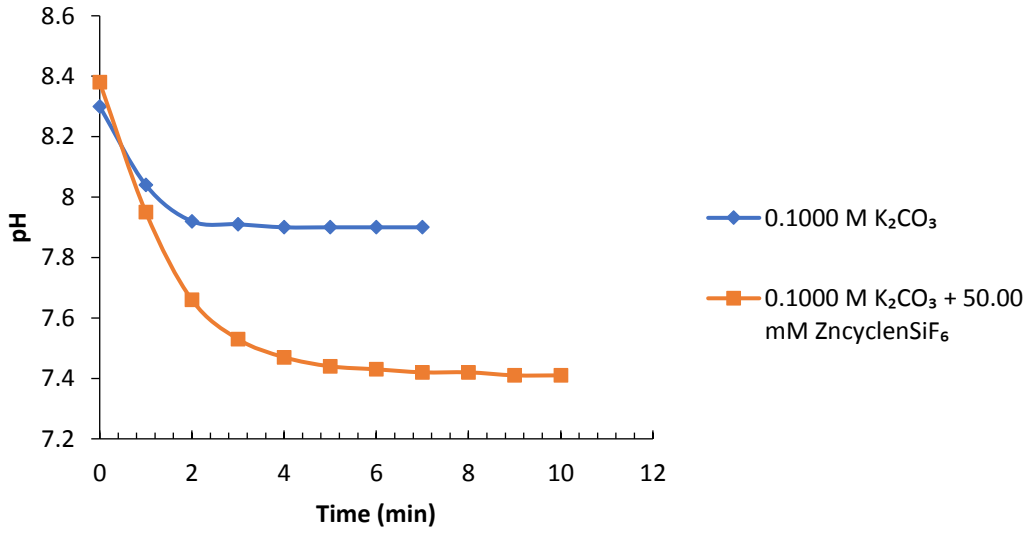

Figure 4.4 pH vs. time of 50.00 mM $[Zn(cyclen)(H_2O)]SiF_6 \bullet 2H_2O$ in 0.1000 M K_2CO_3 at pH 8.4

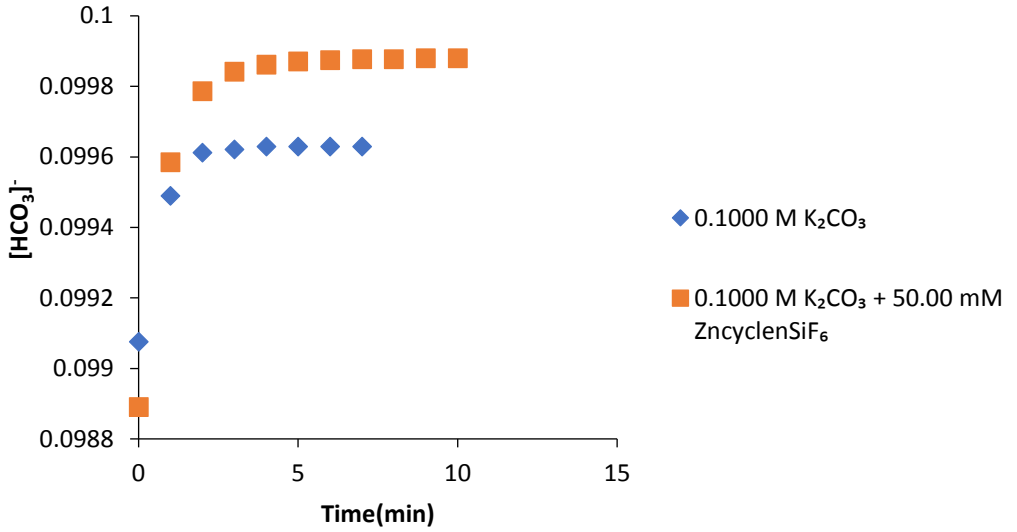

Figure 4.5 Bicarbonate concentration vs. time for 50.00 mM $[Zn(cyclen)(H_2O)]SiF_6 \cdot 2H_2O$ in 0.1000 M K_2CO_3

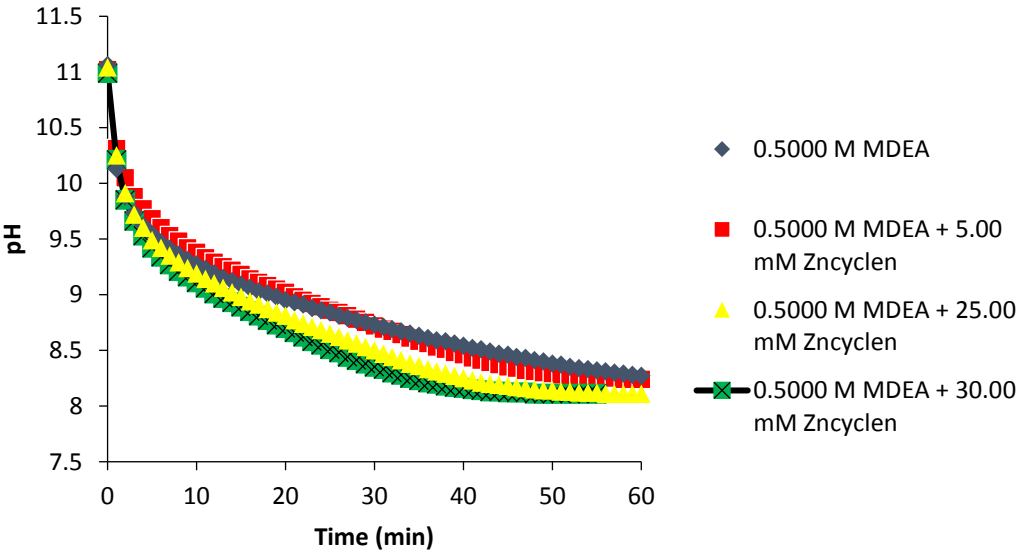

Figure 4.6 pH vs. time for $[Zn(cyclen)(H_2O)]SiF_6 \cdot 2H_2O$ in 0.5000 M MDEA

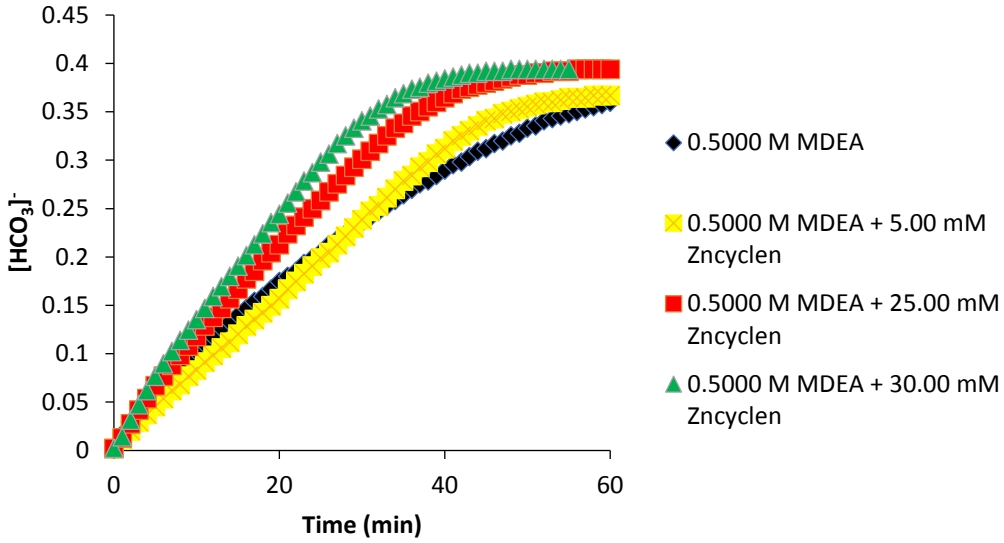

Figure 4.7 Bicarbonate vs. time for $[Zn(cyclen)(H_2O)]SiF_6 \bullet 2H_2O$ in 0.5000 M MDEA

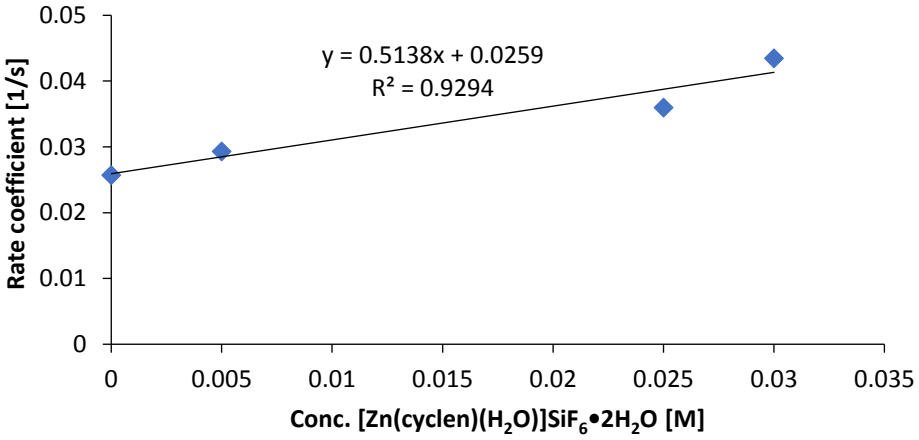

Figure 4.8 Rate constant for catalysis of bicarbonate formation by $[Zn(cyclen)(H_2O)]SiF_6 \bullet 2H_2O$ in 0.5000 M MDEA at pH = pK_a = 8.68

In catalytic reactions, it is critical to understand the fate of the catalyst. A precipitate formed as the reaction progressed during experiments. The precipitate was immediately noted upon the introduction of CO_2 gas and the amount increased as the reaction progressed. TGA and IR were not consistent with the starting zinc compound, $ZnSiF_6 \bullet 6H_2O$ (Figures 4.9, 4.10 and 4.11). IR (Figure 4.10) analysis of the precipitate suggested that it is a simple inorganic zinc salt, most likely a fluoride or silicate. IR spectra did not support the presence of carbonate, which would be evidenced by bands at 1440 cm^{-1}, 1335 cm^{-1}, 744 cm^{-1} and 729 cm^{-1}. IR spectra did suggest Si−O (1057.76 cm^{-1}) and Si−F bond (734.04 cm^{-1}) but not a simple, binary zinc silicate. The precipitate was analyzed by powder XRD and was found to be K_2SiF_6 (Figure 4.12). In order to identify the Zn species present at the end of the reaction and also to determine the yield of K_2SiF_6, a reaction mixture of 0.1000 M K_2CO_3 and $[Zn(cyclen)(H_2O)][SiF_6]$ after the reaction with CO_2 was analyzed. ^1H NMR confirmed the presence of intact $[Zn(cyclen)(H_2O)]^{2+}$. This suggests that $[Zn(cyclen)(H_2O)]^{2+}$, not a decomposition product, is the active catalyst. The results also demonstrate that the tetradentate cyclen ligand is retained during the reaction. This is an important aspect of catalyst design for the process of interest. The observation that no zinc carbonate was formed suggests that the cyclen ligand can prevent the precipitation of zinc carbonate. Loss of zinc from the catalyst active site is a potential route to catalyst inactivation in high CO_3^{2-}

concentrations. CO_3^{2-} can react with Zn^{2+} to form insoluble $ZnCO_3$ in water. Additionally, the reaction between CO_2 and water in carbonate solvent yields two HCO_3^- molecules, leading to two times higher HCO_3^- concentrations in carbonate solvents during CO_2 loading than in other (e.g. amine) solvents. Accumulation of high concentrations of bicarbonate likely increases the rate of the reverse reaction. Since the measured catalytic rate constants were lower than what would be expected for [Zn(cyclen)(H_2O)]SiF_6•2H_2O in 0.5000 M MDEA and 0.1000 M K_2CO_3, bicarbonate coordination to the Zn(II) active site may be the cause. More specifically, while the complex showed a reasonable k_{obs} of 2000 L/mol that was consistent with previously reported results using stopped-flow spectrometry kinetics testing, the activity was much lower when evaluated under conditions more consistent with CO_2 capture reaction (CAER pH drop screening). It is proposed that the lack of activity is related to coordination of the solvent to the metal. Previous complexes have shown problems with unwanted coordination of carbonate as well as other nucleophiles (e.g., counteranions) in solution by crystallographic analysis of isolated complexes. Thus, strong coordination of newly formed bicarbonate species would prevent active site regeneration (inability to reform hydroxyl species on the metal). Moreover, as the measured catalytic rate constant was lower than what would be expected for carbonic anhydrase in 0.1000 M K_2CO_3, it strengthens the fact that bicarbonate coordination to the Zn(II) active site is the cause.

This would explain why [Zn(cyclen)(H_2O)][SiF_6] and similar catalysts show lower activity when evaluated using the CAER pH drop method.

4.3.1 Calculation of K_{sp} of K_2SiF_6

Solubility of K_2SiF_6 at 20 ºC is 1.129g/1000g in water[141] or 0.00513 M

K_2SiF_6 dissociates upon dissolution:

$$K_2SiF_6\,(s) \rightleftharpoons 2\,K^+\,(aq) + SiF_6^{2-}\,(aq)$$

The K_{sp} expression is:

$$K_{sp} = [K^+]^2\,[SiF_6^{2-}]$$

$$K_{sp} = (0.01025)^2(0.00513) = 5.4 \times 10^{-7}$$

4.3.2 Calculation of solubility of K_2SiF_6 in 0.1000 M K_2CO_3

$$K_2SiF_6\,(s) \rightleftharpoons 2\,K^+\,(aq) + SiF_6^{2-}\,(aq)$$

	$K_2SiF_6(s)$	$2\,K^+(aq)$	$SiF_6^{2-}(aq)$
Initial concentration	All Solid	0.2000 M	0
Change in concentration	$-x$	$2x$	x
Equilibrium concentration	$-x$	$0.2 + 2x$	x

$$K_{sp} = [K^+]^2\,[SiF_6^{2-}]$$

$$5.4 \times 10^{-7} = [0.2 + 2x]^2\,[x]$$

$$5.4 \times 10^{-7} \approx [0.2]^2\,[x] \text{ for very small } x$$

$x = 0.0000135$ M

Thus, solubility of K_2SiF_6 is decreased in the presence of K_2CO_3 leading to more crashing out of K_2SiF_6 in 0.1000 M K_2CO_3 solution.

This left the question of precipitate yield to address. Using the same experimental conditions above, K_2SiF_6 formed at the end of the reaction was filtered, dried and weighed, in 90% yield. This suggests that a nearly quantitative salt metathesis reaction occurs, replacing SiF_6^{2-} with CO_3^{2-}.

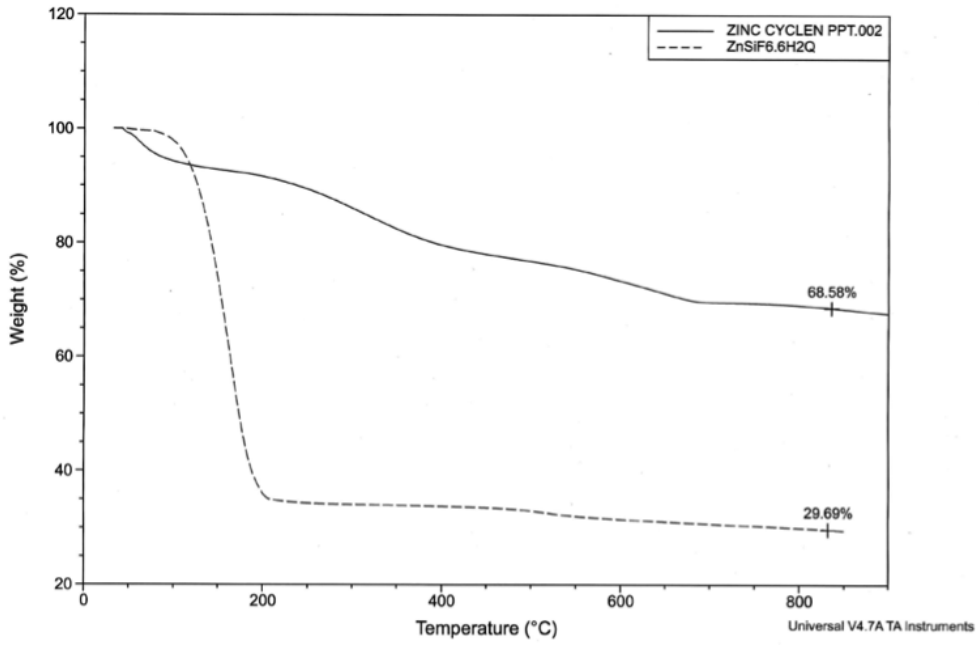

Figure 4.9 Thermograms (under air) of $ZnSiF_6 \cdot 6H_2O$ and precipitate

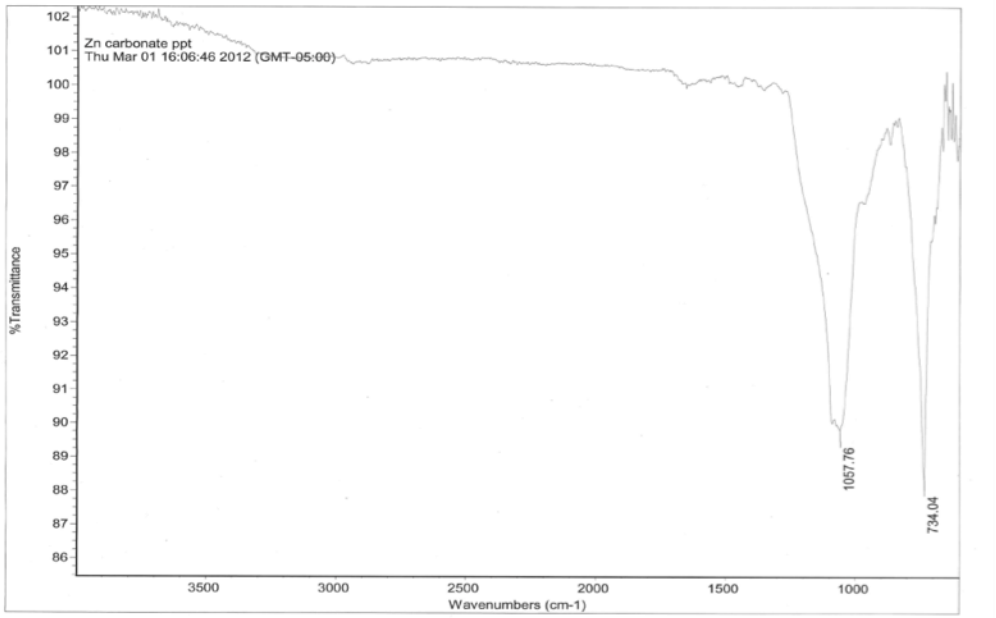

Figure 4.10 IR spectrum of precipitate

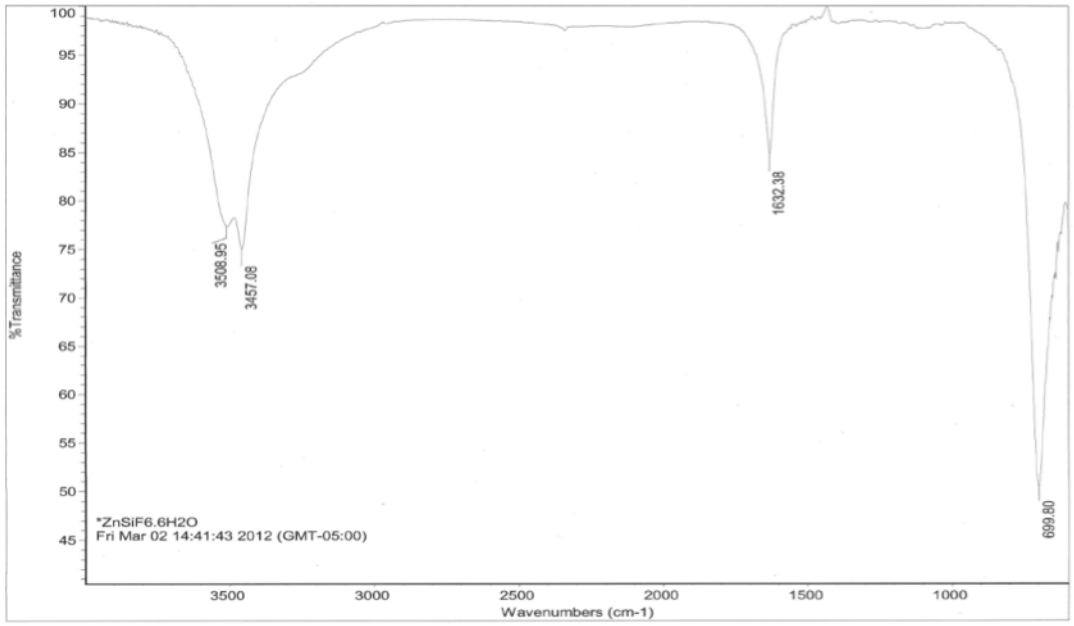

Figure 4.11 IR spectrum of $ZnSiF_6 \bullet 2H_2O$

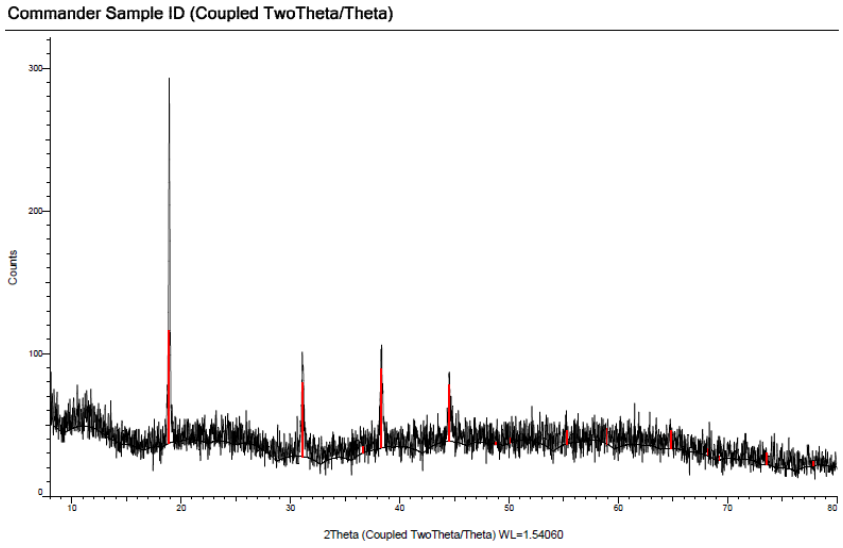

Figure 4.12 Powder XRD of K_2SiF_6

In order to compare the threshold value of the catalyst's rate constant, carbonic anhydrase was run. Initially, concentrations of carbonic anhydrase ranging from 5.00 µM to 45.00 µM were tested in 0.1000 M K_2CO_3 to determine the k_{obs} (Figures 4.13–4.14), but these concentrations were too high to observe any difference in catalysis. To determine the k_{obs}, concentrations of carbonic anhydrase ranging from 0.10 µM to 0.75 µM were tested in 0.1000 M K_2CO_3 (Figures 4.15–4.17). Figure 4.17 shows the graph to calculate the rate constant; k_{obs} = 438797 $M^{-1}s^{-1}$. Different concentrations of $[Zn(cyclen)(H_2O)]SiF_6 \cdot 2H_2O$ were run in 0.1000 M K_2CO_3 without the addition of KOH to determine the k_{obs} in this system (Figures 4.18–4.20). Figure 4.20 shows the graph to

calculate the rate constant; k_{obs} = 12.561 $M^{-1}s^{-1}$. This is improved from the k_{obs} = 4.7374 $M^{-1}s^{-1}$ found when the KOH is added in the system.

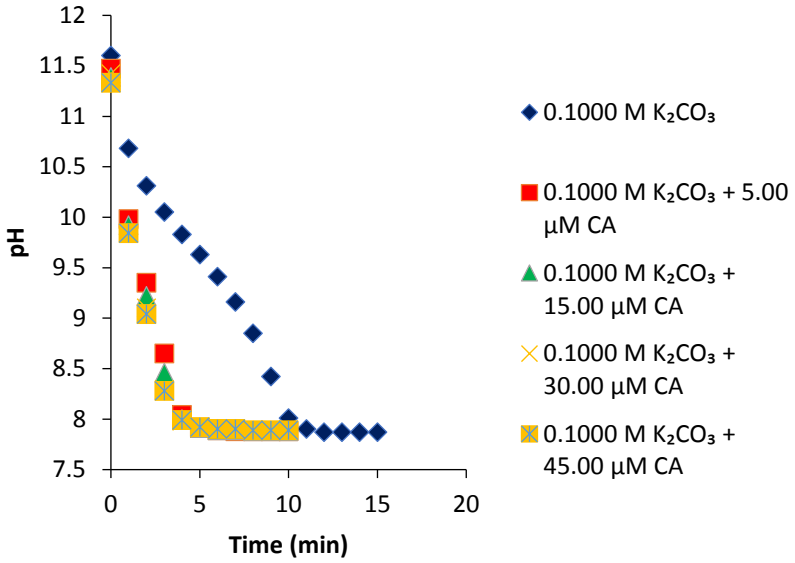

Figure 4.13 pH vs. time for carbonic anhydrase in 0.1000 M K_2CO_3

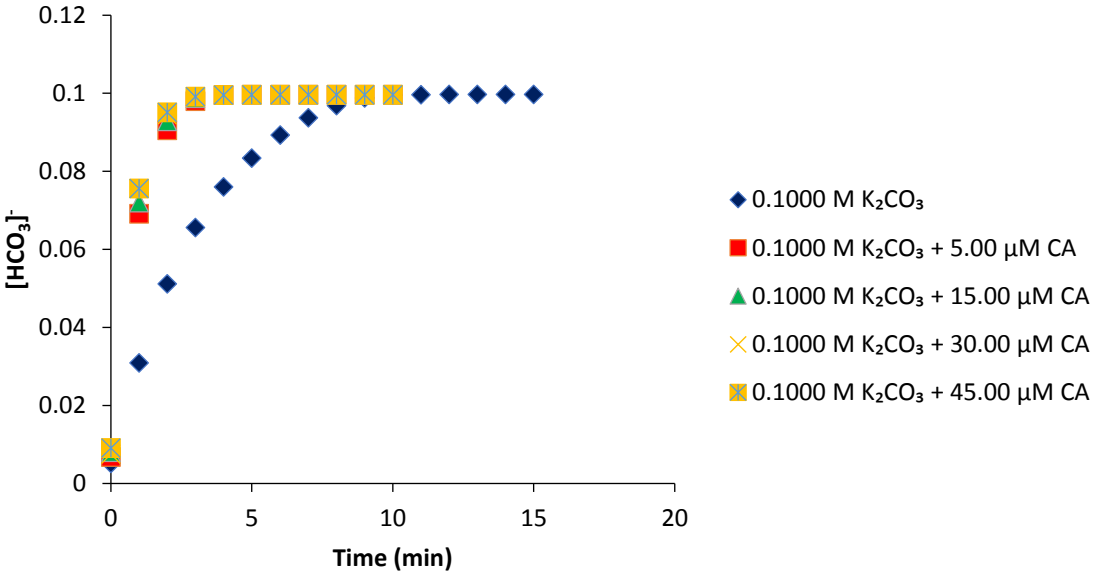

Figure 4.14 Bicarbonate concentration vs. time for carbonic anhydrase in 0.1000 M K_2CO_3

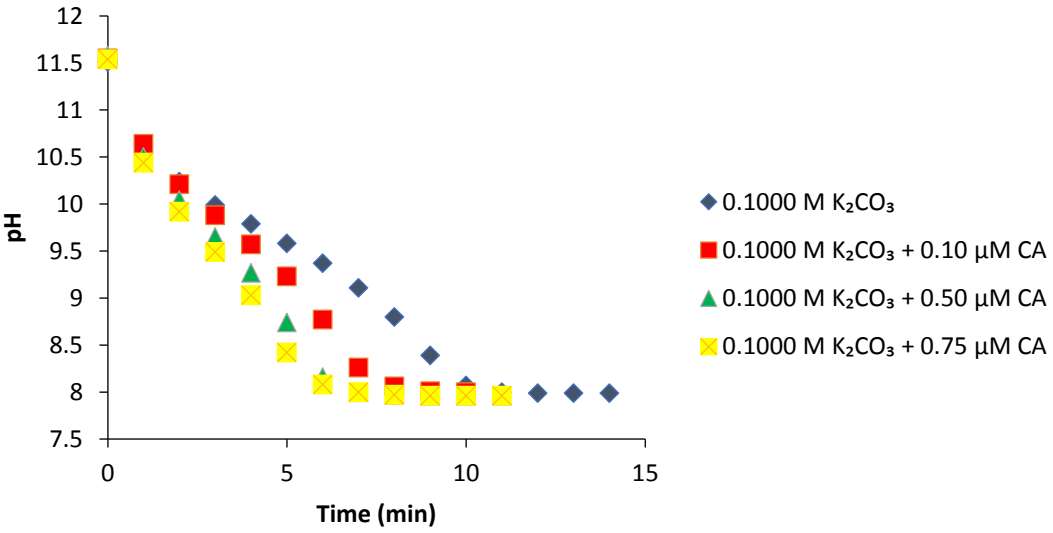

Figure 4.15 pH vs. time for carbonic anhydrase in 0.1000 M K_2CO_3

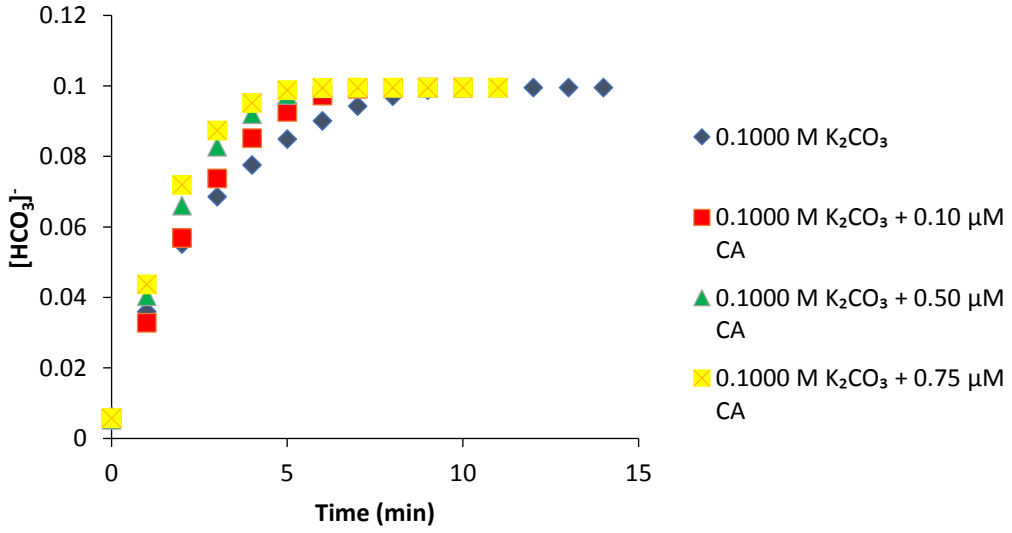

Figure 4.16 Bicarbonate concentration vs. time for carbonic anhydrase in 0.1000 M K_2CO_3

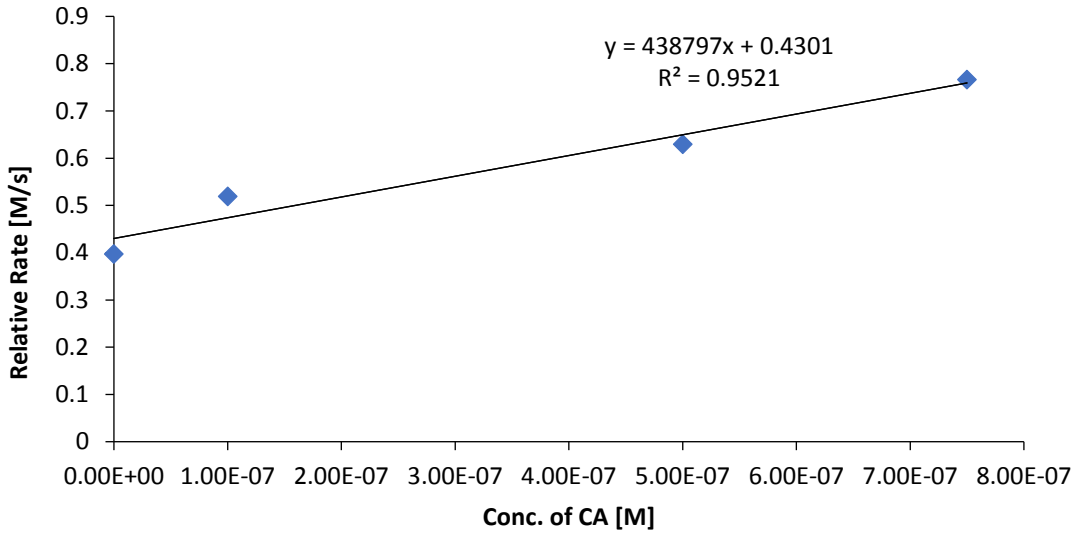

Figure 4.17 Rate constant for catalysis of bicarbonate formation by carbonic anhydrase in 0.1000 M K_2CO_3 at pH = pK_a = 10.33

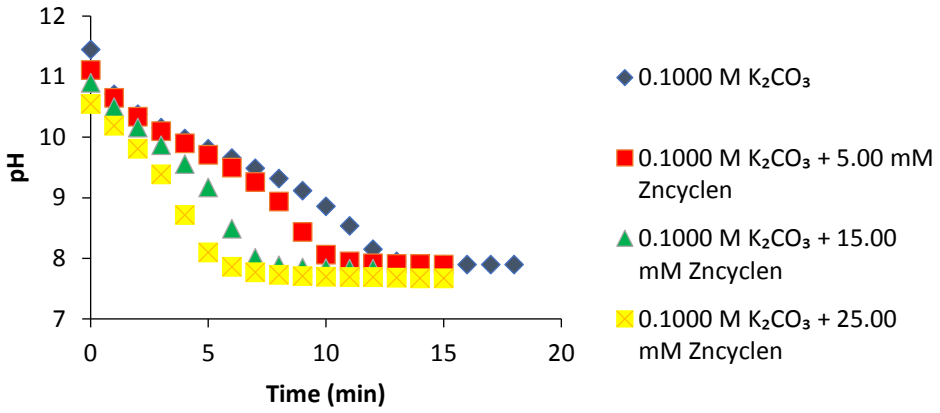

Figure 4.18 pH vs. time for [Zn(cyclen)(H_2O)]SiF_6•2H_2O in 0.1000 M K_2CO_3

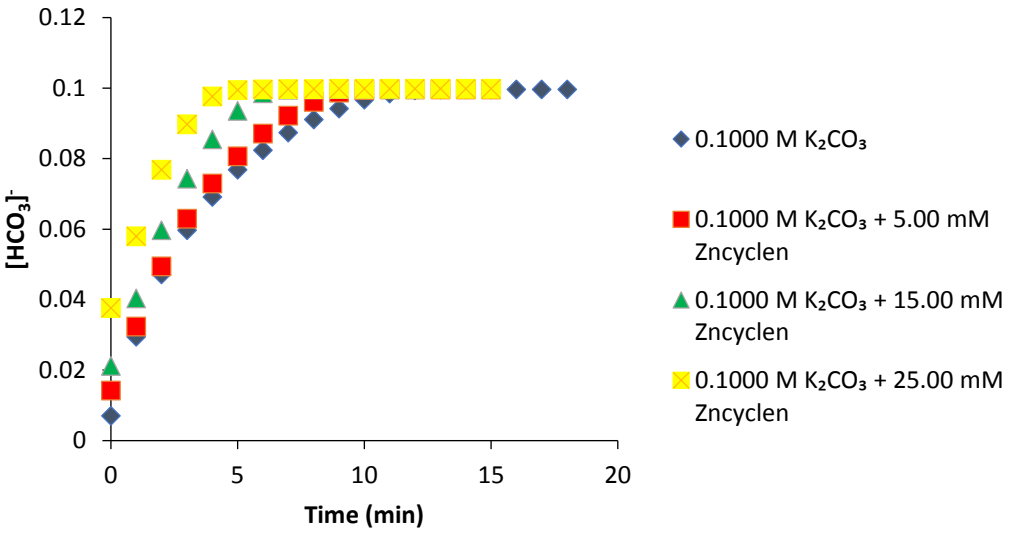

Figure 4.19 Bicarbonate concentration vs. time for $[Zn(cyclen)(H_2O)]SiF_6 \bullet 2H_2O$ in 0.1000 M K_2CO_3

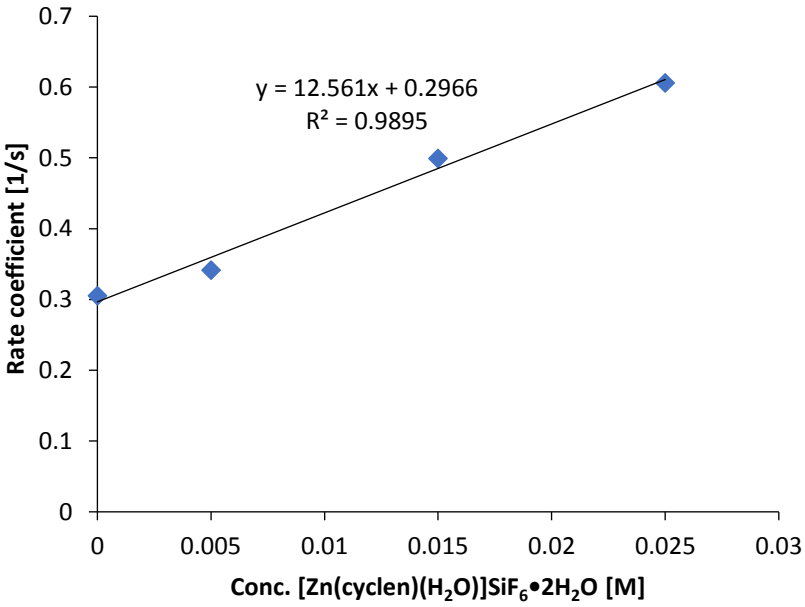

Figure 4.20 Rate constant for catalysis of bicarbonate formation by $[Zn(cyclen)(H_2O)]SiF_6 \bullet 2H_2O$ in 0.1000 M K_2CO_3 at pH = pK_a = 10.33

4.4 Conclusions

Zinc cyclen is one of the most stable carbonic anhydrase mimics because the cyclen ligand is a highly stable macrocyclic chelator as described by the chelate effect.[142] The activity of Zn cyclen is lower when evaluated under conditions more consistent with CO_2 capture reaction (CAER pH-drop screening). The determined value using the assay here was 1000 times lower than that determined using stopped-flow kinetic measurement in 0.1 M AMPSO buffer. While stopped-flow spectrophotometry enables the direct measurement of the overall reaction rate, stopped flow is most accurate when using moderate buffer concentrations and pH ranges, and when the buffer and indicator have similar pK_a values.[143] These rate constants are lower than what was expected from the stopped-flow measurements, probably because of bicarbonate coordination to Zn active site in these systems. The Zn center is highly electron deficient and therefore easily coordinates anions, inhibiting the ability to reform hydroxyl species on the metal. The cationic complex attracts anionic species such as bicarbonate into its secondary coordination sphere to maintain charge balance which drives the equilibrium to the bicarbonate-bound species. Thus, it became necessary to test the catalysis of benchmark enzyme carbonic anhydrase under similar conditions to determine the threshold k_{obs} value. Carbonic anhydrases catalyze the hydration of carbon dioxide at ambient temperatures and physiological pH with the highest known rate constant = 10^6 M^{-1} s^{-1}

[137,138,139], but in our system (CAER pH drop screening) k_{obs} came out to be 438797 M^{-1} s^{-1}. The lower catalytic rate constant for carbonic anhydrase in 0.1000 M, similar to Zn-cyclen, strengthens the conjecture that at high bicarbonate concentrations, HCO_3^- binding to the Zn(II) active site slows catalysis by inhibiting bicarbonate displacement with water to regenerate the active species. Therefore, routes for circumventing inhibition of carbon capture catalysts are broadly required. Strong bicarbonate and carbonate inhibition have been observed for some isoforms of carbonic anhydrase[144,145] and may represent a considerable challenge in catalyzed CO_2 capture. However, the fact that some carbonic anhydrase isoforms are inhibited to a lesser extent than others[144] suggests that carbonic anhydrase mimics might be designed to minimize bicarbonate and carbonate inhibition. While some variants of carbonic anhydrase minimize bicarbonate inhibition by protecting the active site with a hydrophobic pocket, other approaches to catalyst design may include using an anionic ligand to repel bicarbonate and other potential anionic inhibitors.

The complexes containing anionic ligands that donate electron density into the metal center may serve to remove anionic bicarbonates/carbamates from the secondary coordination sphere and away from the metal center, thereby facilitating bicarbonate/anion dissociation and increasing CO_2 hydration rates. The electron donation facilitates the dissociation of the formed bicarbonate, typically the rate-limiting step, regenerating the catalytically active species under basic conditions.[146] We propose the

above as key features in achieving catalytic rates large enough to contribute to the overall mass transfer in concentrated primary amine-based solvents. Catalytic activity of some of the anionic ligands will be discussed in next chapter.

Chapter 5 Synthesis and Catalysis of Anionic Complexes

5.1 Introduction

The development and study of carbonic anhydrase mimics for CO_2 hydration has been explored by several research groups[113, 118, 147] but there are no carbonic anhydrase mimics that are currently employed in power plants for post-combustion absorption of CO_2. Utilization of homogeneous catalysts for post-combustion carbon capture is plagued with difficult challenges, such as water solubility, water and air stability, and redox inertness. Direct structural mimics tend to dimerize, strongly bind anions, and perform undesirable side reactions due to the lack of a secondary coordination environment to control the reaction process.[146]

Significant catalytic and mechanistic work has been performed on [Zn(cyclen)] system, one of the most efficient carbonic anhydrase mimics;[118] however, their activities are still not comparable to benchmark carbonic anhydrase. As described in Chapter 4, we observed [Zn(cyclen)] complex to be even less active under conditions similar to industrial carbon capture. Under similar conditions, activity of carbonic anhydrase was found to be significantly lower too. This is due to inhibition by strong coordination of anions that block the active site. This strong affinity for anion coordination inhibits bicarbonate dissociation, thereby inhibiting catalyst activity. Bicarbonate dissociation is believed to be the rate-limiting step and largest barrier for catalyst to overcome. This

result suggests that ligand environments that donate electron density into the metal center will facilitate bicarbonate dissociation and increase the rate of CO_2 hydration. The above criteria guided the choice to select new catalyst candidates.

The testing of homogeneous CO_2 hydration catalysts has mostly been reported in dilute tertiary amine or carbonate salt solutions in the presence of a concentrated CO_2 stream in stopped-flow conditions. These experiments are a far reach from conditions observed in post-combustion carbon capture, which typically utilize concentrated amine-based or carbonate solvents and a dilute CO_2 stream (14%). Upon identification of the potential CO_2 hydration catalysts, we tested their catalytic activities under conditions similar to post-combustion carbon capture via pH drop method. Reported herein is the synthesis and analysis of catalysts comprised of zinc centers with electron-donating, anionic ligands.

5.2 Experimental

5.2.1 Materials

All reactions were run under a nitrogen atmosphere with constant stirring. Zinc acetate tris(pyrazolyl)borate complex was prepared by using known procedures.[147-148] $CDCl_3$, acetone-d_6, DMSO-d_6 and D_2O (Cambridge Isotopes) and reagent-grade solvents (acetone, methanol, ethanol, diethyl ether, dichloromethane, THF) were used as they

were obtained commercially. Acetonitrile was dried and distilled over magnesium sulfate. Potassium carbonate (purity > 99%), $Zn(BF_4)_2 \bullet xH_2O$, were procured from Sigma-Aldrich. Pyridine-2,6-dicarbonyl chloride, 2,6-dimethylaniline, triethylamine, diethyl zinc (Acros) and other reagents were obtained from the indicated commercial sources and used without purification. Span gas (14% CO_2 in N_2), pure N_2 and pure CO_2 were supplied by Scott-Gross. Melting points were recorded on either a Thomas-Hoover melting apparatus or Digi-Melt apparatus. TGA analyses were done on Thermal Analysis Hi-Res TGA 2950 instrument. In a typical run, 10–15 mg of the sample was loaded in a platinum pan. For all the analyses, a Hi-Res dynamic ramp 12.5 °C min^{-1}, Hi-Res 4.0, RT to 1000 °C was used under constant argon flow (65 mL/min). Infrared spectra of solid complexes were recorded in ATR mode between 4000 and 400 cm^{-1} on a Perkin-Elmer Paragon 1000 FT-IR spectrophotometer. ^{1}H and ^{13}C NMR spectra were recorded on a Varian Gemini 400 spectrometer at room temperature, unless mentioned otherwise, and were referenced to residual solvent peaks. Mass spectra was acquired by the University of Kentucky mass spectrometry facility. High-resolution electron impact (EI) ionization mass spectra were recorded at 25 eV on JEOL JMS-700T station and were referenced to perfluorokerosene (PFK). FAB-mass spectra were obtained on a Finnigan Polaris Q in EI mode via direct insertion probe. The accelerating voltage was 10 kV. The mass spectrometer was operated in positive ion mode and mass spectra were calibrated by

Alkali-CsI positive. X-ray diffraction data was collected on at 90K on either a Nonius Kappa CCD diffractometer or a Bruker-Nonius X8 Proteum diffractometer. Crystal indexing and data processing were performed either with DENZO- SMN (KappaCCD) or with Bruker APEX2 (X8 Proteum). The structures were solved and refined with SHELXS-97. Elemental analyses were performed at the Center for Applied Energy and Research at University of Kentucky.

5.2.2 Setup for faster catalyst screening

The reactions were carried out in a 4-necked 250 cm^3 round-bottom flask equipped with a pH meter. 14 vol % CO_2 gas in N_2 was supplied through an Aalborg mass flow controller at 1.0 L/min. Temperature was monitored throughout the reaction with experiments conducted at room temperature. Reaction progress was followed by monitoring the change in pH with time, as CO_2 was absorbed.

5.2.3 Synthesis of ligands

5.2.3.1 *N,N'*-Bis(2,6-dimethylphenyl)-2,6-pyridinedicarboxamide[149]

A solution of pyridine-2,6-dicarbonyl chloride (1.0 g, 5.0 mmol) at 0 °C in THF (150 mL) was added slowly to a mixture of 2,6-dimethylaniline (1.21 g, 10.0 mmol) and triethylamine (1.41 mL, 10.0 mmol). The reaction mixture was warmed to room temperature, stirred for 5 h, and filtered. The light-yellow residue obtained by removal of solvent was treated with hexane (10.0 mL) and washed with a small volume of

dichloromethane/ether (1:5 v/v) to give the pure product as a white powder (1.4 g, 80%). Spectroscopic and physical properties of ligand matched as described in literature.

5.2.3.2 Synthesis of KL[1147]

5.2.3.2.1 Step 1: 5-methyl-3-(4′-pyridyl)pyrazole[148]

A mixture of (18.7 g, 0.10 mole) of methyl isonicotinate, 20 ml of acetone and (5.90 g, 0.11 moles) of NaOMe dissolved in dry ether were heated under reflux with stirring for 2.5 hr. The mixture was cooled, acidified with 10 ml of AcOH, and diluted with 50 ml of H_2O. Organic layer was separated, and the aqueous phase was extracted with Et_2O. Ether layer was dried with $MgSO_4$ and concentrated under reduced pressure to provide 13.7 g of a red liquid, 1-(4-pyridinyl)butane-l,3-dione. (5.0 g ,0.03 mole) of 1-(4-pyridinyl)butane-l,3-dione was added during 15 min with stirring to 11 ml of 100% hydrazine hydrate; the temperature of the solution rose. The mixture was stirred at room temperature for 1 hour, diluted with 17 ml of H_2O, and cooled overnight at 5 °C. The white solid which separated was collected and dried. Yield 70%. ^{1}H NMR (400 MHz, ([D_6] DMSO): δ=8.544-8.533 (d, 2H), 7.704-7.692 (d, 2H), 6.609 (s, 1H), 2.271 (s, 3H).

5.2.3.2.2 Step 2: KL[1]

A mixture of (3.14 g, 19.7 mmol) of 5-methyl-3-(4′-pyridyl)pyrazole and (266 mg, 4.93 mmol) of KBH_4 was stirred in a three-necked 100-mL flask equipped with an immersing thermometer. The temperature was slowly increased to 200 °C over a period of 30 min.

At 140–160 °C, the mixture melted and the gas evolution became brisk. The melt was stirred continuously at 200 °C until it started to turn brown (ca. 3 h) and then slowly cooled to room temperature. The resulting glassy residue was carefully powdered and refluxed in 50 mL of toluene for 30 min, in order to remove unreacted pyrazole impurities. The mixture was filtered while hot, and the light brown residue was washed 3 times with 2.5 mL of boiling toluene and once with 2.5 mL of petroleum ether (30–50 °C). Recrystallization from 50 mL of acetonitrile at yielded 1.25 g (50 %) of KL^1 as colorless crystals, m.p. 328 °C. ^{1}H NMR ([D_6] DMSO): δ = 2.02 [s, 9 H, Me(pz)], 6.418 [s, 3 H, H(pz)], 7.709-7.698 (dd, *J* = 4.5 and 1.5 Hz, 6 H, Py), 8.550-8.539 (dd, *J* = 4.5 and 1.5 Hz, 6H, Py) ppm.

5.2.3.3 Bis(5-sulfonatosalicylaldehyde)zinc(II) disodium salt

5-sulfonatosalicylaldehyde sodium salt (3.30 g, 14.6 mmol) was dissolved in an aqueous solution of sodium hydroxide (15.0 mL, 1.0 M). A solution of $ZnCl_2$ (0.66 g, 4.81 mmol, dissolved in 6.0 mL of water) was then added slowly to the solution. The yellow solution became white after one hour of agitation. The solid was filtered, washed with cold ethanol and dried under vacuum. Yield is mass 84.2%. ^{1}H NMR ([D_6] DMSO): δ = 9.51 (s, 1 H), 7.62 (d, J = 2.5 Hz, 1 H), 7.49 (dd, J = 2.5, 8.7 Hz, 1 H), 6.55 (d, J = 8.7 Hz, 1 H) ppm. IR (KBr pellet): 3585 (m), 3519 (m), 3218 (m), 2872 (w), 2785 (w), 1651 (s),

1525 (m), 1463 (s), 1406 (m), 13356 (w), 1171 (s), 1122 (s), 1043 (s), 921 (w), 841 (w), 753 (w), 676 (m), 615 (m), 518 (w), 451 (w) cm^{-1}

5.2.4 Synthesis of complexes

5.2.4.1 Attempted synthesis of 1:1 Zn complex of *N,N'*-bis(2,6-dimethylphenyl)-2,6-pyridinedicarboxamide

A solution of (0.5 g, 1.3 mmol) of *N,N'*-bis(2,6-dimethylphenyl)-2,6-pyridinedicarboxamide was added slowly via cannula transfer to (5.2 mL, 5.2 mmol) of 1.0 M diethylzinc in hexanes. Immediate precipitate formation started. The reaction was left overnight for stirring. Precipitate obtained was washed with THF and vacuum dried to give the powder. Yield: mass 60%. Powder was found partially soluble in most organic solvents. MALDI-MS was obtained. Peak at 810 suggests 2:1 (ligand: zinc complex) whereas peak at 873 suggests presence of 2:2 (ligand: zinc complex).

5.2.4.2 Synthesis of Zn complex of KL^1:[147]

A solution of (174 mg, 0.79 mmol) of $Zn(OAc)_2 \cdot 2H_2O$ in 5 mL of methanol was added dropwise to a solution of (379 mg, 0.72 mmol) of in 20 mL of methanol/dichloromethane (1:1) over a period of 5 min. After 6 h of stirring, a small amount of a cloudy precipitate was removed by filtration, and the clear filtrate was concentrated to dryness in vacuo. Recrystallization from methanol yielded 401 mg (91 %) of complex as large colorless crystals, m.p. 242 °C. ^1H NMR ([D_6] DMSO): δ = 1.51 (s, 3 H, Ac), 2.56 [s, 9 H,

Me(pz)], 6.64 [s, 3 H, H(pz)], 7.60 (dd, *J* = 4.6 and 1.4 Hz, 6 H, Py), 8.60 (d, *J* = 6.0 Hz, 6 H, Py) ppm.

5.2.4.3 Synthesis of [Zn{Salen(SO_3Na)}]

Ethylenediamine (237 μL, 3.50 mmol) was added to a mixture of ethanol (70 mL) previously degassed for 15 min. Bis(5-sulfonatosalicylaldehyde)zinc(II) disodium salt (2.0 g, 3.5 mmol) was introduced, and the mixture was stirred for two hours at 90 °C. The white solid was filtered, washed with ethanol and dried under vacuum. Yield is 70%. ^{1}H NMR ([D6] DMSO): δ = 8.43 (s, 1 H), 7.41 (d, J = 2.4 Hz, 1 H), 7.32 (dd, J = 2.4, 8.8 Hz, 1 H), 6.52 (d, J = 8.8 Hz, 1 H), 3.72 (s, 2 H) ppm. IR (KBr pellet): 3604 (s), 3523 (s), 3447 (m), 1641 (s), 1601 (m), 1537 (s), 1472 (s), 1382 (m), 1341 (m), 1312 (m), 1205 (s), 1169 (s), 1123 (s), 1045 (s), 986 (w), 945 (w), 931 (w), 901 (w), 833 (m).

5.3 Results and Discussion

5.3.1 Pincer complexes

Recently, it has been reported by Holm that a planar nickel complex $[Ni^{II}(NNN)(OH)]^-$ containing a tridentate 2,6-pyridinedicarboxamidate pincer ligand and a terminal hydroxide ligand carries out an extremely rapid CO_2 fixation reaction.[150-151] For this bimolecular reaction, the reported (extrapolated) rate constant is 9.5×10^5 M^{-1} s^{-1} in N,N′-dimethylformamide at 298 K, a value within the range of $k_{cat}/K_M \approx 10^5$–10^8 M^-

[1] s^{-1} for carbonic anhydrase. The initial event is the formation of a weak precursor complex between the Ni-OH group and CO_2, followed by insertion of a CO_2 oxygen molecule into the Ni-OH bond to generate a four-center Ni(η^2-OCO_2H) transition state similar to that at the zinc site in carbonic anhydrase. Carbon dioxide may react with free or metal-bound hydroxide to afford products containing bicarbonate or carbonate, often captured as ligands bridging two or three metal sites. Thus, we got interested in forming Zn analogue of these complexes. Scheme 5.1 describes the synthesis of Zn complex of *N*,*N'*-bis(2,6- dimethylphenyl)-2,6-pyridinedicarboxamide.

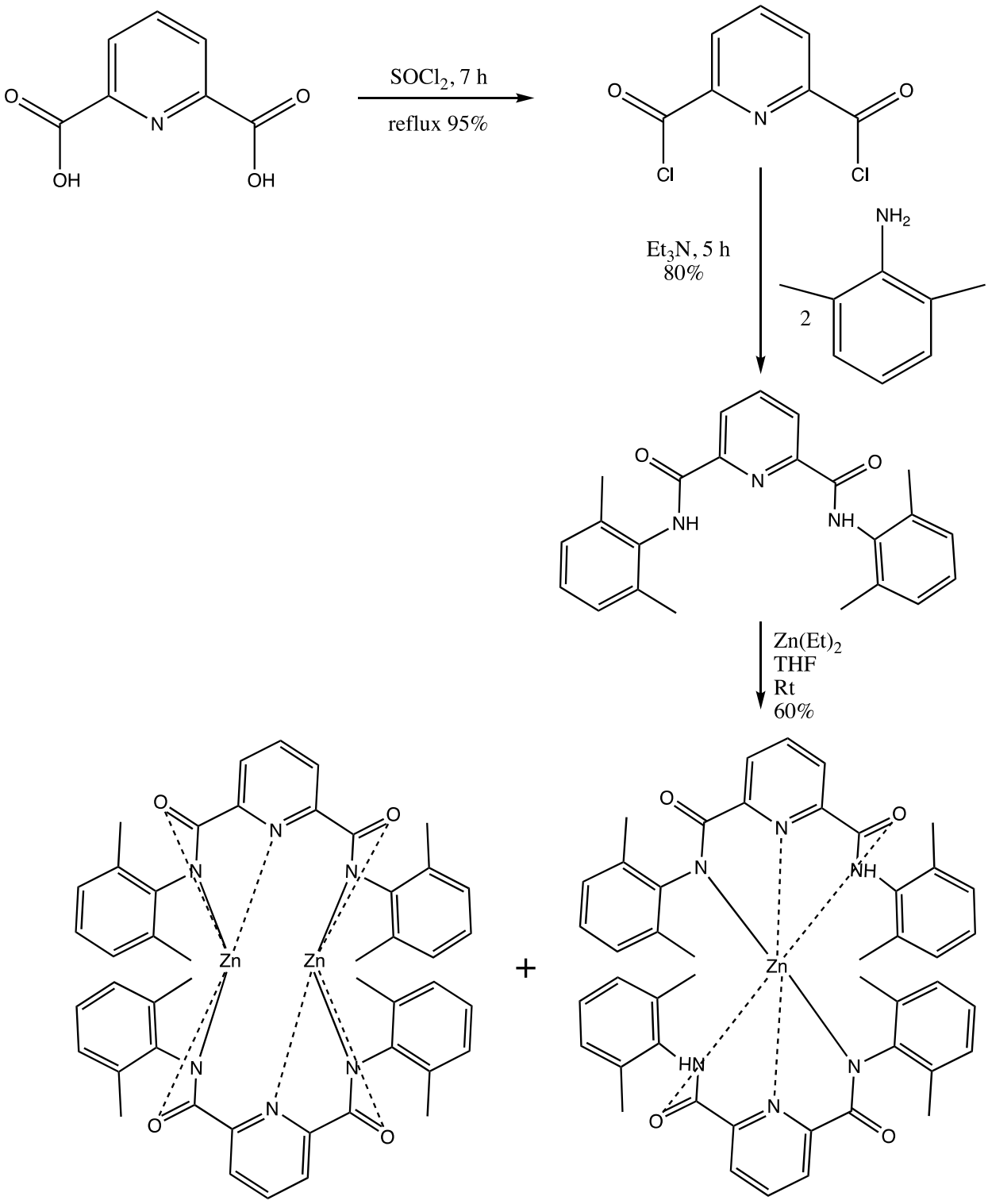

Scheme 5.1 Synthesis of Zn complex of *N,N'*-bis(2,6-dimethylphenyl)-2,6-pyridinedicarboxamide

However, we were not able to isolate pure 1:1 Zn complex from the mixture of both the complexes. Due to insolubility of mixture in various common solvents, neither we were able to fully characterize compounds, nor we were able to test catalytic activity of these complexes. However, MALDI-MS (Figure 5.1) is indicative that both the complexes are formed.

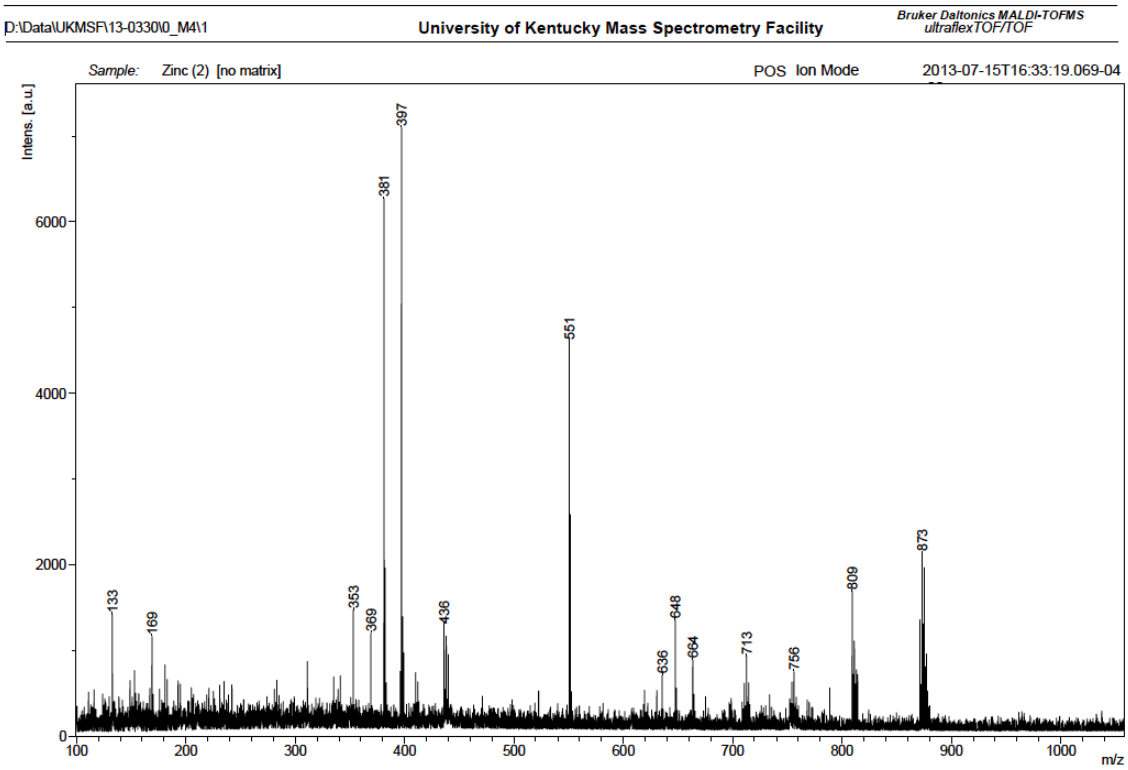

Figure 5.1 Maldi-MS spectrum of Zn complex of *N*,*N'*-bis(2,6-dimethylphenyl)-2,6-pyridinedicarboxamide

5.3.2 Tris(pyrazolyl)borate complexes

Trofimenko's tris(pyrazolyl)borate (Tp) ligands have been the key to success in biomimetic zinc enzyme chemistry.[147] Vahrenkamp has extensively contributed to Tp

ligands[117, 147, 152-168] in the field of zinc complexes, for simple Tp*Zn–OH systems as well as for a carbonic anhydrase enzyme model.[169] One of the reasons being that their structures can be varied, for example, by attaching various substituents at the 3- and 5-positions of their pyrazole rings. Substituents as small as methyl groups at the 5-positions protect the B-N bonds, preventing hydrolytic destruction of the ligands due to the presence of zinc ions. The substituents at the 3-positions create and control the protective pocket around the zinc ion, which is the active center of the enzyme model.[169] Their organic substituents disfavor access of water to the functional Zn–X center, but favor product inhibition, i.e. the formation of uncharged molecular complexes by attachment of the hydrolysis products to zinc. The way out of this dilemma required a more hydrophilic Tp*Zn chemistry by the incorporation of suitable substituents in the Tp* ligands. This is not a trivial task, as these ligands are hydrolyzable boron–nitrogen compounds and their standard synthesis requires temperatures up to 200 °C. We decided to choose pyridyl-substituted Tp* complexes as they were water-soluble and best suited for our purposes. Pyrazolyl ligand coordinates to the zinc ion in the tripodal fashion, it contains donor functional groups, it engages in various kinds of hydrogen bonds, and it forms water soluble complexes. It enforces coordination numbers higher than four for zinc. Variability in coordination numbers and geometries is a prerequisite for catalytic activity. These characteristics make them an attractive candidate for CO_2 hydration. The Tp*Zn–

OH complexes owe their stability both to the fact that the sterically laden Tp* ligands enforce a low coordination number and that they create a hydrophobic pocket around the Zn–OH unit. Their organic substituents disfavor access of water

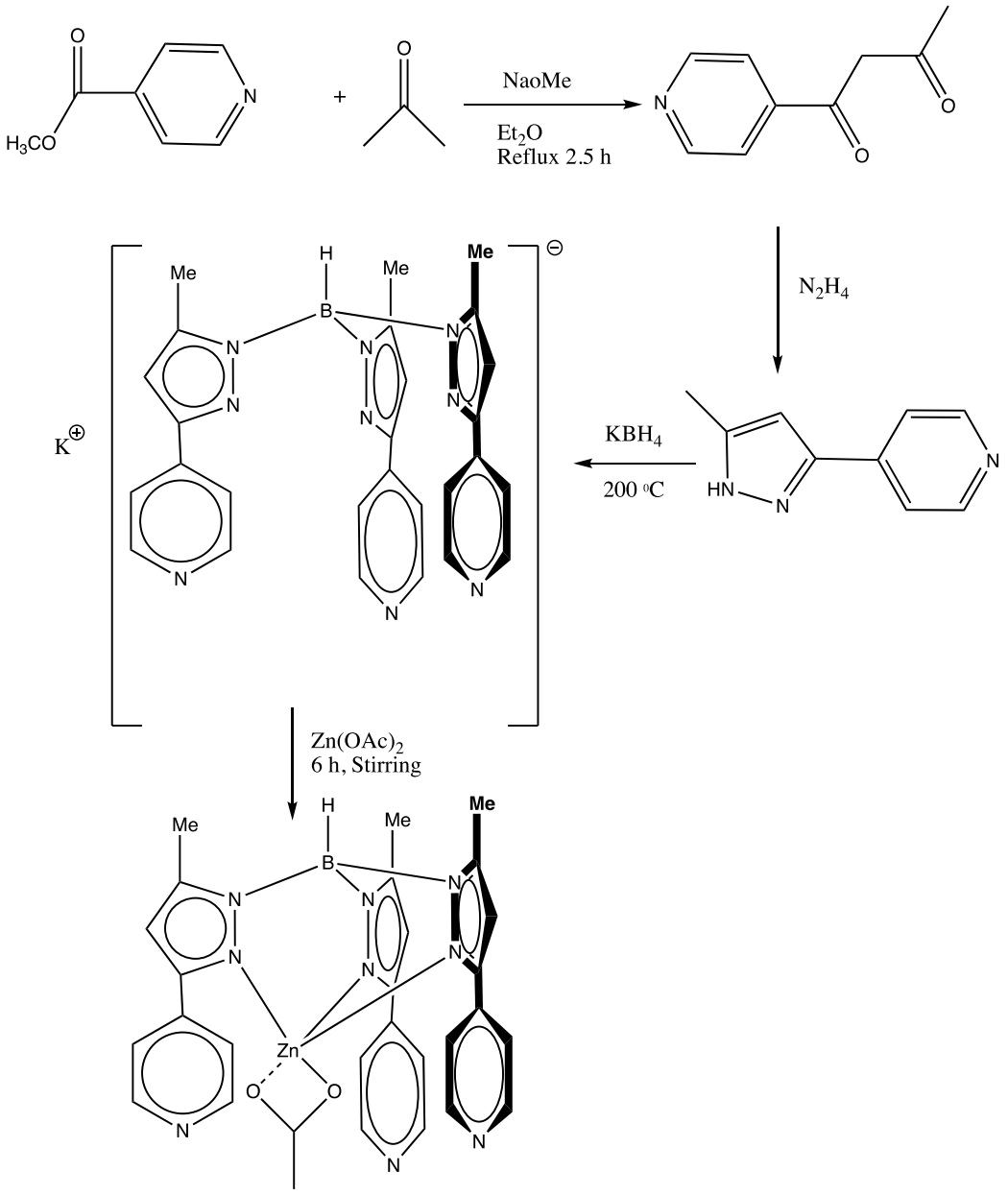

Scheme 5.2 Synthesis of zinc complex of KL[1]

to the functional Zn–X center, but favor product inhibition, i.e. the formation of uncharged molecular complexes by attachment of the hydrolysis products to zinc. The way out of this required a more hydrophilic Tp*Zn chemistry by the incorporation of suitable substituents in the Tp* ligands.

We decided to choose pyridyl- substituted Tp* complexes as they were water-soluble and best suited for our purposes. Scheme 5.2 describes synthesis of zinc complex of KL^1 and figure 5.2 depict catalysis by complex in 30% MEA.

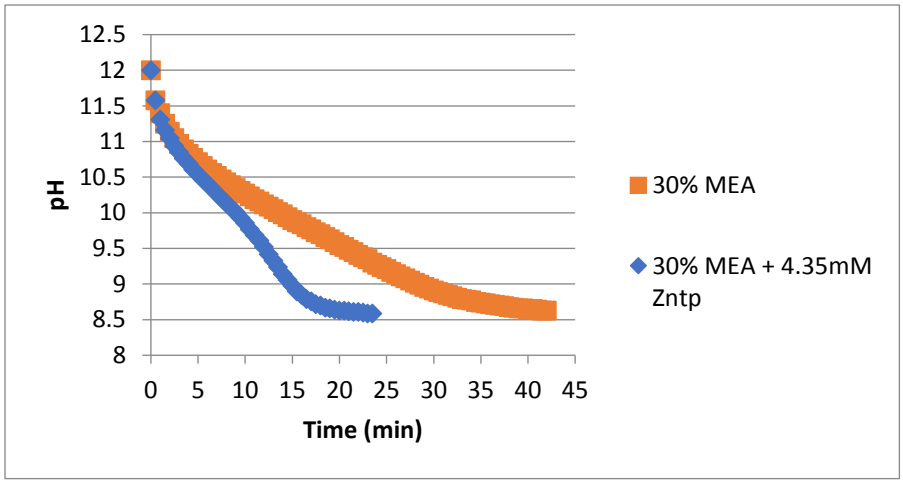

Figure 5.2 pH vs. time for zinc complex of KL^1 in 30% MEA

As seen from the graph, zinc complex of KL^1 is very catalytically active. For, 4.35 mM complex, it took approximate 25 minutes for reaction completion whereas 30 % MEA took around 45 minutes for completion. This is a very exciting result as the catalyst

is active in 30% MEA. However, during the reaction, foaming was observed. It is suggested to test this molecule in the presence of anti-foaming agent.

5.3.3 Salen Complexes

Salen-like ligand moieties have been extensively used as ligands for CO_2 activating catalysts.[170-172] Typically, salen ligands synthesized by condensation of salicylaldehyde or its derivatives with ethylenediamine or its derivatives are insoluble in water but by incorporating hydrophilic moieties such as sulphonates or carboxylates around phenol group, water-soluble salen complexes can be synthesized. For catalysis of molecules towards CO_2 capture, it is necessary that these complexes be soluble in amine or water. A major challenge we have encountered so far while synthesizing various other complexes for their efficacy towards CO_2 hydration is the insolubility of complexes in solvents. Water soluble Zn(salen)SO_3Na complex was synthesized by Dr. Rahul Butala from Dr. Atwood's lab and provided to us to test for the efficacy towards CO_2 hydration. Figure 5.3 depict catalysis by [Zn{Salen(SO_3Na)}] in 0.1 M K_2CO_3.

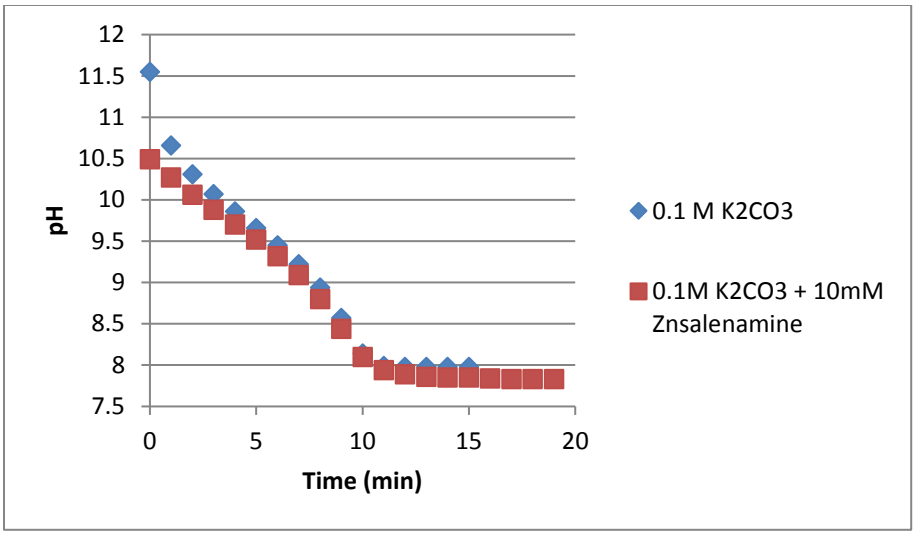

Figure 5.3 pH vs. time for [Zn{Salen(SO_3Na)}] in 0.1 M K_2CO_3

As seen from the graph, the 10.00 mM zinc [Zn{Salen(SO_3Na)}] is catalytically inactive in 0.1 M K_2CO_3. Possible reason for the inactivity is the decomposition of ligand in aqueous solution due to imine hydrolysis, making it unsuitable for aqueous amine-based post-combustion carbon capture. One of the alternatives to overcome this problem is to synthesize ligands without the presence of hydrolyzable imine groups as that should serve as promising ligand scaffolds for the synthesis of more robust CO_2 hydration catalysts. Scheme 5.3 describes one such process, where ligand salen is reduced to salean by $NaBH_4$.

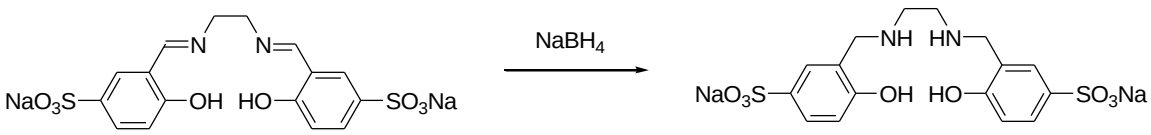

Scheme 5.3 Reduction of Salen to Salean

5.3.4 NMR-based method to monitor catalytic activity

[Zn(cyclen)] system is one of the most efficient carbonic anhydrase mimics; however, it's activity is still not comparable to benchmark carbonic anhydrase. We observed [Zn(cyclen)] complex to be even less active under conditions similar to industrial carbon capture. This is due to inhibition of catalyst due to strong coordination of anions that block the active site. This strong affinity for anion coordination inhibits bicarbonate dissociation, thereby inhibiting catalyst activity. To observe coordination of bicarbonate or solvents in which CO_2 hydration is carried out such as amines or carbonates on the active site of catalysts, we decided to develop an NMR-based method. It was hypothesized that if an alkanolamine is coordinating to the metal center either via OH or NH_2 bond present in the alkanolamine then, it is going to block the active site of the catalyst inhibiting its catalytic activity. Furthermore, oxygen in the alcohol functional group in the commonly used alkanolamines, such as MEA, could coordinate even more strongly forming a chelate. This would prevent catalytic activity by blocking the potential active site. To figure out whether amine is coordinating to the catalysts, NMR method was developed. It was hypothesized that if amine is blocking the catalyst site, then there should be difference in the NMR spectrum of catalyst after coordination with amine. There could be formation of new peaks due to coordination or there could be shift in the peaks of the original spectrum. It was also hypothesized that the equilibrium of amine

coordinating with the catalyst is dynamic and it would not be possible to see the peaks at room temperature. We should be able to see the peaks at low temperature. For that purpose, an equimolar mixture of deuterated DMSO and acetonitrile was chosen to achieve low temperature (–30 °C). New peaks started emerging proving that coordination is indeed taking place. It is difficult to prove mechanistic pathway of coordination. Scheme 5.4 below shows the coordination mode of catalyst with amine.

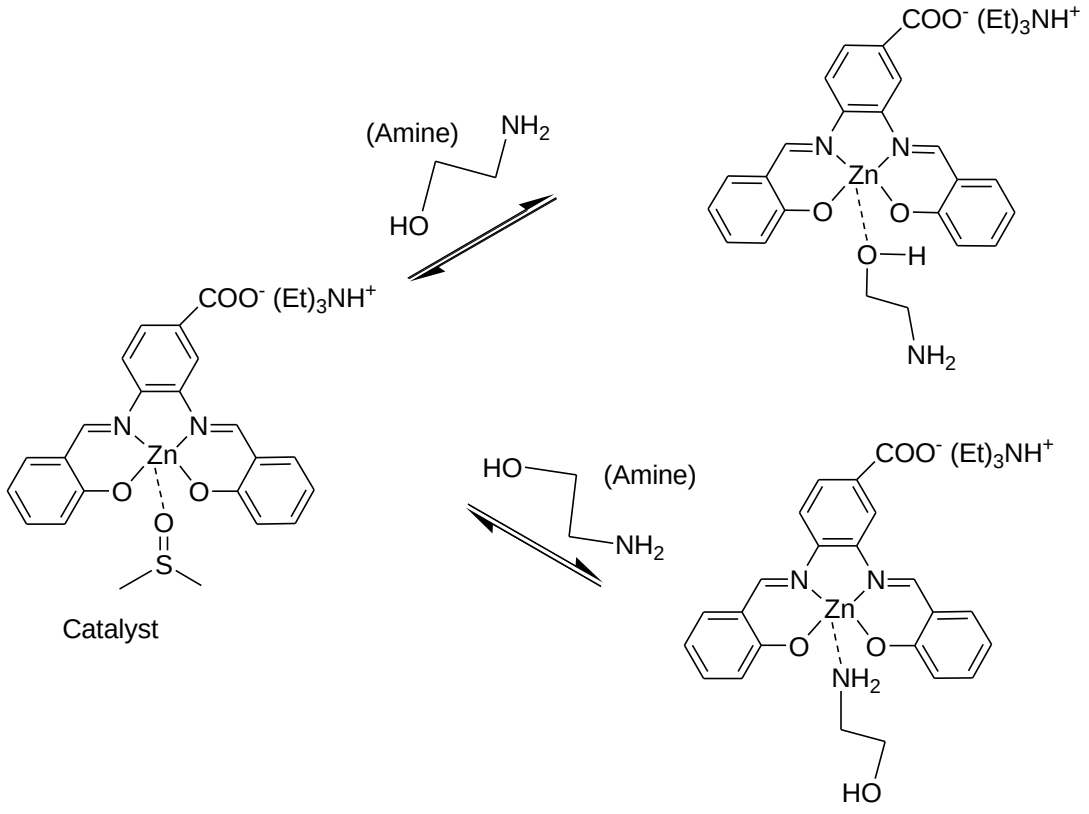

Scheme 5.4 Metal center coordination of catalyst by OH or NH_2 of monoethanolamine

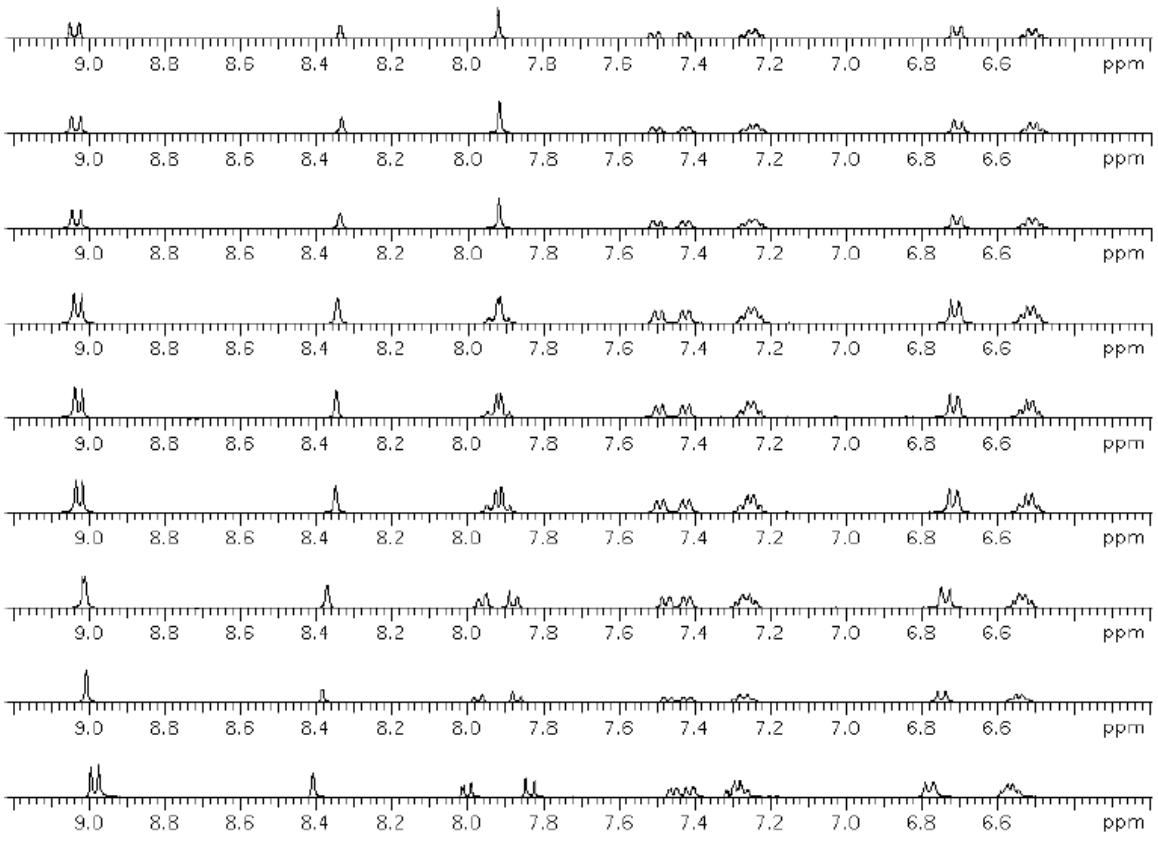

Figure 5.4 Spectrum change after addition of d_3-CD_3CN to catalyst solution in d_6-DMSO

In the ^1H NMR (figure 5.4), it can be seen that upon addition of d_3-CD_3CN, broad singlet peak at 7.9 ppm tend to show more resolved coupling reaching doublet of doublet in the final spectrum. The broad singlet at 7.9 ppm that is observed in d_6- DMSO indicates that the catalyst is fluxional in solution. Polarity of the pure d_6-DMSO system is affected by addition of acetonitrile. Similar phenomenon was also observed by Dr. Atwood *et al.,* in a similar salen complex.[173]

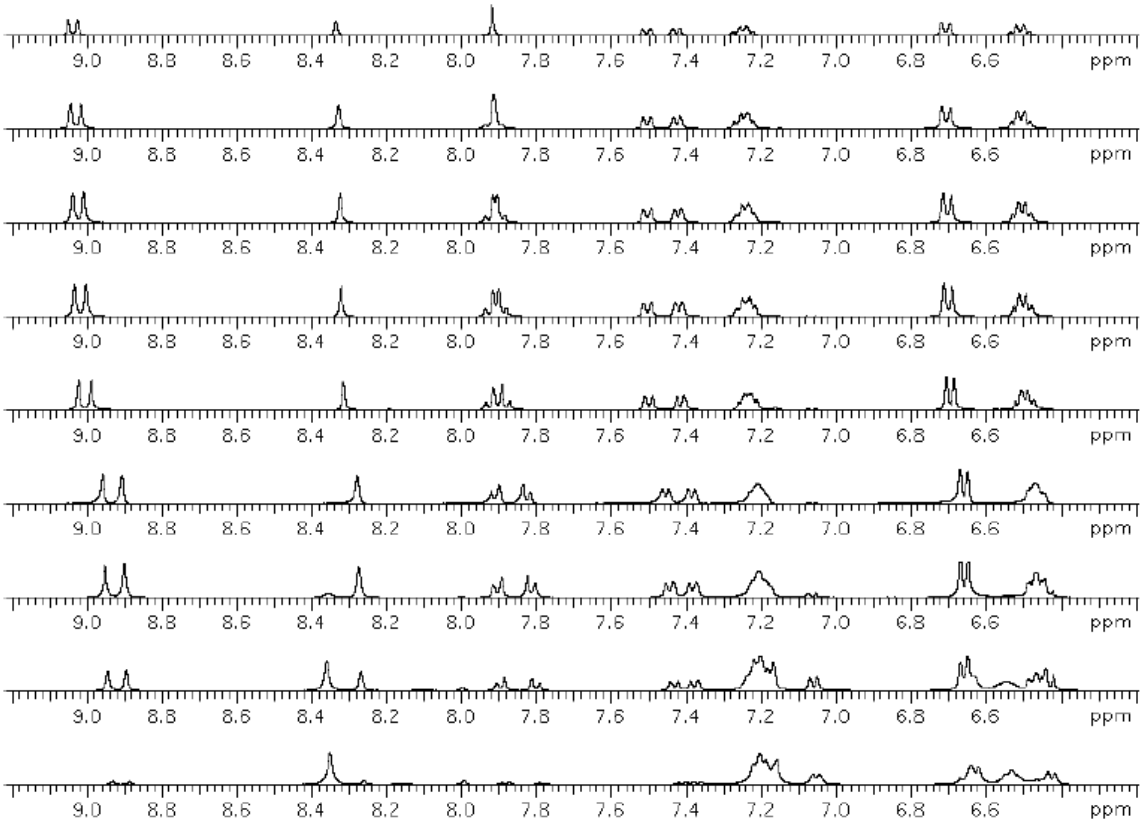

Figure 5.5 Spectrum change after addition of MEA to catalyst solution in d_6-DMSO

In the ^{1}H NMR (figure 5.5), it can be seen that initially upon addition of MEA, broad singlet peak of catalyst at 7.9 ppm tend to show more resolved coupling reaching doublet of doublet. This phenomenon is similar as observed in the previous system upon addition of d_3- CD_3CN. Upon addition of further MEA, new peaks tend to form leading the conclusion of formation of new species that are completely different from starting material thus proving that coordination is indeed taking place. It is difficult to prove mechanistic pathway of coordination.

5.4 Conclusions

The complexes containing anionic ligands that donate electron density into the metal center may serve to remove anionic bicarbonates/carbamates from the secondary coordination sphere and away from the metal center, thereby facilitating bicarbonate/anion dissociation and increasing CO_2 hydration rates. Zn complex of KL^1 was found to be catalytically active; this compound should be tested in presence of anti-foaming agent. 1:1 Zn complex of an N,N-pincer ligand couldn't be isolated despite various attempts. Optimization of purification method to isolate the complex for full characterization needs to be done in the future. An NMR-based method was successfully developed to see if the coordination of solvents to CO_2 capture solvents can be studied.

Chapter 6 Summary and Future Directions

Work undertaken so far, and possible future development in ferrocene-fused thiophene complexes, and homogeneous catalysts for CO_2 capture are discussed below.

Chapter 1 discussed approaches to ferrocene-fused thiophene complexes. Exploring a shorter synthetic route to 1,2-bis(hydroxymethyl)ferrocene was the first task. This was followed by successful synthesis of an important precursor to ferroceno[*c*]thiophene, 1,4-dihydro-2,3-ferrocenodithiin. The desired end product, ferrocene–fused thiophene monomer, hasn't been obtained yet. Further optimization of synthetic pathway to the target molecule is needed. Investigation into polymerization (electrochemical and chemical) is the next logical step once the monomer (aromatic or quinoid form) is achieved. Future work will also involve study of electronic and electrochromic properties and changing other conjugated substituents to obtain different forms of metallocene-fused thiophene polymer. Substituent effect with electron-withdrawing functionalities on ferroceno[*c*]thiophene is an intriguing avenue for further research.

Chapter 2 discussed the latest advancements in the area of Carbon capture and Storage.

Chapter 3 focused on synthesis and catalysis of homogeneous catalysts for CO_2 capture. We focused mainly on the synthesis and characterization of Cu, Co, and Zn

complexes with ligands, 1,5,7,7,12,14,14-hexamethyl-1,4,8,11-tetraazacyclotetradecane (teta, tetb), 1,4,7,10-tetraazacyclododecane (cyclen), tris(2-benzimidazoylmethyl)amine (NTB), and nitrilotris(2-benzimidazoylmethyl-6-sulfonic acid) (NTBSA) as these complexes have similar structural, thermodynamic and kinetic properties to carbonic anhydrase. We tested these molecules in a wetted-wall column experiment. None of the compounds were found to be catalytically active in the conditions conducive to post carbon capture. It was proposed that the lack of activity may be related to coordination of the solvent to the metal. A laboratory setup was designed to reduce the screening time of catalysts for CO_2 capture. Using a decrease in pH over time method a series of catalysts was tested. Compared to the WWC method, lower catalyst quantity and only a few hours of evaluation time are required. This further save time since the smaller amount of catalyst needed reduces time spent synthesizing complexes.

Chapter 4 discussed catalysis by [Zn(cyclen)(H_2O)]•2H_2O**.** This complex showed a reasonable k_{cat} of 2000 L/mol that was consistent with previous literature reported results using stopped-flow spectrometry kinetics testing. However, the activity was much lower when evaluated in conditions more consistent with CO_2 capture reaction (CAER pH drop screening). The rate constant is lower than what was expected from the stopped-flow measurements, probably because of bicarbonate coordination to Zn active site in these systems causing inability to reform hydroxyl species on the metal. The Zn center is

highly electron deficient and therefore easily coordinates anions, inhibiting the ability to reform hydroxyl species on the metal. The cationic complex attracts anionic species such as bicarbonate into its secondary coordination sphere to maintain charge balance which drives the equilibrium to the bicarbonate-bound species. Thus, it became necessary to test the catalysis of benchmark enzyme carbonic anhydrase under similar conditions to determine the threshold k_{obs} value. Carbonic anhydrases catalyze the hydration of carbon dioxide at ambient temperatures and physiological pH with the highest known rate constant = 10^6 M^{-1} s^{-1}, but in our system (CAER pH drop screening) k_{obs} came out to be 438797 M^{-1} s^{-1}. The lower catalytic rate constant for carbonic anhydrase in 0.1000 M, similar to Zn-cyclen, strengthens the conjecture that at high bicarbonate concentrations, HCO_3^- binding to the Zn(II) active site slows catalysis by inhibiting bicarbonate displacement with water to regenerate the active species. Therefore, routes for circumventing inhibition of carbon capture catalysts are broadly required.

Chapter 5 discussed catalytic activity of various anionic complexes. The complexes containing anionic ligands that donate electron density into the metal center may serve to remove anionic bicarbonates/carbamates from the secondary coordination sphere and away from the metal center, thereby facilitating bicarbonate/anion dissociation and increasing CO_2 hydration rates. Trispyrazolylborates were found to be catalytically active; these compounds should be tested in presence of anti-foaming agent.

1:1 Zn complex of an N,N-pincer ligand couldn't be isolated despite various attempts. Optimization of purification method to isolate the complex for full characterization needs to be done in the future. An NMR-based method was developed to see if the coordination of solvents to CO_2 capture solvents can be studied. We propose that trisimidazole moieties should be synthesized and tested for catalytic activity.

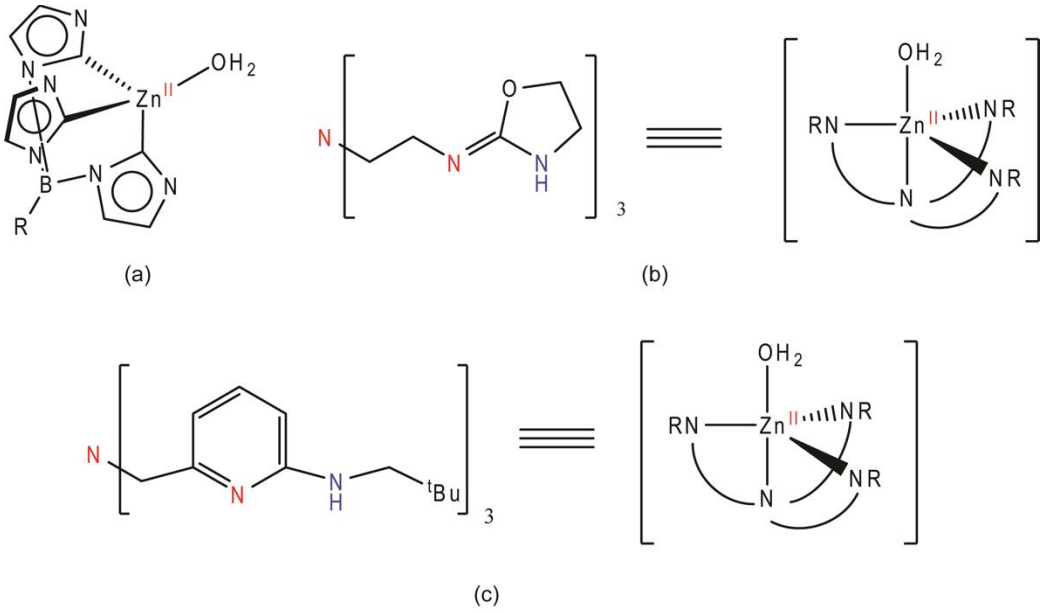

Figure 6.1 New target candidates featuring (a) a tethered-tetrahedral, two tripodal networks containing a (b) tautomerized H-bond network, and (c) sterically demanding and rigid H-bond network.

We predict that metal complexes of the trisimidazole ligand should be catalytically active based on three criteria: 1) Geometry: the tris(carbene) ligand coordinates in a tetrahedral geometry allowing access to both the metal center and hydroxo ligand for CO_2 hydration. 2) Sterics: The imidazole functionality can be

sufficiently functionalized to form a bulky environment to prevent dimerization and/or bidentate coordination of carbonates. 3) Electronics: The carbenes are strong sigma donors that should elongate the Zn–OH bond, making it more reactive towards CO_2 as well as facilitating dissociation of newly formed carbonates to regenerate the active species. The ligand design shown in Figure 6.1 was developed to overcome the problems contained in the Zn-cyclen system. The ligand scaffold in Figure 1a should provide a strong pseudo-trans-effect, thereby elongating the Zn–OH bond generating a more reactive hydroxo, disfavoring unwanted coordination, and promoting dissociation of newly formed carbonates derived from CO_2. The ligand scaffold in Figure 1b and 1c both contain an H-bonding network in the 2^{nd} coordination sphere that should aid the dissociation of carbonates as well as being significantly sterically hindered inhibiting dimerization. The ligand scaffold design in Figure 1 can be placed into two categories: 1) facially-capping tethered tetrahedral and 2) Hydrogen-bonding tripodal network. The above scaffolds have beneficial qualities that led to their selection as catalyst candidates. The scaffold in category two were chosen based on 3 criteria as well. 1) Geometry: Ligands in category 2 generate tripodal complexes consisting of trigonal bipyramidal geometry. This geometry still allows for activation of CO_2 while inhibiting bidentate coordination of carbonates. 2) Sterics: As with category 1, the sterics should inhibit complex dimerization. 3) Hydrogen-Bonding Network: Ligands in category 2 contain

functionalities that allow for development of a hydrogen bonding network in the 2nd coordination sphere. This should help dissociate carbonate species and regenerate the active catalyst for CO_2 hydration.

To date, there are no homogeneous catalysts that are being used in CO_2 capture plants to increase the rate of CO_2 absorption, and hence this project has a vast scope of further development.

References

1. Wudl, F.; Kobayashi, M.; Heeger, A. J., *J. Org. Chem.* **1984,** *49*, 3382.

2. Kanatzidis, M. G., *Chem. Eng. News. Arch.* **1990,** *68*, 36.

3. Heywang, G.; Jonas, F., *Adv. Mater.* **1992,** *4*, 116.

4. Brédas, J. L.; Heeger, A. J.; Wudl, F., *J. Chem. Phys.* **1986,** *85*, 4673.

5. Roncali, J., *Chem. Rev.* **1997,** *97*, 173.

6. McCullough, R. D., *Adv. Mater.* **1998,** *10*, 93.

7. Kim, D.; Jeong, S.; Lee, S. H.; Moon, J.; Song, J. K., *Synth. Met.* **2009,** *159*, 1381.

8. Kline, R. J.; DeLongchamp, D. M.; Fischer, D. A.; Lin, E. K.; Richter, L. J.; Chabinyc, M. L.; Toney, M. F.; Heeney, M.; McCulloch, I., *Macromolecules* **2007,** *40*, 7960.

9. Williams, K. A.; Boydston, A. J.; Bielawski, C. W., *Chem. Soc. Rev.* **2007,** *36*, 729.

10. Wolf, M. O., Synthesis and Properties of Oligo- and Polythiophenes Containing Transition Metals. In *Handbook of Thiophene-Based Materials*, John Wiley & Sons, Ltd: 2009; pp 293.

11. Snyder, C. A.; Selegue, J. P.; Tice, N. C.; Wallace, C. E.; Blankenbuehler, M. T.; Parkin, S.; Allen, K. D. E.; Beck, R. T., *J. Am. Chem. Soc.* **2005,** *127*, 15010.

12. Selegue, J. P.; Swarat, K. A., *J. Am. Chem. Soc.* **1993,** *115*, 6448.

13. Snyder, C. A.; Tice, N. C.; Sriramula, P. G.; Neathery, J. L.; Mobley, J. K.; Phillips, C. L.; Preston, A. Z.; Strain, J. M.; Vanover, E. S.; Starling, M. P.; Sahi, N. V., *Synth. Commun.* **2011,** *41*, 1357.

14. Wallace, C. E.; Selegue, J. P.; Carrillo, A., *Organometallics* **1998,** *17*, 3390.

15. Snyder, C. A.; Tice, N. C.; Maddox, J. B.; Emberton, E. D.; Vanover, E. S.; Hinson, D. F.; Jackson, D. C., *J. Organomet. Chem.* **2011,** *696*, 2220.

16. Tice, N. C. The Synthesis, Structure, And Reactivity Of Some Organomettalic-Fused Heterocycles. P.hD. Dissertation, University of Kentucky, Lexington, KY, 2006.

17. Lednicer, D. H., C. R., *Organic Syntheses* 1973, p 434.

18. Slocum, D. W.; Rockett, B. W.; Hauser, C. R., *J. Am. Chem. Soc.* **1965,** *87*, 1241.

19. Marr, G.; Rockett, B. W.; Rushworth, A., *J. Organomet. Chem.* **1969,** *16*, 141.

20. Otwinowski, Z.; Minor, W., *Methods Enzymol.* **1997,** *276*, 307.

21. Sheldrick, G., *Acta Cryst. A* **2008,** *64*, 112.

22. Angelici, R. J., *Acc. Chem. Res.* **1988,** *21*, 387.

23. Jr, K. J. R.; Jr, R. J. C.; Sokol, P. E., *J. Am. Chem. Soc.* **1957,** *79*, 3420.

24. Rinehart, K. L.; Curby, R. J., *J. Am. Chem. Soc.* **1957,** *79*, 3290.

25. Gao, B.; Yang, B.; Li, T.; Zhang, B., *Synth. Commun.* **2009,** *39*, 2973.

26. Sotiriou, C.; Lee, W.; Giese, R. W., *J. Org. Chem.* **1990,** *55*, 2159.

27. Maier, N. A.; Shklyar, S. A.; Ol'dekop, Y. A., *Zh. Obshch. Khim.* **1980,** *50*, 2625.

28. Ratajczak, A., *Pol. J. Chem.* **1981,** *51*, 1953.

29. Boev, V. I. D., A. V., *Russ. J. Gen. Chem.* **1985,** *54*, 1660.

30. Hillman, M.; Austin, J. D., *Organometallics* **1987,** *6*, 1737.

31. Ratajczak, A.; Niedbałła, H., *Pol. J. Chem.* **2001,** *75*, 677.

32. Tverdokhlebov, V. P. S., A. V.; Tselinskii, I. V. Zh. Org. Khim. 1982, 18, 1958, *Russ. J. Org. Chem.* **1982,** *18*, 1958.

33. Banks, S. R. Organometallic Materials: Ferroceno[c]thiophenes and 1,2-Bisthienylmetallocenes, P.hD. Dissertation, University of Kentucky, Lexington, KY, 2016.

34. Southam, G.; Rothschild, L. J.; Westall, F., The Geology and Habitability of Terrestrial Planets: Fundamental Requirements for Life. In *Geology and Habitability of Terrestrial Planets*, Fishbaugh, K. E.; Lognonné, P.; Raulin, F.; Des Marais, D. J.; Korablev, O., Eds. Springer New York: New York, NY, 2007; pp 7.

35. Jaime, L. G.; Aguilar, L.; Pichardo, B., *Mon. Not. R. Astron. Soc.* **2014,** *443*, 260.

36. Lacis, A. A.; Schmidt, G. A.; Rind, D.; Ruedy, R. A., *Science* **2010,** *330*, 356.

37. Charles, D. K., The Concentration and Isotopic Abundances of Carbon Dioxide in the Atmosphere. Ocenaography, S. I. O., Ed. University of California San Deigo, 1960.

38. Carbon Cycle Gases; Earth System Research Laboratory: Mauna Loa, Oct 15, 2017, MLO Carbon Cycle Surface Flasks.

39. NASA https://climate.nasa.gov/climate_resources/24/ (accessesed Oct 15, 2017).

40. Pachauri, R. K., Meyer, L., *Climate change 2014: Synthesis Report;* IPCC, Geneva, Switzerland, 2015.

41. Lockwood, M., *Proc. Math. Phys. Eng. Sci.* **2009,** *466*, 303.

42. Lean, J. L., *Wiley. Interdiscip. Rev. Clim. Change.* **2010,** *1*, 111.

43. NOAA http://www.cpc.ncep.noaa.gov/products/stratosphere/temperature/ (accessed Oct 15, 2017).

44. NASA Global Temperature. https://climate.nasa.gov/vital-signs/global-temperature/ (accessed Oct 15, 2017).

45. NASA Goddard Institute of Space Studies. https://data.giss.nasa.gov/gistemp/graphs/ (accessed Oct 15, 2017).

46. Hansen, J.; Ruedy, R.; Sato, M.; Lo, K., *Rev. Geophys.* **2010,** *48*, RG4004.

47. Boden, T. A., G. Marland, R. J. Andres, Global, Regional, and National Fossil-Fuel CO2 Emissions. Center, C. D. I. A., Ed. U.S. Department of Energy, Oak Ridge, Tenn., U.S.A. : Oak Ridge National Laboratory, 2017.

48. Agency, E. P., Inventory of U.S. Greenhouse Gas Emissions and Sinks: 1990-2015. EPA, Ed. 2017; p 633.

49. Melillo, J. M., Terese (T.C.) Richmond, and Gary W. Yohe, Eds., Climate Change Impacts in the United States: The Third National Climate Assessment. Program, U. S. G. C. R., Ed. 2014; p 841.

50. Puma, M. J.; Cook, B. I., *J. Geophys. Res.* **2010,** *115*, D16120.

51. Administration, E. I. Electricity in the United States. https://www.eia.gov/energyexplained/index.cfm?page=electricity_in_the_united_states - tab2 (accessed Oct 16, 2017).

52. Fanchi, J. R., *Energy in the 21st century*. 4th edition. ed.; Singapore: World Scientific: 2017.

53. Mcculloch, S., Keeling, S. *20 Years of Carbon Capture and Storage.* International Energy Agency, Paris, France, 2016.

54. Abanades, J. C.; Arias, B.; Lyngfelt, A.; Mattisson, T.; Wiley, D. E.; Li, H.; Ho, M. T.; Mangano, E.; Brandani, S., *Int. J. Greenh. Gas Control* **2015,** *40*, 126.

55. Metz, B., O. Davidson, H. C. De Coninck, M. Loos, and L. A. Meyer, IPCC Special Report on Carbon Dioxide Capture and Storage. Cambridge, UK/New York: Cambridge Univ. Press: 2005; Vol. I, p 443.

56. Metz, B.; O.Davidson; H. C. de Coninck; M. Loos, a.; Meyer, L. A., **2005**, 442.

57. Jansen, D.; Gazzani, M.; Manzolini, G.; Dijk, E. v.; Carbo, M., *Int. J. Greenh. Gas Control* **2015,** *40*, 167.

58. Puigjaner, L., Introduction. In *Syngas from Waste: Emerging Technologies*, Puigjaner, L., Ed. Springer London: London, 2011; pp 1.

59. Syngas Composition. https://www.netl.doe.gov/research/coal/energy-systems/gasification/gasifipedia/syngas-composition (accessed Oct 16, 2017).

60. Higman, C.; van der Burgt, M., Chapter 1 - Introduction. In *Gasification (Second Edition)*, Gulf Professional Publishing: Burlington, 2008; pp 1.

61. Higman, C.; van der Burgt, M., Chapter 2 - The Thermodynamics of Gasification. In *Gasification (Second Edition)*, Gulf Professional Publishing: Burlington, 2008; pp 11.

62. Higman, C.; van der Burgt, M., Chapter 3 - The Kinetics of Gasification and Reactor Theory. In *Gasification (Second Edition)*, Gulf Professional Publishing: Burlington, 2008; pp 33.

63. Higman, C.; van der Burgt, M., Chapter 4 - Feedstocks and Feedstock Characteristics. In *Gasification (Second Edition)*, Gulf Professional Publishing: Burlington, 2008; pp 47.

64. Higman, C.; van der Burgt, M., Chapter 5 - Gasification Processes. In *Gasification (Second Edition)*, Gulf Professional Publishing: Burlington, 2008; pp 91.

65. Higman, C.; van der Burgt, M., Chapter 6 - Practical Issues. In *Gasification (Second Edition)*, Gulf Professional Publishing: Burlington, 2008; pp 193.

66. Stanger, R.; Wall, T.; Spörl, R.; Paneru, M.; Grathwohl, S.; Weidmann, M.; Scheffknecht, G.; McDonald, D.; Myöhänen, K.; Ritvanen, J.; Rahiala, S.; Hyppänen, T.; Mletzko, J.; Kather, A.; Santos, S., *Int. J. Greenh. Gas Control* **2015,** *40*, 55.

67. Xu, X.; Song, C.; Wincek, R.; M Andresen, J.; G Miller, B.; W Scaroni, A., *Fuel Chem. Div. Preprints*, **2003,** *48*, 162.

68. Granite, E. J.; King, W. P.; Stanko, D. C.; Pennline, H. W., *Main Group Chem.* **2008,** *7*, 227.

69. Deschermeier, R.; Rehfeldt, S.; Klein, H., *Chem. Eng. Technol.* **2017,** *40*, 28.

70. Ban, Z. H., *Adv. Mat. Res.* **2014,** *917*, 134.

71. Oko, E.; Wang, M.; Joel, A. S., *Int. J. Coal. Sci. Technol.* **2017**, *4*,5.

72. Power, S. http://www.saskpower.com/our-power-future/carbon-capture-and-storage/carbon-storage-research-centre/?linkid=MM_carbon_capture_research_centre (accessed Oct 16, 2017).

73. Cebrucean, D.; Cebrucean, V.; Ionel, I., *Energy Procedia* **2014,** *63*, 18.

74. Oexmann, J.; Kather, A.; Linnenberg, S.; Liebenthal, U., *Greenh. Gases.* **2012,** *2*, 80.

75. Soong, Y.; Gray, M. L.; Champagne, K. J.; Stevens, R. W.; Toochinda, P.; Chuang, S. S. C., Novel Solid Sorbents for Carbon Dioxide Capture. In *Environmental Challenges and Greenhouse Gas Control for Fossil Fuel Utilization in the 21st Century*, Maroto-Valer, M. M.; Song, C.; Soong, Y., Eds. Springer US: Boston, MA, 2002; pp 147.

76. Dąbrowski, A.; Bülow, M.; Hubicki, Z.; Robens, E., Novel Environmental Sorbents and Methods for their Characterization. In *Role of Interfaces in Environmental Protection*, Barany, S., Ed. Springer Netherlands: Dordrecht, 2003; pp 225.

77. Vericella, J. J.; Baker, S. E.; Stolaroff, J. K.; Duoss, E. B.; Hardin Iv, J. O.; Lewicki, J.; Glogowski, E.; Floyd, W. C.; Valdez, C. A.; Smith, W. L.; Satcher Jr, J. H.; Bourcier, W. L.; Spadaccini, C. M.; Lewis, J. A.; Aines, R. D., **2015,** *6*, 6124.

78. Tachy, E. D., C. S. J. Andrade, and B. S. Neves, *AMM.* **2016,** *830*, 19.

79. Kim, I.; Hoff, K. A.; Mejdell, T., *Energy Procedia* **2014,** *63*, 1446.

80. Choma, J.; Stachurska, K.; Marszewski, M.; Jaroniec, M., *Adsorption* **2016,** *22*, 581.

81. Kohl, A. L.; Nielsen, R. B., Chapter 2 - Alkanolamines for Hydrogen Sulfide and Carbon Dioxide Removal. In *Gas Purification (Fifth Edition)*, Gulf Professional Publishing: Houston, 1997; pp 40.

82. D'Alessandro, D. M.; Smit, B.; Long, J. R., *Angew. Chem. Int. Ed.* **2010,** *49*, 6058.

83. Rochelle, G. T., *Science* **2009,** *325*, 1652.

84. Rao, A. B.; Rubin, E. S., *Environ. Sci. Technol.* **2002,** *36*, 4467.

85. Sharma, M. M.; Danckwerts, P. V., *Trans. Faraday Soc.* **1963,** *59*, 386.

86. Danckwerts, P. V., *Gas-liquid reactions*. New York, McGraw-Hill Book Co.: New York, 1970.

87. Vázquez, G.; Chenlo, F.; Pereira, G., *Ind. Eng. Chem. Res.* **1997,** *36*, 2353.

88. Wappel, D.; Khan, A.; Shallcross, D.; Joswig, S.; Kentish, S.; Stevens, G., *Energy Procedia* **2009,** *1*, 125.

89. Oexmann, J.; Hensel, C.; Kather, A., *Int. J. Greenh. Gas Control* **2008,** *2*, 539.

90. Cullinane, J. T.; Rochelle, G. T., *Ind. Eng. Chem. Res.* **2006,** *45*, 2531.

91. Trachtenberg, M. C. B., L. In *CO2 Capture: Enzyme vs. Amine*, Fourth Annual Conference on Carbon Capture and Sequestration, Alexandria, VA, DOE/NETL: Alexandria, VA, 2005; pp 2.

92. Vaidya, P. D.; Kenig, E. Y., *Chem. Eng. Technol.* **2007,** *30*, 1467.

93. Luis, P., *Desalination* **2016,** *380*, 93.

94. Aines, R. D.; Spaddaccini, C. M.; Duoss, E. B.; Stolaroff, J. K.; Vericella, J.; Lewis, J. A.; Farthing, G., *Energy Procedia* **2013,** *37*, 219.

95. Yu, C.-H.; Huang, C.-H.; Tan, C.-S., *AAQR* **2012,** *12*, 745.

96. Feron, P. H. M., *Int. J. Greenh. Gas Control* **2010,** *4*, 152.

97. Zhang, X.; Van Eldik, R., *Inorg. Chem.* **1995,** *34*, 5606.

98. Enns, T., *Science* **1967,** *155*, 44.

99. DeVoe, H.; Kistiakowsky, G. B., *J. Am. Chem. Soc.* **1961,** *83*, 274.

100. Tsao, G. T., *Chem. Eng. Sci.* **1972,** *27*, 1593.

101. Alper, E., *Chem. Eng. Sci.* **1978,** *33*, 1399.

102. Alper, E.; Deckwer, W. D., *Chem. Eng. Sci.* **1980,** *35*, 549.

103. Donaldson, T. L., *Chem. Eng. Sci.* **1978,** *33*, 627.

104. Liu, N.; Bond, G. M.; Abel, A.; McPherson, B. J.; Stringer, J., *Fuel Process. Technol.* **2005,** *86*, 1615.

105. Bond, G. M.; Stringer, J.; Brandvold, D. K.; Simsek, F. A.; Medina, M.-G.; Egeland, G., *Energy Fuels* **2001,** *15*, 309.

106. Dilmore, R.; Griffith, C.; Liu, Z.; Soong, Y.; Hedges, S. W.; Koepsel, R.; Ataai, M., *Int. J. Greenh. Gas Control* **2009,** *3*, 401.

107. Fradette, S.; Ceperkovic, O., CO2 absorption solution. U.S. Patent 7,740,689 B2, June 22, 2010.

108. Xia, J.; Shi, Y.-b.; Zhang, Y.; Miao, Q.; Tang, W., *Inorg. Chem.* **2003,** *42*, 70.

109. Hay, R. W.; Lawrance, G. A.; Curtis, N. F., *J. Chem. Soc., Perkin Trans. 1* **1975**, 591.

110. Athey, P. S.; Kiefer, G. E., *J. Org. Chem.* **2002,** *67*, 4081.

111. Ki-Young, C.; Il-Hwan, S.; Ju Chang, K., *Polyhedron* **1997,** *16*, 1783.

112. Choi, K.-Y.; Ryu, H.; Suh, I.-H., *Polyhedron* **1998,** *17*, 1241.

113. Nakata, K.; Shimomura, N.; Shiina, N.; Izumi, M.; Ichikawa, K.; Shiro, M., *J. Inorg. Biochem.* **2002,** *89*, 255.

114. Liu, J.; Wang, S.; Zhao, B.; Tong, H.; Chen, C., *Energy Procedia* **2009,** *1*, 933.

115. Mshewa, M. M. Carbon Dioxide Desorption/absorption with Aqueous Mixtures of Methyldiethanolamine and Diethanolamine at 40 to 120 Degrees C. Ph.D. Dissertation, The University of Texas at Austin, Austin, TX, 1995.

116. Vespa, M., *Ecol. Law. Curr.* 2009, p 185.

117. Vahrenkamp, H., *Acc. Chem. Res.* **1999,** *32*, 589.

118. Zhang, X.; van Eldik, R., *Inorg. Chem.* **1995,** *34*, 5606.

119. Davy, R., *Energy Procedia* **2009,** *1*, 885.

120. Liu, K.; Jinka, K. M.; Remias, J. E.; Liu, K., *Ind. Eng. Chem. Res.* **2013,** *52*, 15932.

121. Thompson, L. K.; Ramaswamy, B. S.; Seymour, E. A., *Can. J. Chem.* **1977,** *55*, 878.

122. Wishrojwar, A. S. Synthesis, Characterization and Development of Catalysts for CO_2 Capture. M.S. thesis, University of Kentucky, Lexington, KY, 2010.

123. Zhang, X.; van Eldik, R.; Koike, T.; Kimura, E., *Inorg. Chem.* **1993,** *32*, 5749.

124. Kimura, E.; Shiota, T.; Koike, T.; Shiro, M.; Kodama, M., *J. Am. Chem. Soc.* **1990,** *112*, 5805.

125. Kimura, E., Macrocyclic Polyamine Zinc(II) Complexes as Advanced Models for Zinc(II) Enzymes. In *Prog. Inorg. Chem.*, John Wiley & Sons, Inc.: 2007; pp 443.

126. Carbonic Anhydrase Models. *Encyclopedia of Supramolecular Chemistry* [Online]; CRC Press, Posted May 05, 2004. https://www.taylorfrancis.com/books/e/9781482258165 (accessed July 28, 2017).

127. Ichikawa, K.; Nakata, K.; Ibrahim, M. M.; Kawabata, S., *Stud. Surf. Sci. Catal.* **1998,** *114*, 309.

128. Lavecchia, R.; Zugaro, M., *Fed. Eur. Biochem. Soc.* **1991,** *292*, 162.

129. Matulis, D.; Kranz, J. K.; Salemme, F. R.; Todd, M. J., *Biochemistry* **2005,** *44*, 5258.

130. Subat, M.; Woinaroschy, K.; Gerstl, C.; Sarkar, B.; Kaim, W.; König, B., *Inorg. Chem.* **2008,** *47*, 4661.

131. Looney, A.; Han, R.; McNeill, K.; Parkin, G., *J. Am. Chem. Soc.* **1993,** *115*, 4690.

132. Cheng, M.; Lobkovsky, E. B.; Coates, G. W., *J. Am. Chem. Soc.* **1998,** *120*, 11018.

133. Baffert, M.; Maishal, T. K.; Mathey, L.; Copéret , C.; Thieuleux, C., *ChemSusChem* **2011,** *4*, 1762.

134. Koziol, L.; Valdez, C. A.; Baker, S. E.; Lau, E. Y.; Floyd, W. C.; Wong, S. E.; Satcher, J. H.; Lightstone, F. C.; Aines, R. D., *Inorg. Chem.* **2012,** *51*, 6803.

135. Gibbons, B. H.; Edsall, J. T., *J. Biol. Chem.* **1964,** *239*, 2539.

136. Versteeg, G. F.; Van Swaaij, W. P. M., *J. Chem. Eng. Data* **1988,** *33*, 29.

137. Merz, K. M.; Hoffmann, R.; Dewar, M. J. S., *J. Am. Chem. Soc.* **1989,** *111*, 5636.

138. Krishnamurthy, V. M.; Kaufman, G. K.; Urbach, A. R.; Gitlin, I.; Gudiksen, K. L.; Weibel, D. B.; Whitesides, G. M., *Chem. Rev.* **2008,** *108*, 946.

139. Eriksson, A. E.; Jones, T. A.; Liljas, A., *Proteins: Struct., Funct., Bioinf.* **1988,** *4*, 274.

140. Floyd, W. C.; Baker, S. E.; Valdez, C. A.; Stolaroff, J. K.; Bearinger, J. P.; Satcher, J. H.; Aines, R. D., *Environ. Sci. Technol.* **2013,** *47*, 10049.

141. Ryss, I. G., *Zh. Fiz. Khim.* **1947,** *21*, 197.

142. Martell, A. E.; Hancock, R. D.; Motekaitis, R. J., *Coord. Chem. Rev.* **1994,** *133*, 39.

143. Khalifah, R. G., *J. Biol. Chem.* **1971,** *246*, 2561.

144. Nishimori, I.; Minakuchi, T.; Onishi, S.; Vullo, D.; Cecchi, A.; Scozzafava, A.; Supuran, C. T., *J. Enzym. Inhib. Med. Ch.* **2009,** *24*, 70.

145. De Simone, G.; Supuran, C. T., *J. Inorg. Biochem.* **2012,** *111*, 117.

146. Lippert, C. A.; Liu, K.; Sarma, M.; Parkin, S. R.; Remias, J. E.; Brandewie, C. M.; Odom, S. A.; Liu, K., *Catal. Sci. Technol.* **2014,** *4*, 3620.

147. Pérez Olmo, C.; Böhmerle, K.; Steinfeld, G.; Vahrenkamp, H., *Eur. J. Inorg. Chem.* **2006,** *2006*, 3869.

148. Singh, B.; Lesher, G. Y.; Pluncket, K. C.; Pagani, E. D.; Bode, D. C.; Bentley, R. G.; Connell, M. J.; Hamel, L. T.; Silver, P. J., *J. Med. Chem.* **1992,** *35*, 4858.

149. Huang, D.; Holm, R. H., *J. Am. Chem. Soc.* **2010,** *132*, 4693.

150. Huang, D.; Makhlynets, O. V.; Tan, L. L.; Lee, S. C.; Rybak-Akimova, E. V.; Holm, R. H., *Inorg. Chem.* **2011,** *50*, 10070.

151. Huang, D.; Makhlynets, O. V.; Tan, L. L.; Lee, S. C.; Rybak-Akimova, E. V.; Holm, R. H., *Proc. Natl. Acad. Sci. U.S.A.* **2011,** *108*, 1222.

152. Benkmil, B.; Ji, M.; Vahrenkamp, H., *Inorg. Chem.* **2004,** *43*, 8212.

153. Gregorzik, R.; Hartmann, U.; Vahrenkamp, H., *Chem. Ber.* **1994,** *127*, 2117.

154. Tekeste, T.; Vahrenkamp, H., *Inorg. Chim. Acta* **2007,** *360*, 1523.

155. Tekeste, T.; Vahrenkamp, H., *Eur. J. Inorg. Chem.* **2006,** *2006*, 5158.

156. Tekeste, T.; Vahrenkamp, H., *Inorg. Chem.* **2006,** *45*, 10799.

157. Maldonado Calvo, J. A.; Vahrenkamp, H., *Inorg. Chim. Acta* **2006,** *359*, 4079.

158. Brandsch, T.; Schell, F.-A.; Weis, K.; Ruf, M.; Miiller, B.; Vahrenkamp, H., *Chem. Ber.* **1997,** *130*, 283.

159. Brombacher, H.; Vahrenkamp, H., *Inorg. Chem.* **2004,** *43*, 6042.

160. Badura, D.; Vahrenkamp, H., *Inorg. Chem.* **2002,** *41*, 6013.

161. Badura, D.; Vahrenkamp, H., *Inorg. Chem.* **2002,** *41*, 6020.

162. Badura, D.; Vahrenkamp, H., *Eur. J. Inorg. Chem.* **2003,** *2003*, 3723.

163. Gross, F.; Vahrenkamp, H., *Inorg. Chem.* **2005,** *44*, 4433.

164. Rombach, M.; Seebacher, J.; Ji, M.; Zhang, G.; He, G.; Ibrahim, M. M.; Benkmil, B.; Vahrenkamp, H., *Inorg. Chem.* **2006,** *45*, 4571.

165. Vahrenkamp, H., *Dalton Trans.* **2007**, 4751.

166. Pérez Olmo, C.; Böhmerle, K.; Vahrenkamp, H., *Inorg. Chim. Acta* **2007,** *360*, 1510.

167. Ji, M.; Vahrenkamp, H., *Eur. J. Inorg. Chem.* **2005,** *2005*, 1398.

168. Groß, F.; Brombacher, H.; Vahrenkamp, H., *Z. Anorg. Allg. Chem.* **2007,** *633*, 865.

169. Ruf, M.; Vahrenkamp, H., *Inorg. Chem.* **1996,** *35*, 6571.

170. Anselmo, D.; Escudero-Adán, E. C.; Martínez Belmonte, M.; Kleij, A. W., *Eur. J. Inorg. Chem.* **2012,** *2012*, 4694.

171. Bhunia, S.; Molla, R. A.; Kumari, V.; Islam, S. M.; Bhaumik, A., *Chem. Commun.* **2015,** *51*, 15732.

172. Liu, T.-T.; Liang, J.; Huang, Y.-B.; Cao, R., *Chem. Commun.* **2016,** *52*, 13288.

173. Atwood, D. A.; Benson, J.; Jegier, J. A.; Lindholm, N. F.; Martin, K. J.; Pitura, R. J.; Rutherford, D., *Main Group Chem.* **1995,** *1*, 99.

VITA

Deepshikha Gupta

EDUCATION

MS, Chemistry, Jamia Millia Islamia University, Delhi, India *May 2008*

BS, Chemistry, University of Delhi, Delhi, India *May 2006*

AWARDS

- **Third Prize Oral Presentation Award** *Nov 2013*
  98th Annual Meeting of the Kentucky Academy of Sciences,
  Morehead State University, KY, US

- **Indian Academy of Sciences (IAS)** Summer Fellowship *June 2007 - Aug 2007*

- **Qualified GATE**, a nationwide Indian science aptitude exam *Spring 2007*

- **ACS** Summer School on Green Chemistry and Sustainability *July 2014*